

1 **Evaluation of the WRF-Chem Performance for gaseous~~the air~~ pollutants over**
2 **the United Arab Emirates.**

3 **Yesobu Yarragunta¹, Diana Francis^{1*}, Ricardo Fonseca¹ and Narendra Nelli¹**

4 ¹ Environmental and Geophysical Sciences (ENGEOS) Lab, Khalifa University of Science
5 and Technology, P. O. Box 127788, Abu Dhabi, United Arab Emirates
6

7 *Correspondence to:* Diana Francis (diana.francis@ku.ac.ae)

8 **Abstract**

9 This study presents a comprehensive evaluation of the Weather Research and Forecasting
10 model coupled with Chemistry (WRF-Chem) in simulating meteorological parameters and
11 concentrations of gaseous~~air~~ pollutants across the United Arab Emirates (UAE) for ~~the months~~
12 ~~of June and December 2018~~2022, representing the contrasting ~~summer and winter~~ climatic
13 conditions ~~of summer and winter.~~ The assessment of WRF-Chem performance
14 ~~involved~~involves comparisons with ground-based observations for meteorological parameters
15 and satellite retrievals from the TROPOspheric Monitoring Instrument (TROPOMI) for
16 gaseous pollutants. ~~The assessment of gaseous pollutants using the WRF-Chem model revealed~~
17 ~~distinct patterns in the estimation of pollutant levels across different areas and seasons.~~the
18 Moderate Resolution Imaging Spectroradiometer (MODIS) for aerosols. The comparison with
19 TROPOMI column ~~concentration revealed the model's strengths~~concentrations demonstrates
20 ~~that WRF-Chem performs well~~ in simulating ~~tropospheric NO₂ and total O₃~~the spatio-temporal
21 patterns, ~~although it had~~ of total column CO and tropospheric column NO₂, O₃, despite certain
22 deficiencies in ~~modelling the total CO~~modeling tropospheric NO₂ column concentrations. ~~The~~
23 ~~model exhibited~~In particular, WRF-Chem shows a strong correlation with TROPOMI
24 retrievals, with correlation coefficients ranging ~~between~~from 0.71 and 0.53 to 0.95 for 82 during
25 summer and 0.86 to 0.94 for 69 during winter ~~among~~for these gaseous pollutants. ~~It~~
26 ~~tended~~The model tends to slightly overestimate NO₂ levels, with a higher discrepancy
27 observed in summer (0.24×10^{15} to 50×10^{15} molecules/cm³cm²) compared to winter ($0.19 \times$
28 10^{15} to 18×10^{15} molecules/cm³cm²). ~~When comparing WRF-Chem to~~ In comparison with
29 TROPOMI-CO data, the discrepancies ~~were~~are more pronounced, ~~showing in winter, with an~~

Formatted

Formatted: Font color: Black

Formatted: Font color: Auto

Formatted: Font color: Auto

Formatted: Font color: Auto

Formatted: Font color: Auto

Formatted: Font color: Auto

Formatted: Font color: Auto

Formatted: Font color: Auto

Formatted: Font color: Auto

Formatted: Font color: Auto

Formatted: Font color: Auto

Formatted: Font color: Auto

Formatted: Font color: Auto

Formatted: Font color: Auto

Formatted: Font color: Auto

Formatted: Font color: Auto

Formatted: Font color: Auto

Formatted: Font color: Auto

Formatted: Font color: Auto

Formatted: Font color: Auto

Formatted: Font color: Auto

Formatted: Font color: Auto

30 overestimation of 0.48×10^{18} molecules/cm² in summer and a significant underestimation of
31 1.13×10^{18} 0.12×10^{18} molecules/cm² in winter. The model cm². Additionally, WRF-Chem
32 consistently underestimates overestimates ozone levels in both seasons, by 0.15×10^{18} and 0.20
33 $\times 10^{18}$ molecules/cm², respectively. Meteorological evaluations revealed the model's tendency.
34 WRF-Chem also exhibits a moderate correlation with both AERONET and MODIS AOD
35 measurements. The correlation at Mezaira is 0.60, while a correlation of 0.65 is observed with
36 MODIS AOD. However, the model tends to underestimate the 2-m temperature in summer and
37 overestimate it in winter AOD, with mean biases ranging from -2.17 a bias of 0.46 at Mezaira
38 and 0.35 compared to +1.19 °C and a Root Mean Square Error in the range of 0.8 to 5.9 °C
39 among the stations. The model showed enhanced performance for the 10-m wind speed and
40 downward shortwave radiation flux, reflecting advancements over previous studies. Therefore,
41 the WRF-Chem model effectively simulates key meteorological parameters and pollutants over
42 the UAE, demonstrating significant regional-scale prediction skills. Areas for further model
43 refinement are also identified and discussed. Integrating model predictions with satellite and
44 ground-based data is emphasized for advancing air quality monitoring and enhancing
45 predictive accuracy of atmospheric pollutants in this region MODIS AOD.

46 Meteorological evaluations reveal that the model generally overestimated T2m in summer
47 ($<0.2^\circ\text{C}$) and underestimated it in winter ($\sim 3^\circ\text{C}$) with correlation coefficients between 0.7 and
48 0.85. Temperature biases are linked to surface property representation and model physics. For
49 WS10m, biases were within ± 0.5 m/s, indicating good agreement, although overestimations
50 suggest deficiencies in surface drag parameterization. The dry bias observed was consistent
51 with other studies due to dry soil, inaccurate mesoscale circulation representation, and bias in
52 forcing data. The model also overestimated incoming shortwave radiation by ~ 30 W/m² in
53 December due to reduced cloud cover. Night-time cold and dry biases were observed due to
54 more substantial wind speeds and cooler air advection. Comparisons with ERA5 reanalysis
55 showed regional T2m variations with high correlation coefficients (0.97 in summer, 0.92 in
56 winter). Both WRF-Chem and ERA5 displayed consistent seasonal patterns in the planetary
57 boundary layer, correlating with temperature changes and indicating good overall model
58 performance.

59 **Keywords:** Air quality modelling, gaseous modeling, air pollutants, TROPOMI satellite
60 retrievals, MODIS, WRF-Chem, UAE.

61 **Key points:**

Formatted: Font color: Auto

Formatted: Font color: Auto

Formatted: Font color: Auto

Formatted: Font color: Auto

Formatted: Font color: Auto

Formatted: Font color: Auto

Formatted: Font color: Auto

Formatted: Font color: Auto

Formatted: Font: 12 pt

- 62 ● First high-resolution WRF-Chem air quality ~~modelling~~ modeling study over the United
63 Arab Emirates (UAE)
- 64 ● WRF-Chem's ability to simulate meteorological parameters and pollutant levels over
65 the UAE is assessed during summer and winter in ~~2018~~2022.
- 66 ● The model ~~showed a strong correlation~~ strongly correlated with TROPOMI satellite
67 data, achieving correlation coefficients of 0.74-0.53-0.9582 in summer and 0.8640-0.9469
68 in winter for ~~different~~ gaseous pollutants.
- 69 ● Lower model skill in simulating ~~total CO-tropospheric NO₂~~ columns, in contrast to the
70 more accurate ~~modelling~~ modeling of ~~tropospheric NO₂-total CO~~ and ~~total~~ tropospheric
71 O₃ columns ~~as compared to TROPOMI data, particularly in summer.~~
- 72 ● WRF-Chem demonstrated a moderate correlation with AERONET and MODIS for
73 AOD during the summer, with correlation coefficients of 0.60 and 0.65, respectively.
- 74 ● Meteorological analysis revealed a tendency to ~~underestimate-overestimate~~ surface
75 temperature by 0.52 °C in summer and ~~overestimate-underestimate~~ it by 1.3 °C in
76 winter-
- 77 ● across land regions. Surface wind speed is overestimated by 0.1-0.95 m/s in both
78 seasons across various regimes.
- 79

Formatted: Outline numbered + Level: 1 + Numbering
Style: Bullet + Aligned at: 0.63 cm + Indent at: 1.27 cm

Formatted: Font color: Auto

Formatted: Outline numbered + Level: 1 + Numbering
Style: Bullet + Aligned at: 0.63 cm + Indent at: 1.27 cm

Formatted: Font: Calibri, 11 pt

80 1. Introduction

81 The United Arab Emirates (UAE), a federation of seven emirates, has undergone rapid
82 urbanization and industrialization over the last five decades, which has had a profound impact
83 on its air quality (Ramadan, 2015). The major factors affecting air quality in the UAE include
84 emissions from industrial activities, vehicular traffic, construction projects- ([Teixido et al.,
85 2021](#)), and occasionally, natural phenomena such as dust storms, which are quite prevalent in
86 the region due to its desert climate (Environment Agency – Abu Dhabi, 2018; Francis et al.,
87 2020; 2022b; Karagulian et al., 2019). The rapid economic growth of the UAE, especially in
88 cities like Dubai and Abu Dhabi, has led to a surge in energy demand and ~~desalinated~~-water,
89 [the latter obtained from desalination and cloud seeding activities \(Wehbe et al., 2023\)](#), largely
90 met through the burning of fossil fuels (Shahbaz et al., 2014). This has resulted in increased
91 emissions of pollutants like oxides of nitrogen (NO_x), sulfur dioxide (SO₂), particulate matter
92 (PM), and volatile organic compounds (VOCs). Moreover, the heavy traffic in urban areas
93 contributes to the elevated levels of ground-level ozone and particulate pollution (Abuelgasim
94 & Farahat, 2020; Li et al., 2010). Understanding the dynamics of air quality in the UAE
95 involves considering both the environmental challenges posed by rapid development and the
96 steps being taken to mitigate these impacts. The pursuit of balancing economic growth with
97 environmental sustainability is central to this discourse. This area of study is not only vital for
98 ensuring the health and well-being of the population but also plays a crucial role in the UAE's
99 vision for a sustainable future.

100
101 The swift urban expansion in the UAE, [which is expected to continue in the coming decades](#),
102 could intensify air pollution sources. With surface observations sparse in this region, satellite
103 remote sensing becomes a crucial method for air quality monitoring (Chudnovsky et al., 2014;
104 Fonseca et al., 2023; Francis et al., 2023). What is more, satellite measurements themselves
105 fall short in clarifying the different atmospheric processes responsible for peak pollution levels.
106 Consequently, integrating chemistry transport models with satellite-derived and ground-based
107 observations can significantly improve our understanding of pollutant emissions, distribution,
108 transport, and transformation in the targeted regions (Eltahan et al., 2018; Li et al., 2018;
109 Yarragunta et al., 2020; Yin et al., 2021). Air quality (AQ) modelling is dedicated to
110 unravelling the complicated aspects of atmospheric chemistry and transport across both global
111 and regional levels, as explored in numerous studies conducted around the world (Emmons et
112 al., 2010; Kumar et al., 2011, 2018; Tie et al., 2001; Yarragunta et al., 2019, 2020, 2021).

113 Despite facing limitations due to the often low spatial and temporal resolution of observational
114 data, AQ models effectively generate detailed air quality information for remote regions- (e.g.,
115 [Guo et al., 2024a](#)). They predict the formation and removal of air pollutants and facilitate a
116 thorough examination of the transport and photo-chemical transformation of trace gases
117 following their emission into the atmosphere (Archer-Nicholls et al., 2015; Georgiou et al.,
118 2018; Nhu et al., 2021; Sicard et al., 2021). They are also employed globally for operational
119 air quality forecasting (Jena et al., 2021; Koo et al., 2012; Kumar et al., 2012, 2021; Srinivas
120 et al., 2016; Zhang et al., 2012). Air quality models are categorized into two types: 'fully
121 coupled' models, which integrate interactions between chemistry and meteorology, and 'offline'
122 models, where chemistry and meteorology simulations are conducted independently (Gao &
123 Zhou, 2024). Some of state of the art AQ models include the Weather Research and
124 Forecasting (WRF) model coupled with chemistry (WRF-Chem; Grell et al., 2005; Skamarock
125 et al., 2008), WRF-Chem-MADRID (Model of Aerosol Dynamics, Reaction, Ionization and
126 Dissolution; Zhang et al., 2010), CESM2 (Community Earth System Model version 2;
127 Emmons et al., 2020), CHIMERE (Menut et al., 2021), LOTOS-EUROS(v2.0) (Long Term
128 Ozone Simulation European Operational Smog; Manders et al., 2017) and COSMO/MESSy
129 (Consortium for Small Scale Modelling/ Modular Earth Submodel System; Kerkweg &
130 Jöckel, 2012). However, before using these AQ models for ~~future~~[operational or research](#)
131 applications, it is crucial to conduct thorough evaluations to assess the quality of their
132 ~~simulations~~[predictions](#). The AQ model chosen for the current study is ~~the~~ WRF-Chem with its
133 foundational meteorological component, WRF. [WRF-Chem has been used for research studies](#)
134 [in the Arabian Peninsula \(Parajuli et al. 2019, 2023, 2024\), with the meteorological component](#)
135 [optimized for simulations over the region \(Chaouch et al., 2017; Nelli et al., 2020; Abida et al.,](#)
136 [2022; Fonseca et al. 2020, 2021, 2022a\)](#).

137
138 The majority of studies conducted in the UAE and similar arid regions have primarily
139 focused on evaluation of meteorological parameter including temperature, humidity, wind, and
140 solar radiation (Parajuli et al., 2019; Nelli et al., 2020; Fonseca et al., 2020, 2021) with a few
141 others investigating the particulate matter ([PM](#)) dynamics, especially mineral dust. For
142 instance, Ukhov et al., (2021) noted inaccuracies in the WRF-Chem model related to the
143 [commonly used bulk Goddard Chemistry Aerosol Radiation and Transport \(GOCART; Chin](#)
144 [et al., 2022\)](#) aerosol module, affecting PM_{2.5} and PM₁₀ diagnostics. Karagulian et al., (2019)
145 highlighted the effectiveness of integrating WRF-~~chem~~[Chem](#) model simulations with satellite
146 and ground observations to understand and predict the impact of severe dust storms on air

147 quality. Karumuri et al., (2022) reported significant air quality changes due to COVID-19
148 lockdown measures, with reduced trace gas concentrations but increased particulate matter
149 from dust activities, the latter stressed by Francis et al. (2022a) who attributed it to changes in
150 the atmospheric circulation. Moreover, Parajuli et al., (2022, 2023) utilized high-resolution
151 WRF-Chem simulations and advanced aerosol schemes to analyse the dust and rainfall
152 dynamics, providing insights into the direct and indirect effects of dust on rainfall, which aids
153 in better regional water resource planning through accurate rainfall predictions. However, in
154 particular, while through the indirect effects dust promotes precipitation provided there is
155 sufficient moisture for both normal and extreme rainfall events, the dust direct effects on
156 precipitation shift from negative for normal rainfall events (weaker sea-breeze arising from
157 surface cooling) to positive in extreme events (smaller effects on the sea breeze). Zhang et al.
158 (2024) stressed the two-way interaction between dust aerosols and the Planetary Boundary
159 Layer (PBL) dynamics: aerosols directly impact the PBL structure through direct and indirect
160 effects, while the the modified PBL characteristics and low-level circulation modulate aerosol
161 processes. All the aforementioned studies focus on dust aerosols, there is no assessment to date
162 of the model performance for the simulation of gaseous pollutants ~~model performance~~ over the
163 region ~~despite~~. This is crucial, given the complex dynamics between anthropogenic and natural
164 factors in air quality management and the necessity of tailored model configurations for
165 accurate environmental assessments in arid regions.

166
167 This study represents the first comprehensive evaluation of the WRF-Chem model in the
168 Arabian Peninsula, with a focus on the UAE, a country that is representative of those in the
169 region, specifically examining concentrations of gaseous air pollutants along with crucial
170 meteorological parameters relevant to air quality studies. The primary objective of this study
171 is twofold:

- 172
- 173 • Evaluate the WRF-Chem's ability to replicate meteorological conditions. This involves
174 comparing the model's simulation of temperature, wind speed, relative humidity,
175 downward short-wave radiation and boundary layer height against ground-based
176 observations and data from the European Centre for Medium-Range Weather
177 Forecasting (ECMWF) fifth reanalysis product, ERA5 (Hersbach et al., 2020)
178 reanalysis-);
 - 179 • Assess the model's performance in simulating concentrations of key gaseous pollutants,
180 specifically NO₂, O₃, NO₂, O₃, and CO. The skill of, which are prevalent in the WRF-

Formatted: Outline numbered + Level: 1 + Numbering
Style: Bullet + Aligned at: 0.63 cm + Indent at: 1.27 cm

Formatted: Font color: Auto

Formatted: Font color: Black

Formatted: Font color: Black

181 ~~Chem in simulating these pollutants is evaluated by comparing its simulations~~region
182 ~~(Teixido et al., 2021), against data from the TROPOspheric Monitoring Instrument~~
183 ~~(TROPOMI; ~~Veefkind~~Veefkind et al., 2012) ~~onboard~~ the Sentinel-5 Precursor (S5P)~~
184 ~~satellite. Additionally, aerosol optical depth (AOD) at 550 nm from AERONET and~~
185 ~~MODIS satellite observations are used to evaluate the model's skill in simulating~~
186 ~~aerosol concentrations.~~

Formatted: Font color: Black

187
188 The structure of the paper is as follows: Section 2 describes the configuration of the WRF-
189 Chem considered in this work. Section 3 elaborates on the methodology and datasets used in
190 this study. Section 4 provides a comprehensive assessment of the ~~WRF-Chem's~~model's
191 simulated data ~~with~~against observational datasets, reanalysis and satellite-derived products.
192 Section 5 concludes by outlining the main findings.

193 2. WRF-Chem configuration

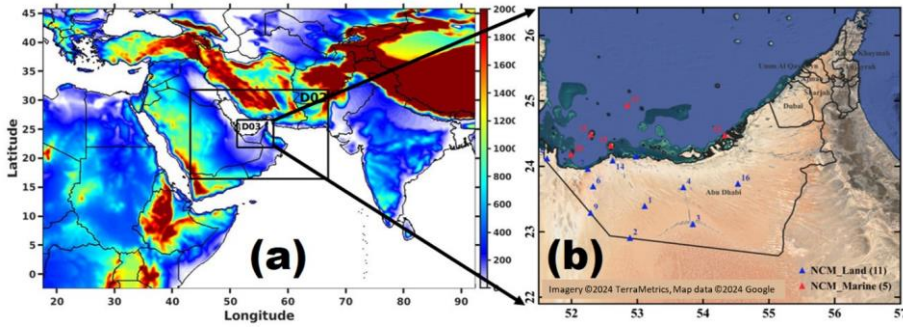
194 ~~The central objective of this study is to apply a regional chemistry/dynamical model~~WRF-
195 Chem version 4.3.1 is employed to simulate the atmospheric conditions and transport of
196 pollutants in the UAE, ~~whose forecasts will be evaluated against in situ, space based~~
197 ~~measurements and a state-of-the-art reanalysis dataset. To this end, the WRF-Chem version~~
198 4.3.1 is employed. WRF-Chem is a mesoscale regional chemistry transport model, developed
199 by the National Oceanic and Atmospheric Administration (NOAA) Earth System Research
200 Laboratory (ESRL), ~~and has been contributed to by~~with contributions from the global science
201 community. In WRF-Chem, ~~the~~ air quality ~~components~~ and meteorological components are
202 predicted simultaneously using the same grid-~~coordinates~~, transport, timestep, and sub-grid
203 scale physics. A detailed description of the model is found in Grell et al., (2005) ~~and~~,
204 Skamarock et al., (2008) ~~and~~ Powers et al., (2017). The physics schemes employed in the
205 simulations are the Rapid Radiative Transfer Model for Global Circulations Models (RRTMG)
206 for radiation parametrization of both short and long wave radiation (Iacono et al., 2008), the
207 cloud microphysics is represented by the Morrison 2-moment (Morrison et al., 2009), and the
208 Kain-Fritsch scheme is used for convective parameterisation (Kain, J.S, 2004) ~~with the~~
209 subgrid-scale cloud feedback to radiation switched on (Alapaty et al., 2012). The Unified Noah
210 model is used to represent the land surface model (Tewari et al., 2004) ~~with~~ an improved
211 representation of soil texture and land use/land cover (LULC) over the UAE (Temimi et al.,
212 2020). The boundary layer dynamics are represented by the Yonsei University (YSU) scheme

Formatted: Font color: Auto

213 (Hong, 2010). ~~Other~~The chosen physics schemes are listed in Table 1. ~~Simulated~~The simulated
214 mesoscale meteorology is kept in line with ~~the~~ analysed meteorology through spectral nudging
215 to the National Centre for Environmental Prediction (NCEP) Global Forecast System (GFS)
216 analyses used to drive the model, in an attempt to limit errors in the mesoscale transport. During
217 the simulations, horizontal and vertical wind, potential temperature and water vapour mixing
218 ratio are nudged to GFS analyses in all model layers above the planetary boundary layer on a
219 time-scale of 6 hours ~~for scales above ~1000 km~~. Meteorological conditions were initialised
220 by NCEP GFS 6-hourly analyses at 0.25° resolution.

221 This study utilised the Model for Ozone and Related Chemical Tracers, version 4
222 (MOZART-4) chemical mechanism for calculating gas-phase chemistry, which includes 81
223 chemical species with 159 gas-phase reactions and 38 photolysis processes (Emmons et al.,
224 2010). Aerosol chemistry is represented by the ~~Goddard Chemistry Aerosol Radiation and~~
225 ~~Transport (GOCART-)~~ (Chin et al., 2002) ~~module~~, along with the Tropospheric, Ultraviolet
226 and Visible (TUV) full photolysis scheme (Madronich, 1987; Tie, 2003), which deploys
227 climatological O₃ and O₂ columns. Dry deposition ~~wasis~~ calculated using Wesely (1989).
228 Anthropogenic emissions ~~were~~are taken from the Emission Database for Global Atmospheric
229 Research (EDGAR) version ~~5 (EDGARv5)~~8.1 at a 0.1 × 0.1° horizontal resolution ~~for 2022~~
230 ~~(Crippa et al., 2020)~~, ~~consistent with the simulation period~~. Emissions include SO₂, NO_x, CO,
231 ~~Non-Methane Volatile Organic Compounds (NMVOC)~~, NH₃, black carbon (BC) and organic
232 carbon (OC). Biogenic emissions ~~were~~are calculated online by the Model of Emissions of
233 Gases and Aerosol from Nature (MEGAN; Guenther et al., 2012). ~~Model simulation uses~~
234 ~~CAM chem model results as chemical~~The chemistry boundary conditions (BCs) ~~for the~~
235 ~~outer~~used in domain D01 and ~~the~~ initial conditions (ICs) for all domains ~~in the WRF-Chem~~
236 ~~simulations are extracted from CAM-chem model forecasts~~ (Emmons et al., 2020). In this
237 ~~present~~ work, we run the WRF-Chem model ~~using the aforementioned physical and chemical~~
238 ~~processes~~ on the three nested domains with horizontal resolutions ~~of 27-, 9-, and 3-km~~
239 corresponding to 283×205, 271×193, and 256×178 grid points ~~and 45-, respectively. In the~~
240 vertical, ~~there are 45 layers, with the lowest model level at about 27 m above the surface~~. The
241 outermost domain covers ~~the vast majority~~most of the Middle East and ~~the~~ surrounding region,
242 while the innermost domain covers the entire UAE (Fig. 1(a)). The analysis in this research
243 article exclusively utilizes results from the inner domain (D03). ~~The~~Fig. 1(b) shows the spatial
244 distribution of ~~ground-based observations from NCM are depicted in Fig. 1(b). UAE airport~~
245 ~~stations, the WISE-UAE observational site, and AERONET locations for AOD measurements.~~

Formatted: Font color: Auto



246

247 **Figure 1: Model Configuration:** (a) The WRF domain configuration consists of three telescoping
 248 nests, with the outermost boundaries denoting the parent grid (D01). D02 and D03 are the nested
 249 domains. Right panel (b) is a zoom of the innermost domain (D03) showing the spatial distribution of
 250 the 16 meteorological stations (land stations are denoted by blue triangles, and marine stations are
 251 represented by red triangles). The shading in (a) represents the orography (m). Further details about the
 252 stations are given in Tables 2.

253

254

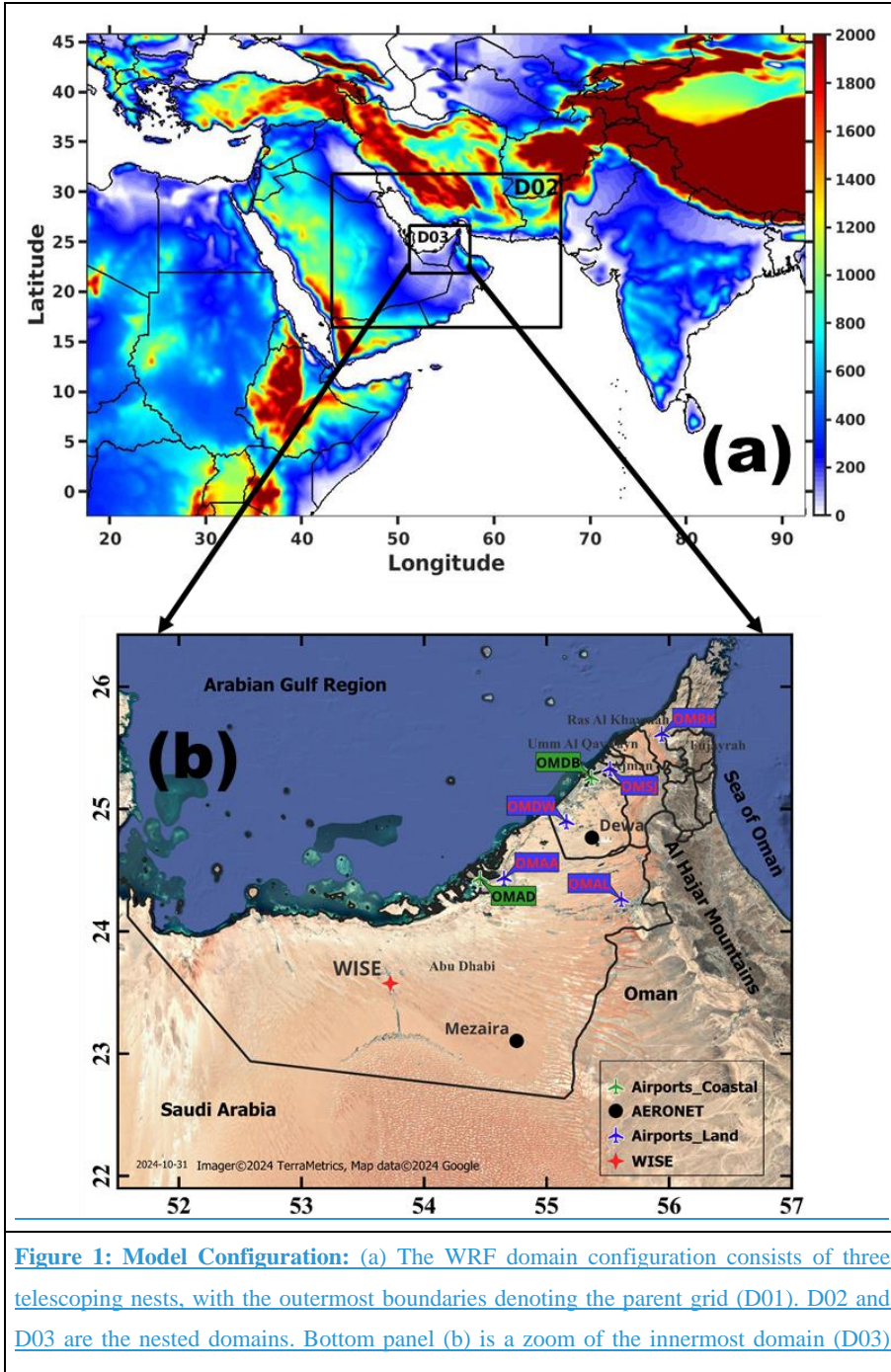


Figure 1: Model Configuration: (a) The WRF domain configuration consists of three telescoping nests, with the outermost boundaries denoting the parent grid (D01). D02 and D03 are the nested domains. Bottom panel (b) is a zoom of the innermost domain (D03)

showing the spatial distribution of the seven automatic weather stations operated in airports (land stations (5) are denoted by blue color, coastal stations (2) are represented by green color) along with Wind-blown Sand Experiment (WISE)-United Arab Emirates (UAE) Site by red color star and black dots represent two AERONET stations (Mezaira and Dewa). The shading in (a) represents the orography (m). Further details about the stations are given in Tables S1.

255

256 The WRF-Chem simulation is driven by anthropogenic emissions from the EDGAR
257 database, version 8.1, at a horizontal resolution of $0.1^\circ \times 0.1^\circ$ for the year 2022 (Crippa et al.,
258 2020). The EDGAR emission inventory accounts for day-to-day variability (e.g., weekday
259 versus weekend) and hourly fluctuations (diurnal cycle) of anthropogenic emissions, as
260 detailed by Crippa et al. (2020). For example, road transport emissions are generally lower at
261 night and higher during daytime hours, while agricultural emissions tend to peak during
262 specific months. To achieve an hourly resolution for the model, we scaled the coarsely resolved
263 emission data using predefined hourly, daily, and monthly scaling factors (temporal profiles).
264 The initial temporal profiles are derived from the work of Olivier et al. (2003) and have been
265 refined to place greater emphasis on the most relevant emission sectors for each pollutant
266 within the study region. According to the Environment Agency – Abu Dhabi (2018), the
267 primary sectors contributing to emissions include traffic, the power industry, energy used in
268 buildings, and the manufacturing industry. Using these optimised emission profiles, emissions
269 for NO_2 and CO were dynamically adjusted during the model simulations to better capture local
270 emission patterns and their variability. However, the results indicated that emissions for NO_2
271 and CO are underestimated by EDGAR. Although WRF-Chem simulations incorporate
272 temporal profiles of emissions, the impact of these emission estimates on daily variations could
273 not be fully assessed in this study due to the lack of ground-based measurements and the limited
274 temporal resolution of satellite data. MODIS and TROPOMI satellites each pass over the study
275 area only once per day, restricting the ability to capture daily variations comprehensively.
276 Consequently, this article is limited in its assessment of daily emission variability. Moreover,
277 WRF-Chem supports the vertical distribution of trace gas emissions, which is particularly
278 useful for capturing emissions released at elevated altitudes, such as those from combustion
279 stacks. Accurately representing the vertical distribution of emissions is important for
280 simulating atmospheric processes. However, incorporating this complexity would likely
281 provide minimal improvements in model accuracy for regions where surface emissions

dominate, and where observational constraints are largely limited to coarse vertical resolution or surface-level data. Therefore, in this study, all emissions were injected into the lowest model layer to align with the observational data characteristics and the typical conditions in the study area.

Table 1: WRF-chem model setup

Model set-up	Option
Model version	4.3.13
Domain	3 domains
Horizontal resolution	D01:27km, D02:9km and D03:3km
Simulation period	Monthly runs from June 2018 and December 2018-2022
Model spin-up period	2 days in each month
Vertical resolution	45 eta levels up to 50 hPa.
Domain size	D01: 283×205 grids, D02: 271×193 grids and D03: 256×178 grids
Meteorological boundary	NCEP FNL reanalysis (0.25°, 6-hourly)
Chemical boundary	CAM-Chem (Emmons, Fasullo, et al., 2020)
Physical Process	Parameterization Scheme
Microphysics	Morrison double moment (Morrison et al., 2009)
Cumulus parameterization	Kain-Fritsch (Kain, J.S., 2004) with the subgrid-scale cloud-radiation feedbacks activated (Alapaty et al., 2012)
Shortwave radiation	Rapid Radiative Transfer Model for GCMs (RRTMG) (Iacono et al., 2008)
Longwave radiation	Rapid Radiative Transfer Model for GCMs (RRTMG) (Iacono et al., 2008)
Land surface	Unified Noah land surface model (Tewari et al., 2004)
Planetary boundary layer	Yonsei University scheme (Hong, 2010)
Chemistry option	Scheme used
Gas phase chemistry	MOZART-4 (Emmons et al., 2010)
Aerosol chemistry	GOCART (Chin et al., 2002)

Formatted Table

Formatted: English (U.A.E.)

Photolysis	Madronich F-TUV (Madronich, 1987; Tie, 2003)
Biogenic emissions	MEGAN (Guenther et al. 2012)
Dry deposition	Wesely (Wesely 1989)

288

289 3. Data Sets and methodology

290 3.1 Meteorology observations

291 In this study, meteorological data from 468 automatic weather stations (AWS) operated by
 292 the National Center of Meteorology (NCM), at UAE were airports are utilized to assess the
 293 WRF-Chem simulations for air temperature at 2 meters above ground (T2m), wind speed at 10
 294 meters (WS10m), and downward shortwave radiation flux at the surface (SR) relative humidity
 295 at 2 meters above ground (RH2m) forecasts during June and December of 2018-2022. The
 296 spatial distribution of the stations across the UAE is illustrated in Fig. 1(b) (refer to Table 2S1
 297 for more details). These locations were are categorically divided into two regions—land stations
 298 (station with ID number: 1-9, 14 code: L OMAA, OMDW, OMAL, OMSJ, OMRK) and 46) and
 299 marine coastal stations (station with ID number: 10-13 and 15 code: OMAD, OMDB)—
 300 following the criteria outlined in Branch et al., (2021). Subsequent analyses are based on these
 301 two primary categories, with the land region comprising 11 stations (marked with green
 302 triangles) and the marine region comprising 5 stations (marked with yellow triangles) in Fig.
 303 1(b). Additional information on the specifics, quality control measures, and other research
 304 studies based on NCM data can be found in the referenced literature (Branch et al., 2021;
 305 Fonseca et al., 2020, 2021, 2022; Temimi et al., 2020a). 5 stations and the coastal region
 306 comprising 2 stations (Fig. 1b). In addition to the UAE airports data, we utilized meteorological
 307 data from the WInd-Blown Sand Experiment (WISE)-UAE measurements. The WISE-UAE
 308 experiment started on 25 July 2022 at Madinat Zayed (23.5761°N, 53.7242°E; elevation: 119
 309 m; Fig. 1b), located 120 km southwest of Abu Dhabi, UAE. An overview of the instrumentation
 310 and experiment site used during WISE-UAE is provided in Nelli et al. (2024(a, b)). This study
 311 uses WS10m T2m, RH2m, and downward shortwave radiation flux (SW) from these
 312 measurements to validate the WRF-Chem simulations for December 2022. The specifications
 313 and accuracies of the instruments used in WISE-UAE are outlined in detail, along with the
 314 stringent quality control procedures applied, as described in Nelli et al. (2024(a,b,c)).

315

Formatted: Font: 14 pt
 Formatted: Heading 2

316 **Table 2 List of Automatic Weather Stations (AWS) utilized for evaluating the WRF-Chem model.**

ID	Name	Lat.	Lon.	Altitude (m)	Region
1	Owtaid	23.40	53.11	160	Land
2	Mukhariz	22.91	52.89	130	Land
3	Mezaria	23.12	53.84	110	Land
4	Madinat Zayed	23.68	53.70	110	Land
5	Al Gheweifat	24.12	51.63	47	Land
6	Bu Hamrah	23.51	54.53	136	Land
7	Barakah	23.96	52.25	5	Land
8	Al Qlaa	24.16	52.98	150	Land
9	Al Jazeera	23.29	52.29	70	Land
10	Yasat	24.19	52.00	115	Marine
11	Sri Bani Yas	24.32	52.60	101	Marine
12	Qarnen	24.94	52.85	26	Marine
13	Dalma	24.49	52.29	10	Marine
14	Al Ruwais	24.09	52.62	33	Land
15	Abu Dhabi	24.48	54.33	3	Marine
16	Al Tawiyen	25.56	56.07	186	Land

317

318 **3.2 AERONET**

319 [The Aerosol Robotic Network \(AERONET\) program is a global federation of ground-based](#)
 320 [sun photometers comprising more than 400 stations worldwide \(Holben et al., 1998\).](#)
 321 [AERONET utilizes multiple bands ranging from UV to near-IR wavelengths to measure](#)
 322 [spectral sun irradiance and sky radiances, from which Aerosol Optical Depth \(AOD\) at 550 nm](#)
 323 [and other aerosol properties are derived. A detailed description of the AERONET retrievals is](#)
 324 [provided in Holben et al. \(1998\). This study uses Level 2.0 AOD data at 550 nm from Mezaira](#)
 325 [for June and from Dewa for December 2022, with an hourly resolution. It is important to note](#)
 326 [that AOD retrieved from AERONET is accurate to within 0.01 \(Dubovik et al., 2000\).](#)

327 **3.3.2 ERA-5 Reanalysis data**

328 The fifth-generation [European Centre for Medium Range Weather Forecasts \(ECMWF\)](#)
 329 reanalysis, known as ERA-5 (Hersbach et al., 2020), represents a significant advancement over
 330 its predecessor, [the ERA-Interim reanalysis](#), introduced by Dee et al., (2011). ERA-5
 331 incorporates a sophisticated four-dimensional variational (4D-Var) data assimilation method,
 332 utilizing the 41r2 cycle of the Integrated Forecast System (IFS). This system is enhanced by
 333 [the integration of both integrating a soil model and an ocean wave model models](#), offering a

334 comprehensive approach to climate data analysis. ~~For the purposes of this research, we~~We
335 accessed ERA-5 data through the Copernicus Climate Change Service Climate Data Store
336 (CDS) ~~for this research.~~ The dataset provides atmospheric observations across 137 hybrid
337 vertical levels, with ~~raw model data available on the CDS~~ interpolated onto 37 distinct pressure
338 levels. These levels span from 1000 hPa, close to the Earth's surface, up to 1 hPa, reaching
339 altitudes of approximately 80 km. Further details on the ERA-5 dataset are available in Dee et
340 al. (2011) and Hersbach et al. (2020). Our study ~~specifically utilized~~utilizes explicitly hourly
341 data for a selection of meteorological parameters: ~~air temperature at 2 meters above the ground~~
342 (~~T2m~~), ~~wind speed at 10 meters (WS10m)~~, ~~downward shortwave radiation flux at the surface~~
343 (~~SR~~), ~~SW~~, and planetary boundary layer height (PBL), for ~~the months of~~ June and December
344 ~~2018~~2022.

345 **3.34 Satellite-borne observations: TROPOMI**

346 Launched by the European Space Agency (ESA) on October 13, 2017, the ~~TROPOspheric~~
347 ~~Monitoring Instrument (TROPOMI) instrument~~ is aboard the ~~Sentinel-5 Precursor (S5P)~~
348 satellite, operating in a near-polar sun-synchronous orbit. Positioned at an altitude of 817 km,
349 the S5P satellite crosses the equator at a local solar time of 13:30, boasting a wide swath of
350 approximately 2600 km, and providing daily global coverage. TROPOMI features four distinct
351 spectrometers that measure the ~~radiation in the~~ ultraviolet (UV) and UV-visible (UV-VIS)
352 range (270 to 500 nm), near-infrared (NIR) range (675 to 775 nm), and short-wave infrared
353 (SWIR) range (2305 to 2385 nm) spectral bands (Veefkind et al., 2012). Notably, the last two
354 spectral bands, NIR and SWIR, are newly introduced in TROPOMI compared to its
355 predecessor OMI (Ozone Monitoring Instrument). TROPOMI's data products encompass daily
356 observations of trace gases, including CO, O₃, NO₂, CH₄, HCHO, aerosols, and cloud
357 properties. ~~The present~~This study utilized daily ~~tropospheric~~ NO₂, ~~total~~ CO ~~columns~~, and ozone
358 ~~column density profile~~ level 2 products ~~from TROPOMI~~, downloaded from the GES DISC
359 website (<https://disc.gsfc.nasa.gov/>) for the period of June ~~1-30~~ and December ~~1-31, 2018~~2022.
360 The specific data sets employed for the present study ~~includes~~include
361 S5P_OFFL_L2_O₃ ~~PR~~ for O₃, S5P_OFFL_L2_CO for CO, and S5P_OFFL_L2_NO₂ for
362 NO₂, covering the study region bounded by longitudes [51°,58°] and latitudes [21°,−27°].
363 Further details ~~regarding on~~ each product, ~~including the retrieval~~ ~~algorithm~~algorithms and
364 validation results, are summarized in the ~~subsequent~~following section.

365

Formatted: Not Superscript/ Subscript

366 TROPOMI retrieval of NO₂ columns are derived using UV-VIS spectrometer backscattered
367 solar radiation measurements in the wavelength range of 405-465 nm and provides total and
368 tropospheric NO₂ vertical column density with a near-nadir resolution of ~~7.37~~ × 3.5 km. The
369 total NO₂ slant column density (SCD) is retrieved from the measured solar irradiance spectra
370 using the Differential Optical Absorption Spectroscopy (DOAS) method. Tropospheric and
371 stratospheric slant column densities are separated from SCD by a data assimilation system
372 based on the chemistry transport model V5 (TM5-MP). Afterwards, they are converted to
373 vertical column densities (VCDs) with the help of look-up table of altitude-dependent air-mass
374 factors (AMFs) and information on the vertical distribution of NO₂ from TM5-MP a priori
375 profile with a horizontal resolution of 1° x 1° and a time step of 30 min (Boersma et al., 2018;
376 Van Geffen et al., 2022). The TROPOMI NO₂ product has been extensively evaluated using
377 ground-based and aircraft observations and is found to have a high correlation and low bias of
378 less than 30% with respect to in-situ measurements (Griffin et al., 2019; Ialongo et al., 2020).
379 We used the both reprocessed (RPRO) and offline (OFFL) TROPOMI NO₂ data files ~~with~~from
380 the most recent processor ~~version of 1.2.2, versions depending on availability~~ for ~~the study~~
381 ~~period a given day of observations~~. Additionally, ~~two more~~there is another NO₂ ~~products~~
382 ~~are~~product available ~~such as offline (OFFL) and~~ near-real time (NRTI). NRTI data files are
383 generated using TM5-MP forecast data rather than analysis data as with REPO and OFFL files
384 (Van Geffen et al., 2022). The differences between the OFFL/REPO and NRTI NO₂ products
385 are generally very small (Ialongo et al. (2020) and references therein ~~Ialongo et al., 2020~~).

386
387 The Shortwave Infrared Carbon Monoxide Retrieval (SICOR) algorithm is used to retrieve
388 CO total column densities from TROPOMI in the spectral range of 2305 to 2385 nm (Landgraf
389 et al., 2016). The SICOR algorithm accounts for a profile-scaling approach that scales retrieved
390 CO total column to the a priori reference profile. The a priori reference profiles are taken from
391 the global chemistry transport model simulations of TM5-MP, and ~~they~~ vary based on the
392 location, month and year (Krol et al., 2005). ~~The~~ detailed outline of all settings and other
393 auxiliary data sets used for CO retrievals ~~are outlined~~is given in ~~the~~ Landgraf et al., (2016).
394 This study limits the analysis to CO pixels corresponding to clear-sky conditions and mid-level
395 clouds by filtering the data using the quality flag variable (qa_value). The scenes corresponding
396 to qa_value > 0.5 are used in this current analysis as suggested in the ATBD (algorithm
397 theoretical baseline document; Landgraf et al., 2016). In this present work, TROPOMI CO
398 measurements for ~~the period from 1-30~~ June and ~~1-31~~ December, ~~2018, 2022~~ have been
399 analysed. Moreover, we use either the reprocessed (RPRO) or offline (OFFL) data files from

400 most recent processor versions depending on availability for a given day of observations.
401 Wizenberg et al., (2021) compared global TROPOMI retrieved CO total columns with
402 corresponding ACE-FTS (Atmospheric Chemistry Experiment- Fourier transform
403 spectrometer) columns for the period from November 2017 to May 2020 and found a small
404 relative bias of -0.83% with a correlation coefficient of 0.93 between two data sets. Similar
405 results ~~were~~are also found between TROPOMI CO with corresponding CO fields from the
406 ECMWF assimilation system: Borsdorff et al. (2018) reported a small mean difference between
407 the two data sets of 3.2% with a correlation coefficient of 0.97.

408
409 TROPOMI also provides ~~total ozone column (TOC) and ozone profile data~~profiles
410 [\(5P OFFL L2 O3 PR\)](#) at ~~1533~~ pressure levels [with a horizontal resolution of 28x28 km](#). It
411 measures radiances and irradiances in the ultraviolet wavelength of 270-330 nm and provides
412 the ozone profile information. The Optimal Estimation (OE) algorithm is used to retrieve the
413 ozone profile data. Before this stage, various pre-processing steps are applied to the measured
414 spectra before the estimation of the ozone profile. The main process of the algorithm is the OE
415 method, which combines the information from the measured spectra with the a-priori
416 information. ~~The a-priori information~~latter is based on climatology as described in ~~the~~Labow
417 et al., (2015). The description of the various pre-processing steps performed to retrieve ozone
418 profiles is presented in the Algorithm Theoretical Basis Document (Veeffkind, et al., 2021). The
419 validation of TROPOMI retrieved ozone profile data against the ground-based measurements
420 reported a median bias of 0.3% for OFFL/REPO products while ~~0.8% for NRTI ozone products~~
421 [\(Lambert et al., 2023\)](#).% for NRTI ozone products [\(Lambert et al., 2023\)](#). Our focus is
422 [specifically on the tropospheric ozone column due to its direct relevance to surface air quality](#).
423 [Total column ozone measurements are primarily influenced by stratospheric ozone, which](#)
424 [accounts for approximately 90% of the total column, while tropospheric ozone comprises only](#)
425 [around 10%. Given this, we have used ozone profile data from the surface to 100 hPa.,](#)
426 [designated as tropospheric ozone columns for this study and referred to as TROPOMI-O₃,](#)
427 [expressed in Dobson Units \(DU\), where 1 DU = 2.69x10¹⁶ molecules/cm².](#)

428 **3.4.3.5 Satellite-borne observations: MODIS**

429 [The Moderate Resolution Imaging Spectroradiometer \(MODIS\) sensor was launched into the](#)
430 [polar sun-synchronous orbit at an altitude of 705 km aboard NASA's two Earth Observing](#)
431 [System \(EOS\) satellites, Terra \(Feb-2000\) and Aqua \(June-2002\) \[Kaufman et al., 1997;](#)

432 [Remer et al., 2005](#). The equator crossing times of two satellites were, Terra crossing at 1030
433 LST and Aqua crossing at 1330 LST. The MODIS sensor has a swath of ~2330 km and
434 provides near-global coverage with a temporal resolution of 1-2 days. The sensor measures the
435 reflected solar radiation from the Earth's atmosphere and the surface as well as emitted thermal
436 radiation at 36 spectral bands from 0.41 to 14 μm with three spatial resolutions: 250m, 500m,
437 and 1km. Seven of these bands operating in the spectral range of 0.415-2.155 μm can
438 effectively retrieve the AOD over land and ocean [Levy et al. 2013 ; Hsu et al. 2015 ; Sayer et
439 al., 2014a; 2014b; 2015] . The MODIS retrieval algorithm is based on the lookup table
440 approach with a pre-defined set of aerosol types, loadings and geometries [Floutsi et al. 2016].
441 A comprehensive description of retrieval algorithms and details of MODIS instrument are
442 found elsewhere [Remer et al. 2008; Levy et al. 2013]. MODIS AOD retrieval algorithms have
443 been substantially validated against in-situ and/or other remote sensing data sets from regional
444 to global scales and are updated periodically [Remer et al. 2008 ; Li et al. 2009]. The
445 uncertainty of AOD retrievals is estimated to be $\pm 0.05 \pm 0.20 \times \text{AOD}$ over land and $\pm 0.03 \pm 0.15$
446 $\times \text{AOD}$ over ocean [Remer et al., 2005; 2008]. The present study utilized Level 2 MODIS
447 aerosol products (Collection 6.1) obtained from the Atmosphere Archive and Distribution
448 System (LAADS DAAC). These products consist of 5-minute satellite swaths with a spatial
449 resolution of 10 km, covering the period of June and December 2022. (Devadiga, 2024).

450 **3.6 Satellite data processing**

451 In order to quantitatively compare the WRF-chem simulations with satellite measurements,
452 the model outputs must be processed using the appropriate method as described in the literature
453 (Kumar et al., 2012). Direct comparison between satellite retrievals and model outputs is not
454 recommended, as satellite measurements depend on column averaging kernels (AK) and a-
455 priori profiles. The AK vector, ~~representing~~ represents the vertical sensitivity of the retrieved
456 column ~~relative to the partial column~~ true vertical profile of the target variable in the
457 atmosphere. It indicates how changes in the true atmospheric profile at different vertical levels,
458 ~~should be employed to convolve the~~ influence the retrieved column values, allowing for a
459 ~~more accurate comparison between~~ model simulations, and TROPOMI data by convolving the
460 model outputs with the AK. The typical AK vectors are plotted over the WISE-UAE location
461 to know the sensitivity of AK at different pressure levels (Figure S7).

462 The column density from the WRF-Chem model is re-gridded to match the TROPOMI
463 instrument's grids and is vertically interpolated to the TROPOMI pressure levels before it is
464 multiplied by the AK. This treatment of the WRF-Chem-simulated profile with the column

Formatted: Font color: Auto

Formatted: Font color: Auto

Formatted: Font color: Auto

Formatted: Font color: Auto

Formatted: Font color: Auto

Formatted: Font color: Auto

Formatted: Font color: Auto

465 averaging kernels allows for a comparison that is independent of the chemical transport model
 466 (CTM) a-priori assumptions and the vertical sensitivity of the retrieval process; therefore, it
 467 can be directly compared with the TROPOMI-derived tropospheric column of NO₂. The
 468 TROPOMI-NO₂ and TROPOMI-CO products also provide a column averaging kernel matrix.
 469 In ~~the~~this case of TROPOMI-NO₂, the application of the column AK averaging kernel accounts
 470 for the vertical distribution and sensitivity of the measurements, as classically done by Borsdorff
 471 et al., (2014) as:

472
 473
$$X_{ret} = X_{a\ prior} + AK \times (X_{true} - X_{a\ prior}) + e_x \text{-----(1)}$$

Formatted: Centered

474 where, X_{true} is model simulation profile of trace gas; X_{ret} is the retrieved profile or smoothed
 475 model profile; e_x represents the error on the retrieved trace gas profile; $X_{a\ prior}$ is the a-priori
 476 information provided in the TROPOMI data set. For TROPOMI-NO₂ data, the contribution of
 477 the a priori profile and error on the retrieved profile can be eliminated, as explained in Borsdorff
 478 et al., (2014). ~~The~~In particular, eq. (1) simplifies to

479
$$X_{ret} = AK \times (X_{true}) \text{----- (2)}$$

Formatted: Centered

480
 481 where X_{true} represents WRF-Chem simulation profile for both NO₂ and CO, AK represents the
 482 averaging kernels information provided in the TROPOMI data set for NO₂ and CO and X_{ret}
 483 represents smoothed model profile for NO₂ and CO.

484 For validation of ozone ~~and CO total column~~, we have used the TROPOMI ozone ~~and CO~~
 485 profile level 2 data product S5P_OFFL_L2_O₃ ~~and S5P_OFFL_L2_CO~~ that provides
 486 the ozone ~~and CO~~ concentrations at ~~15 and 5033~~ pressure levels, ~~respectively~~. This data product
 487 also includes the a priori information and column averaging kernel for each pressure level. In
 488 order to compare our model profile with the one given by this dataset, the model output is
 489 horizontally and vertically interpolated to TROPOMI grids and vertical levels. The final model
 490 profile was calculated by the Eq. (3)

491
$$X_{ret} = X_{a\ prior} + AK \times (X_{true} - X_{a\ prior}) \text{-----(3)}$$

Formatted: Centered

492 where X_{true} represents WRF-Chem simulation profile for O₃, AK represents the averaging
 493 kernels information provided in the TROPOMI data, X_{ret} represents smoothed model profile
 494 for O₃ and $X_{a\ prior}$ is the a-priori information provided in the TROPOMI data. Since the highest
 495 vertical level in WRF-Chem-simulated trace gas concentration is 50 hPa, the remaining vertical
 496 layers of ozone and CO ~~were~~are made equal to the a priori concentration of respective trace
 497 gases as described by ATBD (Landgraf et al., 2016).

498 **3.57 Evaluation methodology**

499 Meteorological parameters from the WRF-Chem model ~~were~~are extracted for the grid points
500 closest to the surface observation sites of ~~NCM. Meteorological~~the AWS. As noted before, the
501 ~~meteorological~~ parameters ~~were~~are categorized and averaged for land and marine regions
502 ~~separately~~ for the regional analysis. ~~Consequently, further analyses based on these categories~~
503 ~~are presented in subsequent sections of the article.~~To enable ~~the~~ comparison of atmospheric
504 column data from the ~~TOPOMITROPOMI~~ satellite retrievals with WRF-Chem outputs, the
505 data must undergo smoothing through an appropriate method described in Section 3.4, as direct
506 comparison between satellite retrievals and simulations is not feasible due to discrepancies
507 highlighted in previous literature. Additionally, ~~and~~ owing to the spatial resolution differences
508 between WRF-Chem and ERA5 datasets, it is necessary to remap the model data to the ERA5
509 grids for accurate comparison. A wide range of statistical parameters is available for evaluating
510 model simulations. In this study, we employed statistical skill scores including the Pearson
511 correlation coefficient (r), the Mean Bias (MB), the Root Mean Square Error (RMSE), and the
512 Mean Absolute Error (MAE), which have been extensively discussed and applied in similar
513 contexts (Fonseca et al., 2021; Ivatt & Evans, 2020; Temimi et al., 2020b).
514 The following equations (eq. 4 to eq. 7) are used to calculate these statistical matrixes in the
515 present study,

516
517
$$r = \frac{\sum_{i=1}^N [(O_i - \bar{O}_i)(M_i - \bar{M}_i)]}{\sqrt{\sum_{i=1}^N (O_i - \bar{O}_i)^2 \sum_{i=1}^N (M_i - \bar{M}_i)^2}}$$

518
$$\frac{\sum_{i=1}^N [(O_i - \bar{O}_i)(M_i - \bar{M}_i)]}{\sqrt{\sum_{i=1}^N (O_i - \bar{O}_i)^2 \sum_{i=1}^N (M_i - \bar{M}_i)^2}} \text{-----(4)}$$

519
$$RMSE = \left(\frac{1}{N} \sum_{i=1}^N (M_i - O_i)^2 \right)^{\frac{1}{2}} \text{-----(5)}$$

520
$$MB = \frac{1}{N} \sum_{i=1}^N (M_i - O_i) \text{-----(6)}$$

521
$$MAE = \frac{1}{N} \sum_{i=1}^N |M_i - O_i| \text{-----(7)}$$

522
$$|O_i| \text{-----(7)}$$

Formatted: Font: 21 pt

524 where O_i denotes the i -th observation, M_i represents the corresponding WRF-chem [model](#)
525 simulated value, and N is the number of model and observation pairs. \overline{M}_t and \overline{O}_t are the
526 model and observational means (i.e. average of 1-30 June and 1-31 December), respectively.
527 The correlation coefficient (r) is an indication of the phase agreement between the modelled
528 and observed time-series. The RMSE measures the average error in the model ~~and predictions.~~
529 [while](#) the MAE determines the mean error between the model [forecasts](#) and observations
530 regardless of whether it is an under or overestimate. The MB is a measure of the systematic
531 error and gives information [as to](#) whether the model is over or underpredicting the
532 corresponding observed values.

533 4. Results and Discussion

534 4.1 Model performance for [key](#) meteorological variables

535 The ~~general ability capability~~ of the WRF-Chem model to reproduce realistic [spatio-](#)
536 ~~temporal~~[spatiotemporal](#) patterns of ~~the most relevant physical and chemical~~ [key meteorological](#)
537 variables ~~is has been~~ assessed by comparing the ~~simulated output with the model outputs to~~
538 observational [reanalysis](#) data for June and December ~~for the year 2018, reflecting the 2022,~~
539 ~~representing~~ contrasting summer and winter conditions over the UAE. ~~Determining~~[Evaluating](#)
540 the accuracy of WRF-Chem ~~simulations by validating~~ Chem's meteorological
541 ~~conditions~~[forecasts](#) in the study area is ~~crucial~~[essential](#) before ~~utilizing~~[applying](#) the model's
542 ~~output for~~ model forecasts to air quality [applications](#). ~~In this regard~~[assessments](#). Accordingly,
543 we ~~have conducted a comparison of~~ compared the model's [model predictions for](#) T2m, RH2m,
544 WS10m, and ~~SR outputs with~~ SW against ground-based observations at seven airport stations
545 ~~and in-situ~~ measurements from ~~observational data sets, the WISE-UAE field campaign (details~~
546 ~~in Table S1)~~. Additionally, ~~we have compared~~ the boundary layer height ~~from the model with~~
547 ~~the ERA5 reanalysis product. These is~~ evaluated against ERA5 reanalysis data, which offers a
548 [spatial resolution of approximately 28 km, higher than the other currently available reanalysis](#)
549 [datasets](#). Detailed results of this analysis are presented in the supplementary material, with key
550 [findings summarized here to support the paper's discussion](#). The aforementioned
551 [meteorological](#) parameters ~~were chosen due to~~ are selected, given their ~~significance~~[critical role](#)
552 in influencing ~~most air pollutants~~ [pollutant behavior](#) (Ritter et al., 2013). ~~Notably, the ERA5~~
553 ~~reanalysis data boasts a high spatial resolution of approximately 28 km, making it superior to~~
554 ~~other reanalysis datasets in this aspect~~. Our comparison involved analysing the hourly results

Formatted: Font color: Auto

Formatted: Font color: Auto

555 from both ERA5 and ground-based datasets against WRF-Chem for two distinct months in
556 2018. Detailed results of this comparison are presented below.

557 **4.1.1 Evaluation against *In-Situ* Observations**

558 The WRF-Chem model evaluation against observations across the seven meteorological
559 stations (Table S1) at the UAE airports for T2m, RH2m, and WS10m during June and
560 December 2022 reveals a close agreement between the modeled and observed values (Table
561 S2). The cold bias reported by several studies, including Branch et al. (2021), Temimi et al.
562 (2020a), and Abida et al. (2022), which occurs primarily at night, is reduced in the WRF-Chem
563 simulations presented here. In fact, and for the June month, the air temperature bias is positive,
564 ~0.2 °C. This stresses the importance of properly simulating the observed aerosol loading in
565 this hyper arid region. Deficiencies in the land surface-based observations model and radiation
566 schemes and in the representation of the surface properties, particularly the surface emissivity
567 that may be overestimated in the model (Parajuli et al., 2023), can also account for this
568 discrepancy. The WRF-Chem model also exhibits a noteworthy dry bias in this region, linked
569 to an incorrect simulation of the soil moisture and the mesoscale land-sea breeze circulation,
570 which is present in both seasons. The strength of the near-surface wind speed tends to be
571 overestimated in WRF-Chem in the UAE by about 1-3 m/s, which has been attributed to an
572 incorrect representation of its subgrid-scale variability and deficiencies in the surface drag
573 parameterization scheme (Nelli et al., 2020; Fonseca et al., 2020; Temimi et al., 2020b). Here,
574 the biases are much smaller, within 0.5 m/s. This, together with the improved representation of
575 the observed air temperature, reflects an overall improved simulation of the boundary layer
576 dynamics in the model.

577 The WRF-Chem model effectively represented the observed variations in T2m, WS10m,
578 and SR across all 16 meteorological stations during June and December 2018. The WRF-Chem
579 model generally underestimated T2m values by less than 0.5 °C in June and overestimated
580 them in December by less than 1.3 °C across the majority of locations. Correlation coefficients
581 for the observed T2m with model simulations were between 0.66 to 0.99 in June, slightly
582 increasing to a range of 0.70 to 0.99 in December. The MB for T2m varied from -0.04 to +1.19
583 °C in June and -2.17 to +0.50 °C in December, with the RMSE spanning from 0.8 to 5.9 °C in
584 June and 0.9 to 4.1 °C in December. Conversely, the outcomes for WS10m and SR
585 demonstrated variability across different stations. The model performance demonstrates
586 significant enhancements over previous research conducted in this region. For instance,
587 Fonseca et al., (2020) observed a warm bias of 1-3 °C in WRF simulations across the UAE for

Formatted: Font: 13 pt

Formatted: Normal, Indent: First line: 0.75 cm

Formatted: Font: 12 pt

Formatted: Font: 12 pt

588 both winter and summer seasons. This observation aligns with similar findings reported by
589 Schwitalla et al., (2020) and Wehbe et al., (2017). The enhanced performance of the model
590 may be attributed to the present model configuration which differs from that used in previous
591 studies.

592 We concentrate on evaluating the model's performance at a regional scale, as delineated
593 by land (encompassing 11 sites) and marine stations (comprising 5 sites), detailed in section
594 3.1.1. Table 3 presents an extensive evaluation of the statistical verification scores for essential
595 meteorological variables at these categories within the UAE. In the month of June, the model
596 slightly underestimated the T2m values in both land and marine settings, with a
597 underestimation of 0.37 °C and 0.48 °C, respectively, despite an overprediction of SR. This
598 arises because of colder temperatures in particular in the evening and night time hours, a bias
599 highlighted by other studies such as Temimi et al. (2020b) and Branch et al. (2021). This has
600 been attributed to deficiencies in the model's physics and/or dynamics, in particular in the land
601 surface model and surface properties, a cold bias in the forcing dataset, and an incorrect
602 representation of the concentration of aerosols and greenhouse gases. Despite this, the model
603 achieves notable correlation coefficients (r) of 0.91 for land regions and 0.83 for marine
604 regions. The lower correlation observed in marine regions possibly arises from the more muted
605 diurnal cycle (Fig. 2) and the model's inability to properly represent the complex land-sea mask
606 even at 3 km spatial resolution. Similar results were reported in Abida et al., (2022), where the
607 WRF model demonstrates improved accuracy in inland areas compared to offshore or coastal
608 regions. The RMSE (MAE) values stand at 3.57 °C (2.68 °C) for land and 1.67 °C (1.47 °C)
609 for marine regions, respectively. In December, the T2m predictions by the model show an
610 overestimation, marked by 0.76 °C in land and 1.30 °C in marine regions. The model maintains
611 strong correlations, with $r = 0.92$ for land and $r = 0.90$ for marine regions, underseoring its
612 consistent performance. The RMSE (MAE) values recorded are 2.87 °C (1.66 °C) for land and
613 2.57 °C (1.37 °C) for marine regions, illustrating the model's accuracy in capturing temperature
614 fluctuations over these regions. For WS10m, the model effectively aligns with observed values,
615 showing good agreement in both land and marine settings. In June, it slightly overestimated
616 the wind speed in the marine region by 0.51 m/s, a trend that is also reflected in the RMSE
617 metrics, which are marginally higher for marine areas compared to land (0.08 m/s). In
618 December, it notably overestimated wind speeds in marine regions by 0.92 m/s, while the
619 overestimation was slightly less in land areas, at 0.38 m/s. Despite this, the correlations remain
620 robust in both seasons, highlighting the model reliability in capturing wind speed variations

across different environments. The model representation of SR demonstrates a similar pattern of accuracy and overestimation. In June, the model tends to overestimate SR across both regions, which has been reported in Fonseca et al. (2020) and Temimi et al. (2020b), yet it achieves a more accurate depiction in December. A possible explanation is a reduced aerosol loading in the model, with the summer featuring higher atmospheric aerosol amounts than the winter season (Nelli et al., 2021), with WRF also exhibiting a tendency to underpredict the observed cloud cover in the region. Although the correlations for SR are slightly lower, especially in the marine regions, they still indicate a reasonable level of model performance. Overall, the model tends to overestimate WS10m and SR across both seasons, while it underestimates the T2m in winter and overestimates it in summer. Such variable performance of the model has been noted in findings from prior research (for example, Schwitalla et al., 2020; Wehba et al., 2017; Fonseca et al.,

The WRF-Chem model evaluation against WISE-UAE measurements (detailed in Table S3 and Fig. S1) reveals a comparable performance to that seen concerning the seven airport stations. SW observations are also available for this site. An evaluation against the WRF-Chem values reveals the model overestimates the incoming shortwave radiation flux by about 30 W/m² for December, which can be attributed to reduced cloud cover, a known WRF deficiency (Wehbe et al., 2019; Fonseca et al. 2020, 2022a). An inspection of the diurnal cycle revealed the cold (typically by 2-3 °C) and dry (by about 20%) biases occur mostly at night, when the wind speed in the model is higher than that observed, suggesting increased advection of cooler and drier desert air into the site.

2020; Abida et al., 2022). Furthermore, a more detailed analysis of the biases identified in T2m and WS10m, including an examination of the diurnal variation of these parameters, is presented in the following sections.

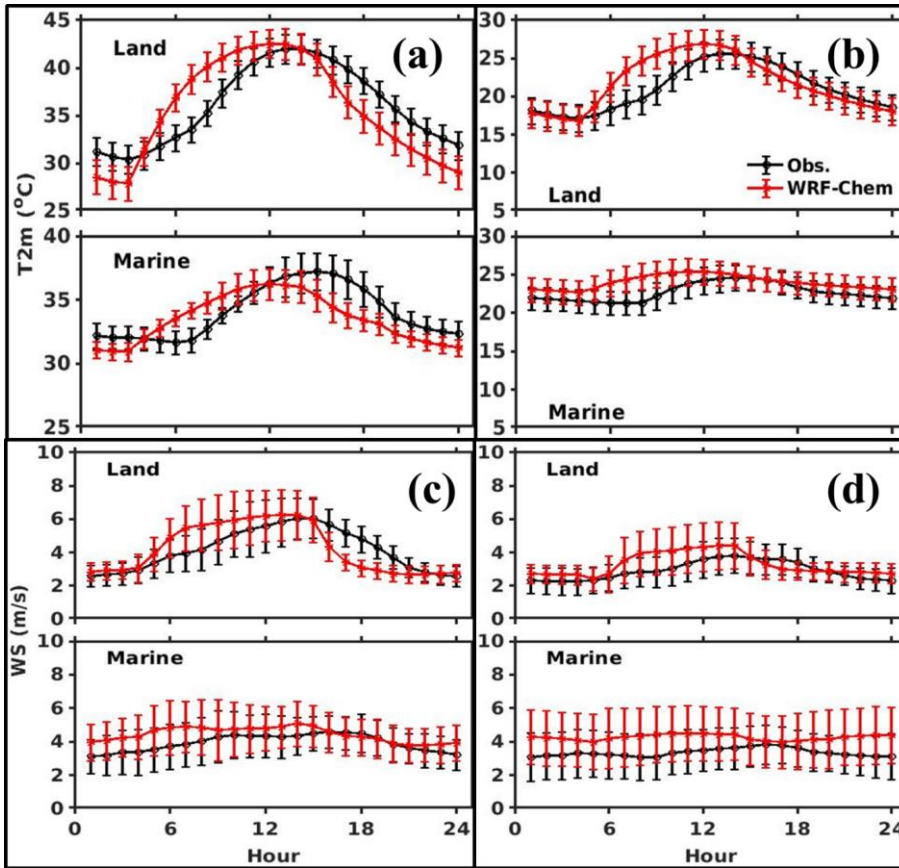
Table 3: Statistical verification scores for evaluation against weather station data: skill scores for air temperature at 2m (T2m), wind speed at 10m (WS10m) and downward shortwave radiation flux (SR) for 16 meteorological stations (categorised into land and marine regions) over the United Arab Emirates (UAE).

Parameter	Month	Region	MOD	OBS	MB	MAE	R	RMSE
T2m (°C)	June	Land	35.70	36.07	-0.37	2.68	0.91	3.57
		Marine	33.54	34.03	-0.48	1.47	0.83	1.67
	Dec	Land	21.84	21.08	0.76	1.66	0.92	2.87
		Marine	24.02	22.72	1.30	1.37	0.90	2.57

WS10m (m/s)	June	Land	4.24	4.16	0.08	0.90	0.88	1.35
		Marine	4.44	3.92	0.51	1.01	0.78	1.09
	Dec	Land	3.29	2.91	0.38	0.63	0.88	0.95
		Marine	4.26	3.35	0.92	1.12	0.89	1.54
SR (W/m ²)	June	Land	352.0	279.7	72.4	197.1	0.87	327.1
		Marine	349.3	264.9	84.4	273.4	0.68	358.7
	Dec	Land	192.7	177.2	15.5	124.3	0.85	231.2
		Marine	183.8	171.7	12.1	188.8	0.59	240.7

649

650 Figure 2, (a) and (b), presents a comparative analysis of the average diurnal variation in T2m
651 from WRF-Chem simulations and observations at both land and marine sites investigated in
652 this study, for the summer and winter seasons of 2018, respectively. The observed and
653 modelled T2m data exhibit a close alignment over land and marine locations, although some
654 discrepancies are evident. During the daytime, there is a tendency for the model to exhibit a
655 warm bias, while at night and evening, a cold bias is more apparent. Such discrepancies in
656 temperature have been reported before (Abida et al., 2022; Branch et al., 2021; Fonseca et al.,
657 2021; Schwitalla et al., 2020; Temimi et al., 2020a). Overall, the WRF-Chem model displays
658 a consistent cold bias of less than 0.5 °C for both environments during the summer months. In
659 contrast, during winter, the model shows a warm bias ranging from 0.8 to 1.3 °C. This is in
660 contrast to findings by Branch et al. (2021), which indicated an increase in the nocturnal cold
661 bias from winter to summer. Conversely, our study identifies a cold bias in the summer and a
662 warm bias in the winter, persisting throughout the entire day over marine locations. The
663 decrease in cold bias observed during summer in WRF-Chem simulations is a result of
664 enhanced representations of updated surface and soil parameters over the study region.



665
 666 **Figure 2: Air temperature and wind speed diurnal cycle:** Diurnal cycles of spatial mean values of
 667 WRF chem simulated (red) and observed (blue) air temperature at 2m (T2m; °C) in (a) (summer) and
 668 (b) (winter) for the regional categories of land and marine sites (c) (d) are as (a) (b) but for the wind
 669 speed at 10 m (WS10m; m/s). The averaged spatial standard deviation is represented by an error bar at
 670 each hour.

671 Figure 2, (c) and (d), show a comparative analysis of the mean diurnal variation in WS10m
 672 from model simulations and observations at both land and marine sites examined in this study,
 673 during the summer and winter of 2018, respectively. In both seasons, higher wind speeds are
 674 observed over marine sites, while lower wind speeds are found over land sites, reflecting sea
 675 and land circulations, respectively. It is indicated that wind speeds are higher during the
 676 daytime and lower during the night and evening hours. This pattern is especially pronounced
 677 over land sites compared to marine sites during both seasons. WRF Chem tends to overestimate

678 WS10m during both day and night, across all regions and seasons. Nonetheless, the model
679 shows the smallest discrepancies over land, with biases being the least significant at 0.1 m/s
680 during summer and 0.4 m/s in winter. In contrast, the biases over marine areas are more
681 pronounced, at 0.5 m/s in the summer and 0.9 m/s in the winter. WRF-Chem tends to
682 overestimate WS10m more significantly during winter, with less overestimation observed
683 during summer. This discrepancy is linked to alterations in wind direction driven by land and
684 sea breeze circulations. Consequently, numerous studies have previously emphasized the
685 model's tendency for wind speed overprediction (Abida et al., 2022; Branch et al., 2021;
686 Fonseca et al., 2021; Schwitalla et al., 2020; Temimi et al., 2020a).

687 **4.1.2 Evaluation against ERA5 reanalysis data**

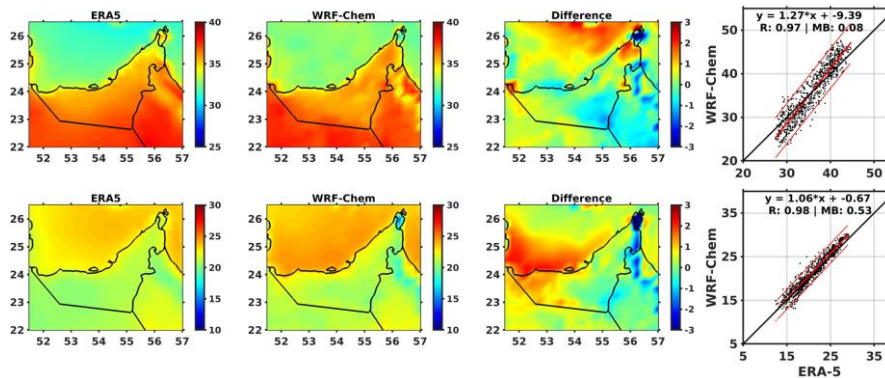
688 The WRF-Chem model predictions are also evaluated against ERA5 reanalysis data for
689 T2m, WS10m, SW, and PBL during June and December 2022. The air temperature biases are
690 within 1 °C, with a cold bias present in both months, more pronounced over inland areas, with
691 correlation coefficients 0.9 (Fig. S2). It is important to note that ERA5 overestimates the
692 temperature at night and underestimates it during the day typically by 1-2 °C in the country for
693 all seasons (Nelli et al., 2024a), meaning the cold bias shown by WRF-Chem does not
694 necessarily indicate a poorer performance. The skill scores for WS10m and SW are also similar
695 to those estimated concerning the station observations and the WISE-UAE field measurements.
696 For the PBL height, the model reproduces its spatial and seasonal variations (Fig. S3), largely
697 driven by the temperature seasonal cycle (cf. Figs. S2; Basha et al., 2019). In Fig. 3, a spatial
698 comparison is presented between the averaged ERA5 T2m and the corresponding WRF chem
699 simulation output across the simulation domain during June and December of 2018. The model
700 adeptly captures regional temperature variations, displaying underestimation in the southern
701 regions and overestimation in the north-western region of the UAE. This observation suggests
702 a comprehensive portrayal of temperature dynamics by the model, with specific tendencies in
703 certain geographical areas. This observation is also supported by NCM data, for instance, at
704 Mezaria (ID No: 3), which represents a southern land site, and at Abu Dhabi (ID No: 15),
705 representing a northern marine site within the emirate of Abu Dhabi. The southern land site
706 found an underestimation of 1°C, while the northern marine site exhibited an overprediction of
707 T2m by WRF chem. WRF Chem overestimates the area-averaged temperature (T2m) over the
708 UAE compared to ERA5 in both seasons. In contrast, NCM observations indicate an
709 underestimation during the summer and an overestimation during the winter across the majority
710 of sites. Kishta et al., (2023) reported that, minor discrepancies in temperature measurements

Formatted: Font: 13 pt

Formatted: Font: 13 pt

711 between observational data and ERA5 reanalysis, identifying a strong correlation coefficient
712 of 0.89 over Abu Dhabi. The spatial average of WRF Chem and ERA5 values are 35.8 °C and
713 35.7 °C, respectively, with a small underestimation of 0.08°C over the UAE. The model
714 displays a high correlation (r) of 0.97 and a RMSE of 2.3 °C, MAE of 2.2 °C in June. For
715 December, the model showed a similar pattern, with a underestimation of 0.53 °C which is
716 slightly higher as compared to June, r of 0.98, MAE of 1.0 °C and RMSE of 1.1 °C (Table 4).

717 Moreover, the analysis of the absolute differences between the two datasets highlighted the
718 most pronounced discrepancies over the Arabian Gulf region, observable in both the summer
719 and winter months. However, these discrepancies are notably more emphasised during the
720 warmer months. WRF simulated Sea Surface Temperatures (SSTs) are compared with both
721 ERA5 and Group for High Resolution Sea Surface Temperature (GHRSSST) data over the
722 Arabian Gulf region (not shown). The comparison involved area averaged daily values,
723 considering that the diurnal amplitude of SST is 0.5 °K over this region as reported by Nesterov
724 et al., (2021). The model showed an overestimation of 1.4 °K compared to both ERA5 and
725 GHRSSST during the summer. Similarly, in winter, its overestimated SSTs by 1.5 °K compared
726 to ERA5 and by 1.3 °K compared to GHRSSST. Furthermore, the model exhibited a
727 significantly higher correlation in winter, achieving a correlation coefficient of 0.9 with both
728 datasets. However, during the summer, it displayed variable correlations, with $r=0.38$ for ERA5
729 and $r=0.20$ for GHRSSST. This observation suggests potential inaccuracies in the model
730 simulation of temperature and wind speed in this region, which could be due to the sea surface
731 temperature data utilized for model forcing. The temperature gradient plays a pivotal role in
732 driving the land sea breeze circulation. Higher temperatures observed over the Gulf could
733 potentially weaken this circulation pattern, resulting in reduced transportation of cleaner
734 marine air towards inland areas. Consequently, this reduction in the influx of marine air could
735 obstruct the effective dispersion of pollutants across terrestrial regions, negatively impacting
736 air quality and the spatial distribution of pollutants.



737
 738 [The PBL height, and over land areas, ranges from 2400-2500 m in the summer during the day](#)
 739 [to less than 500 m in winter at night. Over the Arabian Gulf, the PBL is deeper in the winter](#)
 740 [months in both ERA-5 and WRF-Chem \(800 m vs. 200 m\), owing to stronger winds and](#)
 741 [enhanced turbulent mixing \(Dai, 2024\).](#)

742 [This comprehensive evaluation of the predicted meteorological parameters against those](#)
 743 [observed at seven UAE airport sites, the WISE-UAE experimental site, and ERA5 reanalysis](#)
 744 [data demonstrates that WRF-Chem reliably captures them, including their spatial and seasonal](#)
 745 [variations across the UAE. As WRF-Chem integrates meteorological and chemical processes,](#)
 746 [precise meteorological simulations are essential to ensure accurate chemical computations](#)
 747 [within the model domain.](#)

748
 749 **Figure 3: ERA-5 and WRF-Chem Air Temperature:** Average 2 m air temperature (°C) obtained
 750 [from ERA5 reanalysis \(first panel\), simulated by WRF-Chem \(second panel\), and the corresponding](#)
 751 [absolute differences \(third panel\) and scatter plots between the two datasets \(fourth panel\) during June](#)
 752 [\(top\) and December \(bottom\) 2018.](#)

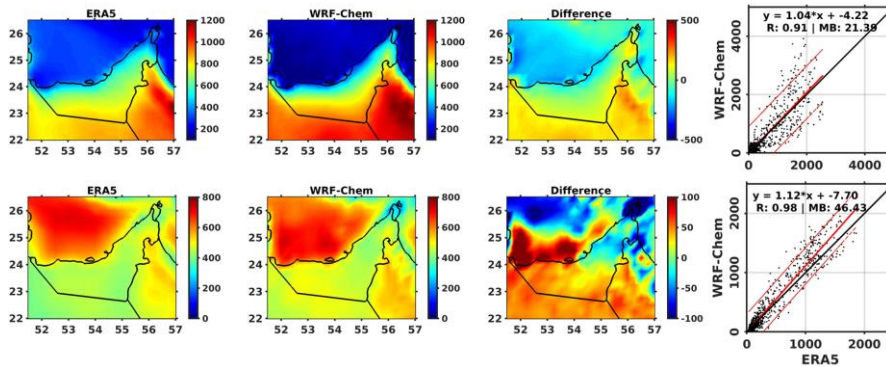
753 [It is widely recognized that the Planetary boundary layer \(PBL\) plays a crucial role in the](#)
 754 [pollution transport process over the region. It constitutes the lowest part of the troposphere and](#)
 755 [is directly influenced by the Earth's surface. The PBL reaches higher elevations during summer,](#)
 756 [with its altitudes being lower in winter. There are noticeable differences in the PBL between](#)
 757 [land areas \(approximately 2400–2500 m\) and marine regions \(about 1200–1500 m\) \(Basha et](#)
 758 [al., 2019\). Basha et al. \(2019\) also discovered that ERA-Interim reanalysis data tend to](#)
 759 [underestimate PBL when compared with data obtained from Global Positioning System Radio](#)

Formatted: Space After: 8 pt

Formatted: Font: 12 pt, Not Bold

760 Occultation (GPSRO) in most regions and in all the seasons. Chen et al., (2022) emphasized
761 the critical role of the boundary layer in influencing air quality and facilitating the
762 transboundary transport of pollutants. They noted that a higher boundary layer enhances the
763 potential for pollutant transport to the Tibetan Plateau. Wang et al., (2022) highlighted the
764 critical role of meteorological conditions in severe PM_{2.5} pollution episodes. They noted that
765 rapid cold air movement can quickly disperse pollutants, in contrast to the slow accumulation
766 of pollutants under weak high pressure systems. This slow build up is characterized by low
767 wind speeds, and low atmospheric boundary layer heights, which lead to prolonged heavy
768 pollution periods.

769 In this study, we aim to compare the PBL as simulated by WRF Chem with the ERA5
770 reanalysis, providing further specifics of model accuracy and performance. Fig. 4 shows a
771 comparison of the mean ERA5 PBL with corresponding WRF chem simulated values over the
772 UAE for the months of June and December 2018. The absolute difference and scatter plot for
773 these data sets are also shown. The spatial distribution of PBL across the UAE, as from ERA5
774 data, exhibits a consistent spatial pattern that aligns with the PBL simulated by WRF Chem.
775 There is a notable trend of increased PBL during the summer months and decreased PBL in the
776 winter. This pattern generally corresponds with the seasonal temperature variations, where
777 warmer summer temperatures contribute to an elevation in PBL, and cooler winter
778 temperatures result in a reduction of PBL (Basha et al., 2019). In terms of PBL (averaged
779 spatially for the UAE), the model exhibits good performance in capturing the regional
780 variations. In June, the modelled PBL is at 669.8 m compared to 646.7 m in ERA5, with a
781 correlation coefficient of 0.91 and a RMSE of 450.1 m. In December, the modelled PBL is
782 490.5 m compared to the ERA5 of 444.2 m, with a high correlation coefficient of 0.98 and an
783 RMSE of 152.8 m (Table 4).



784
 785 **Figure 4: ERA-5 and WRF-Chem Boundary Layer Height:** Same as Fig. 3, but for planetary
 786 boundary layer height (PBL).

787
 788 In addition to T2m and PBL, Table 4 also summarizes the spatially averaged statistical
 789 verification scores for WS10m and SR over UAE. Regarding WS10m, it is accurately
 790 simulated by the model with small differences in MB (June: 0.08 m/s, Dec: 0.01 m/s), which
 791 are slightly larger compared to observations from land-based sites in Abu Dhabi and good
 792 correlations (June: 0.79, Dec: 0.80). The RMSE values are 1.7 m/s for June and 1.1 m/s for
 793 December. For SR, the model performs well, capturing the variability in radiation flux. In June,
 794 the modelled SR is 643.6 W/m² compared to the ERA5 of 576.5 W/m², with a high correlation
 795 of 0.99 and an RMSE of 75.3 W/m². Similarly, in December, the modelled SR is 460.8 W/m²
 796 compared to the ERA5 of 438.1 W/m², with a correlation of 0.97 and an RMSE of 76.1 W/m².
 797 Overall, these results indicate a very good performance of the WRF-chem model in simulating
 798 meteorological parameters over the UAE during the specified months. This rigorous evaluation
 799 of meteorological parameters showed that WRF-Chem's simulated values closely align with
 800 both ground-based and reanalysis datasets. Since WRF-Chem simulates meteorology and
 801 chemistry simultaneously, accurate meteorological simulations are crucial for the precise
 802 computation of chemistry within the model domain.

803
 804 **Table 4: Statistical verification scores for evaluation against ERA-5 data:** skill scores calculated
 805 for model simulations for air temperature at 2m (T2m), wind speed at 10m (WS10m), downward
 806 shortwave radiation flux (SR) and planetary boundary layer (PBL) during June and December of 2018
 807 over the United Arab Emirates.

808

Parameter	Month	MOD	ERA5	MB	MAE	R	RMSE
T2m(°C)	June	35.82	35.73	0.08	2.17	0.97	2.28
	Dec	21.61	21.08	0.53	0.99	0.98	1.12
WS10m (m/s)	-	4.34	4.26	0.08	1.26	0.79	1.7
	-	3.05	3.07	0.01	0.87	0.8	1.1
SR (W/m ²)	-	643.6	576.5	67.1	85	0.99	75.3
	-	460.8	438.1	22.8	69.5	0.97	76.1
PBL (m)	-	669.8	646.7	21.4	271.6	0.91	450.1
	-	490.5	444.2	46.4	113.8	0.98	152.8

809

810 4.2 Model performance ~~with respect to~~ for the gaseous pollutants

811 The study incorporates comparative assessments with satellite data from the TROPOMI
812 instrument. ~~This includes, including~~ evaluations of the tropospheric column of NO₂ (denoted
813 as TROPOMI-NO₂), total column CO (TROPOMI-CO), and ~~total tropospheric~~ column ozone
814 (TROPOMI-O₃) for the corresponding periods within the UAE. ~~Detailed outcomes of these~~
815 ~~comprehensive assessments are discussed in the following subsections. The WRF-Chem model~~
816 ~~exhibited commendable proficiency in replicating the satellite-derived measurements of these~~
817 ~~pollutants throughout the UAE over the summer and winter seasons of 2018.~~ The satellite
818 overpass takes place daily at 13:30 local time; therefore, model simulations corresponding to
819 this time are utilized here for comparison over the study area. After smoothing the model
820 concentrations using the a priori and averaging kernel matrix, as detailed in Section 3.4, the
821 results ~~were~~ are compared with the corresponding TROPOMI products.

822

823 In the troposphere, ~~oxides of nitrogen~~ oxides (NO_x = NO + NO₂) are ~~crucial~~ vital
824 for ~~the mechanisms of~~ ozone production and depletion processes in ~~the presence of~~ sunlight.
825 Due to their ~~shorter~~ relatively short lifespan, ~~their~~ NO_x concentrations are primarily closely
826 linked to emission sources. ~~As a result, NO_x is more susceptible, making them highly sensitive~~
827 to inaccuracies in emission estimates compared to other ~~criteria~~ pollutants. In our model setup,
828 we adopt the recommendation of Emmons et al. (2010), assigning 10% of NO_x emissions as
829 NO₂. As a result, the model tends to underestimate TROPOMI NO₂ levels, particularly in
830 regions with high emission sources, such as urban centres. The Environment Agency – Abu
831 Dhabi (2018) reported that oil and gas, road transport, and electricity generation are the primary

sectors contributing to NO_x total emissions, accounting for 42%, 34%, and 13%, respectively, for the base year of 2015 in the Emirate of Abu Dhabi. In Fig. 5.2 presents the average spatial distributions of both absolute differences between the model-simulated and the TROPOMI-retrieved tropospheric column NO₂ are presented. Additionally, the spatial discrepancies between simulated and retrieved columns are illustrated by absolute differences (see third row) and scatter plots between the two datasets are depicted (see fourth row) for June (left) and December (right) 2018 across the study region, and histograms of relative frequency. The satellite retrievals indicated elevated levels of NO₂ columns, exceeding 1.2×10^{15} molecules/cm², in densely populated and industrial areas and the adjacent regions to the major cities of Dubai and Abu Dhabi in both summer and winter. (Fig. S4). Conversely, lower NO₂ values, less than 1.5×10^{15} molecules/cm², were observed over the less urbanized areas. The higher columns are associated with significant economic development driven by a high demand in power generation and water desalination projects, which primarily depends on the combustion of fossil fuels in big cities like Dubai and Abu Dhabi (Abuelgasim & Farahat, 2020; Li et al., 2010). The model effectively reproduced the spatial distributions of NO₂ during the summer and winter of 2018-2022 as depicted in Fig. 5. Although, the model overestimation is close to zero. Even though the biases are positive in rural areas, it can be as high as 10^{16} the observed column NO₂ concentration is underestimated by up to 2×10^{15} molecules/cm² in areas of high pollution, specifically over Dubai and Abu Dhabi. Conversely, it underestimates up to 10^{16} molecules/cm² in the heavily populated north-eastern UAE, in particular around Ras Al Khaimah emirate, and Dubai (Fig. 2a) the sixth-largest city by population in the country and home to the global ceramic manufacturing company, RAK Ceramics. This observation is not unexpected, as urban and industrial areas frequently report elevated pollutant emissions stemming from urban activities, which are significantly high and present challenges that models often struggle to accurately capture these changes. This discrepancy also suggests that anthropogenic and industrial emissions might be improperly represented in the EDGAR emission inventory, at least for the UAE. Challenges range from the incomplete characterization of emissions in source regions to the impact of model resolution on capturing sub-grid emission sources. Besides deficiencies in the emission sources, other reasons may explain the model's underperformance in this region. Additionally, Hoshyaripour et al. (2016) found that the PBL is shallower and more stable at night when simulated with the YSU boundary layer scheme used in the WRF-Chem runs, resulting in a higher accumulation of NO_x in the surface layers. Such insights were constrained in the present model. As the

Formatted: Not Superscript/ Subscript

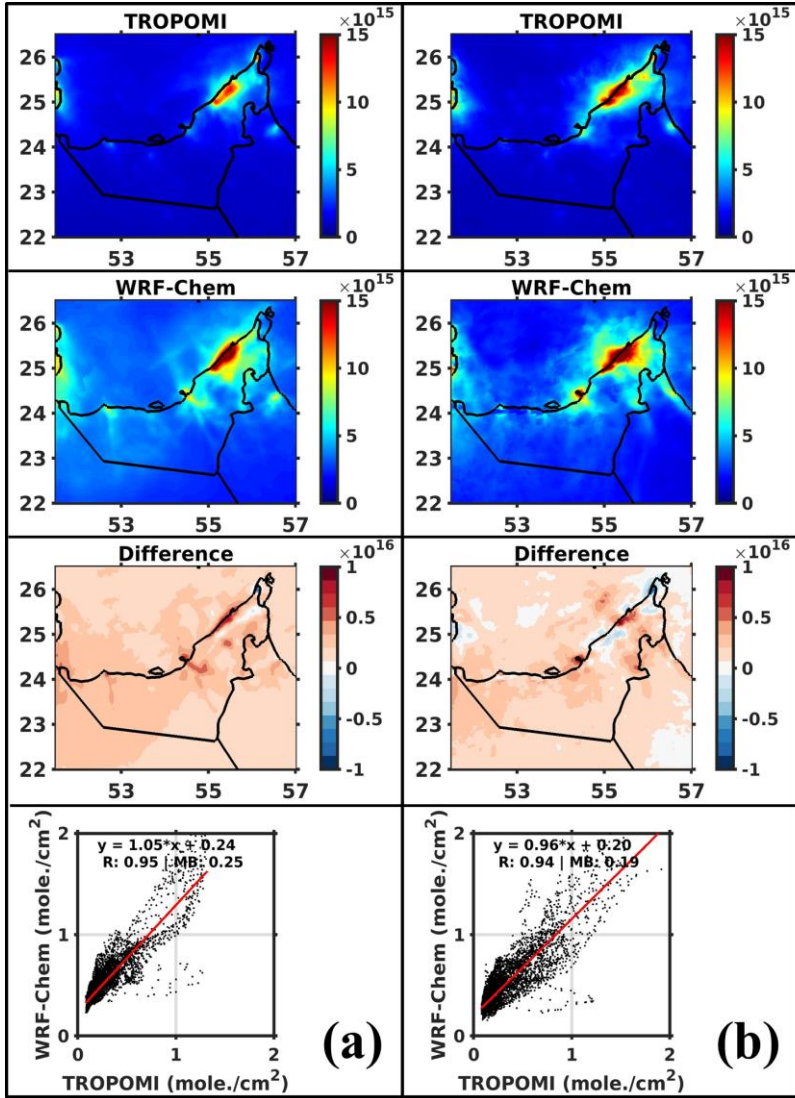
Formatted: Not Superscript/ Subscript

866 evaluation, ~~which conducted here against satellite observations~~ is ~~primarily focusing on~~
867 ~~temporal variability of gaseous pollutants on a daily basis, and did not encompass diurnal~~
868 ~~variations. Incorporating these diurnal variations, an incorrect representation of the~~
869 ~~atmospheric dynamics will be reflected in future model simulations over this region may~~
870 ~~enhance the assessment's accuracy~~ the WRF-Chem predictions. Additionally, the existing
871 model configuration does not include the formation of secondary aerosols ~~in its simulations~~,
872 indicating a potential area for improvement in future versions. ~~Additionally, the~~ The absence of
873 ~~a~~ vertical distribution of anthropogenic emissions in the model simulations also plays a pivotal
874 role in these model discrepancies. The satellite retrieved TROPOMI-NO₂ averaged for the
875 ~~UAE d03~~ is ~~0.241.1~~ $\times 10^{16}$ molecules/cm² in summer and ~~0.241.03~~ $\times 10^{16}$
876 molecules/cm² in winter. ~~The, with the~~ corresponding model simulated column ~~is~~
877 ~~0.46~~ concentration of 1.6×10^{16} and ~~0.431.2~~ $\times 10^{16}$ molecules/cm², respectively. The
878 model demonstrated a ~~strong~~ moderate correlation with satellite ~~derived~~ NO₂ column
879 measurements, achieving correlation coefficients of 0.9559 for summer and 0.9458 for winter
880 (refer to Table S2). It ~~showed a slight tendency tended~~ to overestimate NO₂ levels more in
881 summer, with a discrepancy of 0.245×10^{15} , compared to 0.492×10^{15} molecules/cm² in winter.
882 Moreover, the evaluation shows RMSE values of 0.42×10^{15} to 0.421×10^{15} molecules/cm²
883 and MAE values of 0.207×10^{15} to 0.255×10^{15} molecules/cm² during the seasons. ~~The~~
884 ~~frequency distributions in Fig 2(c) and (f) illustrate the differences in NO₂ concentrations~~
885 ~~between the WRF-Chem model and TROPOMI observations during summer and winter,~~
886 ~~respectively. In panel 2(c), the distribution of differences is entirely positive, indicating that~~
887 ~~the WRF-Chem model consistently overestimates NO₂ concentrations compared to TROPOMI~~
888 ~~observations for the summer of 2022. In contrast, Fig. 2(f) shows both positive and negative~~
889 ~~differences, indicating that the WRF-Chem model exhibits a mix of overestimations and~~
890 ~~underestimations of NO₂ concentrations in winter, although the majority of differences are still~~
891 ~~positive. This suggests a more variable alignment between WRF-Chem and TROPOMI-NO₂~~
892 ~~in winter, with a general tendency toward overestimation but occasional instances of~~
893 ~~underestimation.~~

894

Formatted: Font: 14 pt

Formatted: Space After: 8 pt



895

896 **Figure 5: Evaluation of WRF-Chem against satellite-derived NO₂: average spatial pattern of**
 897 **tropospheric column NO₂ (mole./cm²) obtained from TROPOMI satellite (1st row), simulated by WRF-**
 898 **Chem (2nd row), corresponding absolute difference (model minus TROPOMI) (3rd row) and scatter plots**
 899 **between two daily data sets (4th row) during (a) June and (b) December in 2018.**

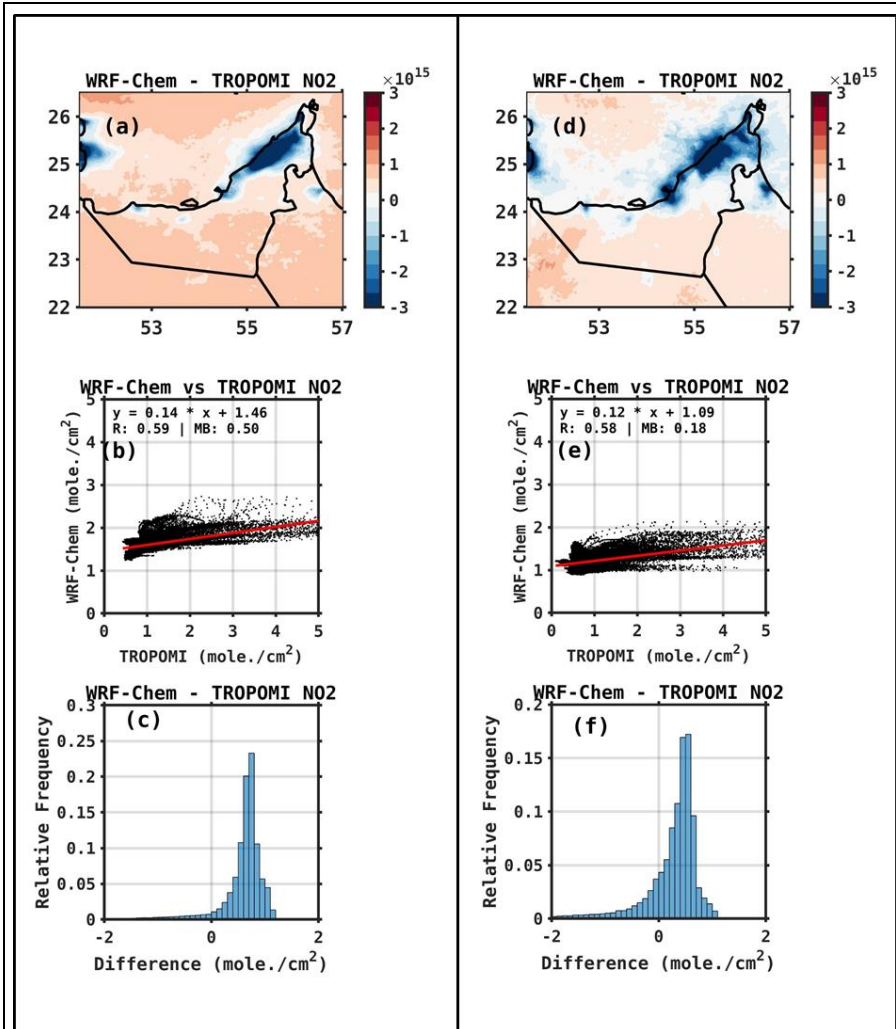


Figure 2: Evaluation of WRF-chem against satellite-derived NO₂: The average difference between tropospheric column NO₂ (mole/cm²) from the TROPOMI satellite and simulated by WRF-Chem, for (a) June and (d) December 2022. (b)-(e) and (c)-(f) are as (a) and (d) but showing scatter plots and histograms of the differences, respectively.

900

901 In Fig. 63, the average spatial distributions assessment of both the model-simulated and
 902 TROPOMI-retrieved total CO column are CO and the corresponding TROPOMI-retrieved
 903 values is presented. Also, the absolute difference of WRF-Chem simulations with TROPOMI-

Formatted: Font: 14 pt

Formatted: Space After: 8 pt

Formatted: Indent: First line: 0 cm

904 ~~CO is depicted along with scatter plots between them during summer and winter of 2018 over~~
905 ~~UAE.~~ The statistical metrics comparing these datasets are provided in Table 5-2. Fig. S5, shows
906 ~~the comparison of total column CO concentrations over the domain as observed by the~~
907 ~~TROPOMI satellite and simulated by the WRF-Chem model (. Panels (a) and (c) display~~
908 ~~TROPOMI-CO for summer and winter, showing spatial variations in CO concentration across~~
909 ~~the region. High concentrations, particularly over the northern areas, while lower~~
910 ~~concentrations found the southern areas. Panels (b) and (d) illustrate corresponding WRF-~~
911 ~~Chem CO simulations for the same periods, providing a model-based estimate of CO~~
912 ~~distribution. The WRF-Chem model appears to capture the general spatial patterns observed~~
913 ~~by TROPOMI, though there may be some discrepancies in the intensity and precise locations~~
914 ~~of high CO concentrations. This comparison highlights areas where the WRF-Chem model~~
915 ~~aligns well with satellite observations and regions where further adjustments in model~~
916 ~~parameters may be necessary to better replicate observed patterns.~~ The TROPOMI-retrieved
917 CO columns display values of 1.8792×10^{18} and 1.8979×10^{18} molecules/cm² for summer and
918 winter, respectively. In contrast, the simulated ~~columns show column~~ values are of $2.351.93 \times$
919 10^{18} for summer and $0.761.91 \times 10^{18}$ molecules/cm² for winter. Thus, comparing WRF-Chem
920 and TROPOMI-CO data reveals more pronounced discrepancies, with a minor overestimation
921 of 0.4802×10^{18} molecules/cm² in summer and a significant underestimation of $1.130.12 \times 10^{18}$
922 molecules/cm² in winter. -Shami et al., (2022) ~~discovered found~~ that the EDGAR emissions
923 inventory underestimates CO emissions when compared to Lebanon's national emission
924 inventory, identifying the road transport sector as the primary source of CO emissions.
925 Consequently, EDGAR's estimates for CO emissions are lower than those provided by Waked
926 et al., (2012) for the same region. The Environment Agency – Abu Dhabi (2018) reported that
927 the road transport sector is the primary source of CO emissions in Abu Dhabi, accounting for
928 74% of the total CO emissions. Additionally, the industrial sector contributes 21% to the total
929 CO emissions. Kumar et al. (2022) observed an underestimation of CO by the WRF-Chem
930 model, attributing it to an inaccurate representation of anthropogenic emissions on the vertical
931 scale, ~~not represented in the current WRF-Chem simulations as noted for NO₂.~~ This could
932 result in a more rapid deposition of CO molecules at the surface, thereby leading to the
933 observed underestimation. ~~In the summer months, the underprediction of the column CO over~~
934 ~~coastal areas, in particular around the major urban centers, and the overprediction over inland~~
935 ~~regions suggests deficiencies in the representation of the atmospheric flow (e.g., a too strong~~
936 ~~onshore flow), coupled with the aforementioned biases in the emission inventory. In contrast,~~

Formatted: Superscript

Formatted: Superscript

937 [in winter the biases are positive, and probably more strongly linked to chemistry than to](#)
938 [meteorological dynamics.](#)

939 The model output correlates reasonably well with TROPOMI-CO with [a correlation](#)
940 [coefficient](#) of ~~0.7182~~ and ~~0.86~~ ~~while~~ ~~40~~ and an RMSE of ~~0.04 to 0.0203~~ $\times 10^{18}$ and 0.04×10^{18}
941 molecules/cm² in summer and winter, respectively (Table ~~5~~~~-2~~). [The frequency distribution in](#)
942 [Fig. \(c\) shows most differences, with a slight positive skew, suggesting a tendency for the](#)
943 [WRF-Chem model to slightly overestimate CO concentrations compared to TROPOMI](#)
944 [observations for summer. In both contrast, Fig. \(f\) displays a broader distribution with a more](#)
945 [pronounced positive skew, indicating larger and more variable overestimations by WRF-Chem](#)
946 [in winter. In winter](#) seasons, the lower correlation coefficients [and higher biases](#) for
947 TROPOMI-CO as compared to TROPOMI-NO₂ ~~suggest a less robust linear relationship~~
948 ~~between the TROPOMI and WRF chem CO levels. This variation in performance~~ might be
949 attributed to the complexities inherent in [modelling](#)~~modeling~~ and observing CO distributions,
950 which ~~can be influenced by~~ local emission sources, atmospheric chemistry, and transport
951 processes [can influence](#). These findings are consistent with research conducted in India, where
952 Dekker et al. (2019) reported a correlation of 0.81 between TROPOMI and WRF-Chem CO
953 levels during a high pollution episode ~~during~~in November 2017. Similarly, in East Asia, Zhang
954 et al. (2016a) documented correlations between WRF-Chem simulated and [the Measurements](#)
955 [of Pollution in the Troposphere \(MOPITT\)-retrieved CO columns, with a r-value](#) of 0.59 and
956 RMSE of 4.6×10^{17} molecules/cm² for summer, and 0.69 with RMSE of 5.2×10^{17}
957 molecules/cm² for winter, respectively.

958

Formatted: Subscript

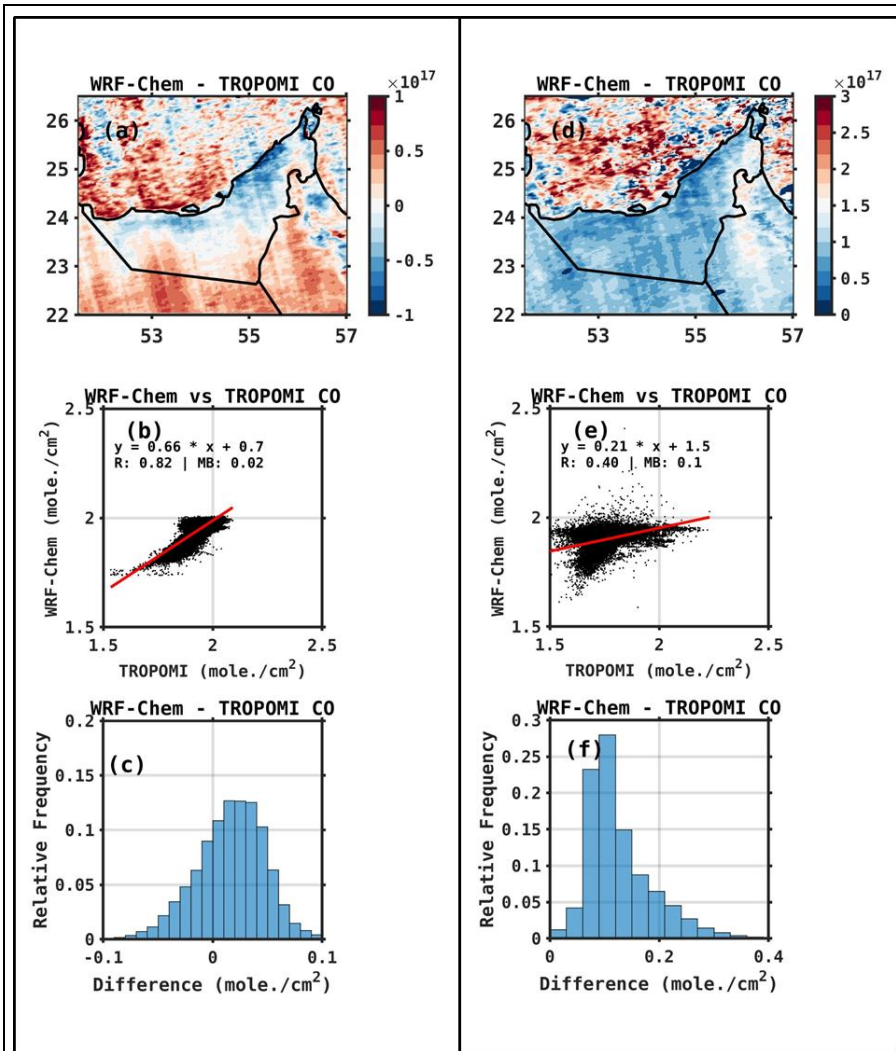
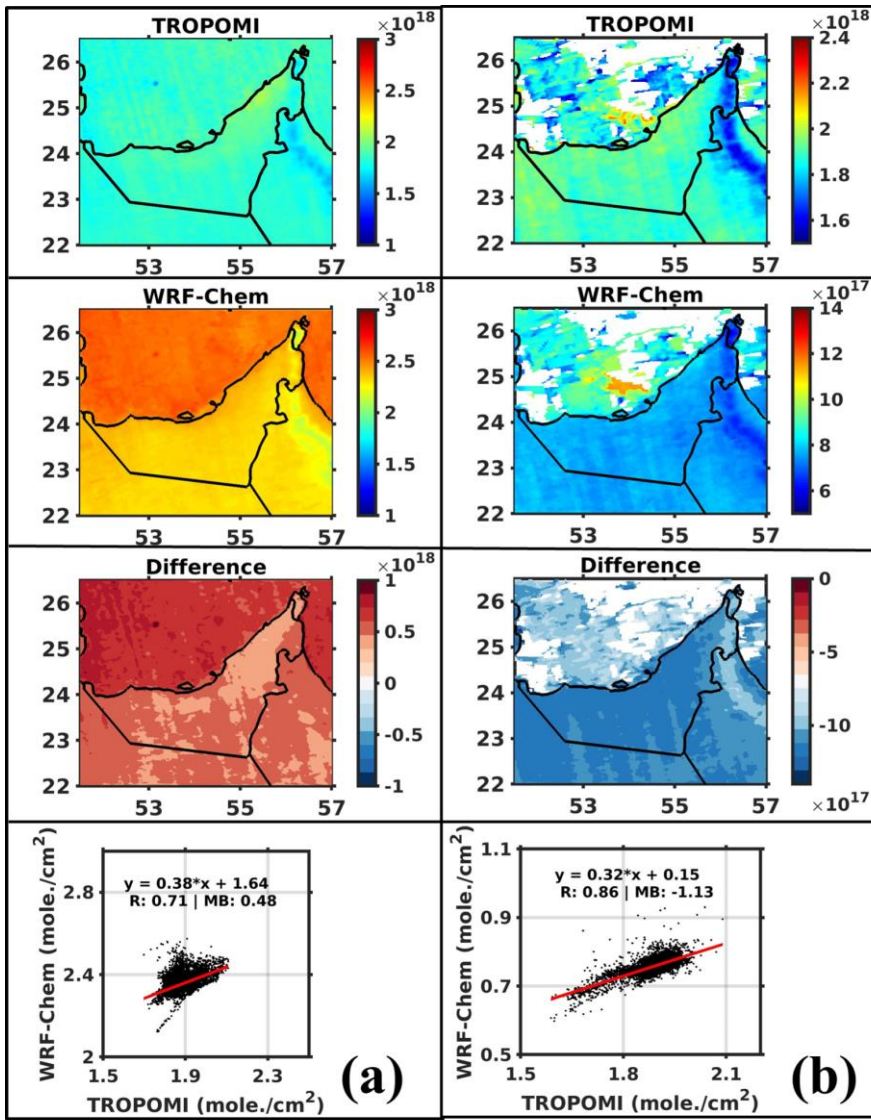


Figure 3: Evaluation of WRF-Chem against satellite-derived CO: Same as Fig. 2 but for the total column of CO.

960

Figure

Formatted: Font: 12 pt, Not Bold



961

962 [Figure 6: Evaluation of WRF-Chem against satellite-derived CO: Same as Fig. 5 but for total](#)
963 [column of CO](#)

964 [We-S6 presents the spatial distribution of tropospheric ozone concentrations over the UAE](#)
965 [as observed by TROPOMI \(TROPOMI-O₃\) and simulated by the WRF-Chem model during](#)

966 [the summer and winter of 2022. In Figures S5 \(a\) and \(b\), TROPOMI shows varying O₃](#)
967 [concentrations with higher values, particularly along the northern coastal regions, where](#)
968 [concentrations reach up to 20 DU. Similarly, WRF-Chem demonstrates a comparable spatial](#)
969 [pattern, with elevated O₃ concentrations in the same regions, reaching up to 40 DU, indicating](#)
970 [that the model captures the general distribution observed by TROPOMI. In Figure S5 \(c\),](#)
971 [representing winter, TROPOMI exhibits a different distribution pattern, with overall lower O₃](#)
972 [concentrations compared to summer. The WRF-Chem simulation in winter also conducted a](#)
973 [shows a broader distribution of O₃, with concentrations reaching up to 25 DU. While the WRF-](#)
974 [Chem model aligns reasonably well with TROPOMI observations, discrepancies in](#)
975 [concentration levels highlight both the model's ability to replicate seasonal variations and areas](#)
976 [where improvements may be needed, especially in the winter months. The comparison of the](#)
977 [WRF-Chem simulated tropospheric ozone levels columns with the TROPOMI-retrieved total](#)
978 [columns \(TROPOMI-O₃\), as is illustrated in Fig. 7. This figure also presents both the absolute](#)
979 [differences \(3rd row\) and scatter plots \(4th row\) between the two datasets for both seasons. The](#)
980 [4, with the statistical comparisons between these datasets are detailed in Table 52. The](#)
981 [TROPOMI-O₃ columns show higher values in summer, at \$7.85 \times 10^{18}\$ molecules/cm² 16.6 DU,](#)
982 [and lower values in winter, at 13.4 DU, which is attributed to increased photochemical activity](#)
983 [during the summer months \(Reddy et al., 2012; Coates et al., \$6.25 \times 10^{18}\$ molecules/cm² 2016;](#)
984 [Badia & Jorba, 2015; Abdallah et al., 2018; Baldasano et al., 2011\) The WRF-Chem](#)
985 [simulations closely match show these variations, with values of \$7.70 \times 10^{18}\$ molecules/cm² 32.8](#)
986 [DU for summer and \$6.06 \times 10^{18}\$ molecules/cm² 24.8 DU for winter, respectively. Therefore,](#)
987 [model output is strongly correlated to the TROPOMI-O₃ columns column concentration, with](#)
988 [a correlation coefficient of \$r=0.8278\$ and 0.93 while 83 and an RMSE \(MAE\) of 1.4 and](#)
989 [1.04\(0. DU \(15.9 and \$0.20 \times 10^{18}\$ molecules/cm² 11.2 DU\) during summer and winter,](#)
990 [respectively. Many studies commonly report higher ozone concentrations in the summer and](#)
991 [lower concentrations in the winter, a phenomenon primarily attributed to increased](#)
992 [photochemical activity during the summer months \(Reddy et al., The WRF-Chem 2012; Coates](#)
993 [et al., 2016; Badia & Jorba 2015; Abdallah et al. 2018; Baldasano et al. 2011\). The WRF-Chem](#)
994 [model systematically underestimates/overestimates ozone levels, with 0. by 15 and \$0.20 \times 10^{18}\$](#)
995 [molecules/cm² both seasons, 9 and 11.2 DU in summer and winter, respectively. The frequency](#)
996 [distribution in Fig. 4\(c\) represents the differences between WRF-Chem and TROPOMI-O₃](#)
997 [concentrations during the summer, showing that they are more pronounced with a positive](#)
998 [skew. This indicates a consistent tendency for the WRF-Chem model to overestimate O₃](#)
999 [concentrations compared to TROPOMI observations in summer. Similarly, Fig. 4\(f\) displays](#)

1000 a frequency distribution for winter with a positive skew and narrower spread, highlighting that
1001 WRF-Chem also tends to overestimate O₃ concentrations compared to TROPOMI during this
1002 season, although with less variability in the overestimations. Therefore, the WRF-Chem model
1003 systematically overestimates O₃ concentrations throughout the year, with a slightly more
1004 consistent bias observed in winter. Hu et al., (2021) highlighted that the substantial influence
1005 of meteorological factors have a considerable effect on ozone production, noting from studies
1006 in China that temperature, relative humidity, and sunshine duration significantly influence
1007 ozone concentrations play significant roles in descending order of importance. They also noted
1008 that strong solar radiation and elevated temperatures could enhance photochemical
1009 reactions, thereby increasing ozone formation. In comparison with ERA-5 data (Fig. S1) and
1010 station data (Table S2), the colder temperatures observed in WRF-Chem, particularly in winter
1011 months when tropospheric column O₃ biases are less positive (Table 2), may explain the
1012 overestimation of O₃ concentrations in the model. Zhang et al., (2020) pointed out found that
1013 low wind speeds and high atmospheric pressure can impede the hinder pollutant dispersion and
1014 dilution of pollutants, which in turn can lead to higher, leading to ozone accumulation, while
1015 Lu et al., (2019) observed that high humidity conditions, with increased can deplete O₃ through
1016 interactions with water vapor, could cause more significant chemical depletion of O₃, as water
1017 vapor interacts with excited ozone molecules to produce and the production of OH radicals.
1018 Hence, the meteorological conditions are conducive to ozone formation in the model but are
1019 insufficient to fully account for WRF-Chem's negative RH2m bias against in situ
1020 measurements in both summer and winter (Tables S2 and S3), combined with temperature
1021 biases, may contribute to the model's significance underprediction of O₃. Sillman, (1999)
1022 demonstrated the ozone formation potential by its precursors being highly nonlinear rather than
1023 linear. Ozone formation can be either NO_x sensitive, meaning O₃ formation increases with an
1024 increase in NO_x concentration, or VOC sensitive, where O₃ formation increases with an
1025 increase in VOC concentration. However, Geng et al., (2007) observed that high NO_x
1026 concentrations in urban environments result in reduced OH radical levels, consequently
1027 decreasing ozone production, as loss of OH is evidenced by the chemical reaction NO₂ + OH
1028 → HNO₃. This observation is consistent with model simulations showing increased NO₂ levels
1029 but markedly lower ozone concentrations at an urban area in the UAE, illustrating the
1030 significant impact of NO_x on urban ozone formation. However, drawing such conclusions
1031 requires careful analysis of model simulations, suggesting that future work, particularly in the
1032 refinement of WRF-Chem evaluations, is essential overprediction of O₃. Further exploration of
1033 these chemical interactions would require additional sensitivity analyses beyond this study's

Formatted: Font color: Auto

Formatted: Font color: Auto

Formatted: Font color: Auto

Formatted: Font color: Auto

Formatted: Font color: Auto

Formatted: Font color: Auto

1034 ~~scope.~~ Future ~~simulations work~~ should ~~not only critically assess these findings but also aim to~~
1035 ~~improve~~ focus on refining model fidelity by ~~enhancing~~ improving the representation of chemical
1036 processes and emissions. ~~Adopting this approach will lead to more precise forecasts and a more~~
1037 ~~profound grip of atmospheric chemistry, thereby enhancing to enhance~~ air quality projections
1038 and ~~fostering a more detailed~~ ~~deepen our~~ understanding of regional pollution patterns ~~over this~~
1039 ~~region.~~

1040 The disparities between WRF-Chem and TROPOMI data highlight the intrinsic challenges
1041 in air quality monitoring and prediction. WRF-Chem's limitations may stem from its
1042 dependency on emissions inventories, ~~meteorological~~ ~~which, as noted above, can have~~
1043 ~~significant discrepancies compared to actual emissions, uncertainty in the meteorological~~
1044 ~~forcing~~ data, and the representation of atmospheric chemistry. TROPOMI, while offering high-
1045 resolution satellite observations, is subject to constraints related to retrieval algorithms and the
1046 influence of atmospheric conditions on measurement accuracy. Liu et al. (2022) identified
1047 that uncertainties in column observations ~~stem~~ arise from the challenges in differentiating
1048 between stratospheric and tropospheric contributions, ~~as well as~~ ~~and~~ uncertainties in the
1049 tropospheric air mass factor and its spectral fitting. ~~The integration of~~ ~~Integrating~~ model
1050 predictions with satellite observations, alongside ground-based measurements, is crucial for
1051 enhancing our understanding of air quality dynamics and improving predictive capabilities.
1052 This synergistic approach can help mitigate biases, enhance accuracy, and provide a more
1053 comprehensive view of atmospheric pollutants' distribution over this region.

1054

Formatted: Font color: Auto, Not Highlight

Formatted: Font color: Auto, Not Highlight

Formatted: Font color: Auto, Not Highlight

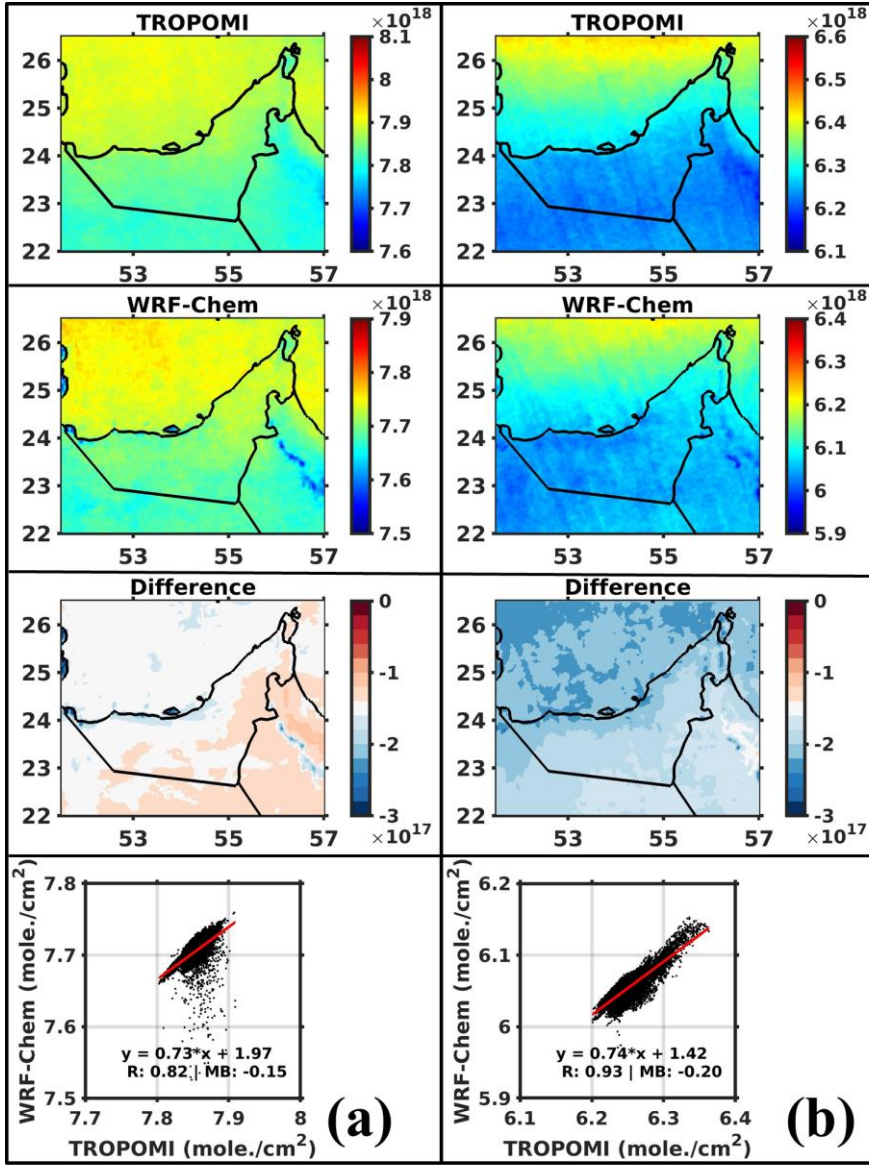
Formatted: Font color: Auto, Not Highlight

Formatted: Font color: Auto, Not Highlight

Formatted: Font color: Auto, Not Highlight

Formatted: Font color: Auto, Not Highlight

Formatted: Font color: Auto, Not Highlight



1055

1056 [Figure 7: Evaluation of WRF-Chem against satellite-derived O₃: Same as Fig. 5 but for total column](#)
 1057 [of ozone.](#)

1058

1059

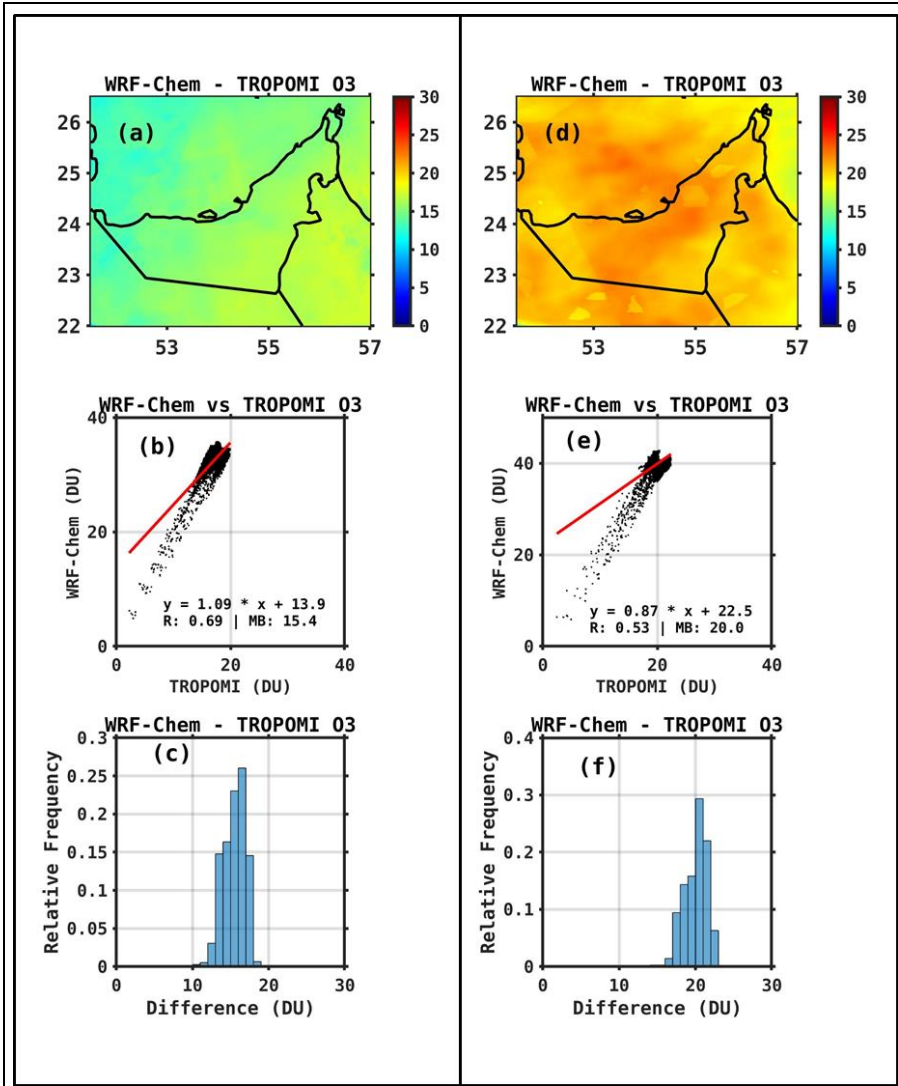


[Figure 4: Evaluation of WRF-Chem against satellite-derived O₃; Same as Fig. 5 but for total column of ozone.](#)

1060

1061 **Table 52: Statistical verification scores for evaluation against TROPOMI measurements:** skill
 1062 scores between TROPOMI columns (mole. /cm²), tropospheric column NO₂ (TROPOMI-NO₂), total
 1063 column carbon monoxide (TROPOMI-CO) ~~and total~~, tropospheric column ozone (TROPOMI-O₃) [and](#)
 1064 [MODIS AOD](#) with corresponding WRF-chem simulated columns during June and December of

1065 2018-2022 over UAE. Means The first two columns show the model and satellite monthly-mean values,
 1066 with the other four giving the MB, MAE and RMSE are given in units of ($\times 10^{15}$ -mole. / cm² for
 1067 TROPOMI-NO₂ and CO and in DU for O₃
 1068

Parameter	Month	MOD	SAT	MB	MAE	R	RMSE
NO ₂ ($\times 10^{16}$ $\times 10^{15}$)	June	0.461.6	0.211.1	0.2550	0.2574	0.9559	0.4016
	Dec	0.431.2	1.0.24	0.1918	0.2054	0.9458	0.4215
O ₃	-	39.6	19.3	20.0	20.0	0.53	1.70
	-	33.1	17.3	15.4	15.4	0.69	1.62
O ₃ CO ($\times 10^{18}$)	-	7.701.9 3	7.851.9 2	-0.1502	0.1503	0.82	0.0103
	-	6.061.9 1	6.251.7 9	-0.212	0.2012	0.9340	0.0104
CO ($\times 10^{18}$)AOD	-	2.350.8 5	1.870.5 4	0.483	0.4832	0.7165	0.0422
	-	0.7628	1.890.2 8	-	1.130.1 1	0.8630	0.0213

Formatted Table

Formatted Table

Formatted: Line spacing: Multiple 1.15 li, No widow/orphan control, Border: Top: (No border), Bottom: (No border), Left: (No border), Right: (No border), Between : (No border)

Formatted: Font: Not Bold

1069

1070 4.3 Model performance with respect to AOD

1071 4.3.1 AERONET

1072 The analysis of daily mean AOD at Mezaira for June 2022 (Fig. 5(a)) and DEWA for
 1073 December 2022 (Fig. 5(b)) reveals the model tends to overestimate the observed AOD values,
 1074 in particular in the summer month when it is the highest (Nelli et al. 2020, 2022). In June at
 1075 Mezaira, the AERONET AOD shows a steady increase from around 0.5 to approximately 1.0
 1076 by the end of the month, which is in line with the expected build-up of aerosols with the annual
 1077 maxima typically occurring in July (Nelli et al., 2022). The WRF-Chem model captures this
 1078 upward variation but consistently overestimates the observed AOD, especially toward the end

1079 [of the month. This overestimation is highlighted by the MB of 0.46. The general overestimation](#)
1080 [of the observed wind speed concerning ground-based measurements \(Tables S2 and S3; Fig.](#)
1081 [S1\) can at least partially explain this bias, together with an incorrect representation of the](#)
1082 [particle size distribution and hence the sedimentation rates, leading to excessive amounts of](#)
1083 [suspended dust \(Ukhov et al., 2021; Parajuli et al., 2023\). The moderate correlation coefficient](#)
1084 [\(\$r = 0.60\$ \) suggests that the model's day-to-day variability reasonably follows that observed.](#)
1085 [This is expected, as dust lifting in the warmer months is mainly associated with the Shamal](#)
1086 [winds \(Yu et al., 2016\), which are fairly well represented in the model. Conversely, at DEWA](#)
1087 [in December \(Fig. 5\(b\)\), the observed AODs are lower, fluctuating between 0.2 and 0.3,](#)
1088 [indicative of the season's lower aerosol concentrations \(Nelli et al., 2020\). The WRF-Chem](#)
1089 [model again follows the observed variation but shows occasional significant overestimations,](#)
1090 [most notably on December 10th, where simulated AOD spikes to 1.6, far exceeding the](#)
1091 [observed AODs. Dust lifting in the colder months is typically associated with the passage of](#)
1092 [mid-latitude weather systems \(Nelli et al., 2022\), which the WRF model does not fully](#)
1093 [reproduce, in particular with respect to its timing \(Temimi et al., 2020b; Taraphdar et al., 2021\).](#)
1094 [This discrepancy is reflected in the weak correlation coefficient \(\$r = 0.16\$ \) and the MB of 0.05.](#)
1095 [The overestimation of the near-surface wind speed at the location of the airport stations \(Table](#)
1096 [S2\) and the WISE-UAE site \(Table S3\) is also in line with the higher amounts of atmospheric](#)
1097 [dust in the model. Fig. 5 shows that, while the WRF-Chem model demonstrates the ability to](#)
1098 [capture seasonal variations in AOD, it tends to overestimate AOD levels in both summer and](#)
1099 [winter months, suggesting a need for calibration of the aerosol parameterization scheme in the](#)
1100 [model or the emissions input. This comparison highlights the model's potential and limitations](#)
1101 [in simulating the UAE-specific aerosol conditions, as well as where research is needed to](#)
1102 [optimize the model performance.](#)

1103

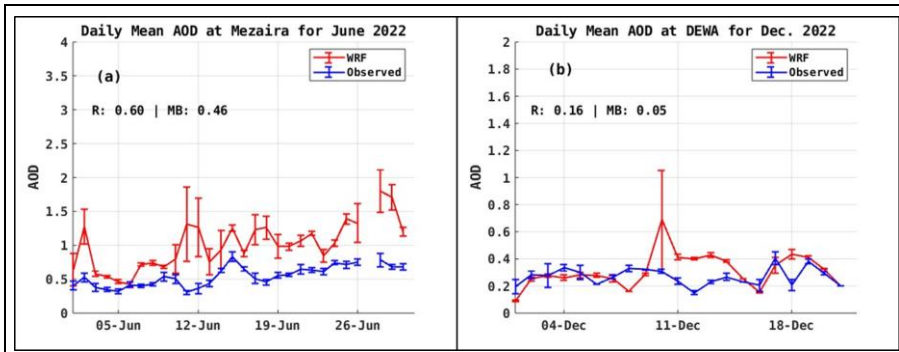


Figure 5: Evaluation of WRF-Chem against AERONET AOD: Daily mean Aerosol Optical Depth (AOD; dimensionless) from WRF-Chem simulations (red) and AERONET observations (blue) at Mezaira during June 2022 (a) and Dewa during December 2022 (b). The lines give the daily mean values and the error bars show one standard deviation from the mean computed using the hourly values. The correlation (r) and mean bias (MB) are given in the plot.

1104

4.3.2 MODIS

1105 The comparison between WRF-Chem simulated and MODIS AOD (MOD-AOD) is
 1106 depicted in Fig. 6, with the statistical comparisons summarized in Table 2. The satellite-derived
 1107 MOD-AOD values follow the same seasonal cycle as the ground-based AERONET
 1108 observations: they are higher in the summer, averaging 0.54, and lower in winter, averaging
 1109 0.28, reflecting the annual cycle in aerosol loading in the region (Nelli et al., 2020). The WRF-
 1110 Chem simulations capture these seasonal variations, with corresponding AODs of 0.85 in
 1111 summer and 0.28 in winter. The model AOD demonstrates moderate correlation with MODIS
 1112 AOD, yielding correlation coefficients of 0.65 for summer and 0.30 for winter, similar to the
 1113 ones with respect to the AERONET AOD, indicating the satellite-derived and ground-based
 1114 AOD estimates are in close agreement, which has been noted by Nelli et al. (2020). The WRF-
 1115 Chem model systematically overestimates AOD by 0.31 in summer, a similar (albeit of a
 1116 smaller magnitude) bias with that respect to the AERONET station (Fig. 5(a)), while slightly
 1117 underestimating by 0.004 in winter.
 1118
 1119

1120 For June, WRF-Chem generally overestimates AOD compared to the MODIS' estimates, in
1121 particular over the southern and central UAE, as shown in the spatial distribution of the
1122 difference between them (Figs. 6(a)-(c)). The frequency distribution shows most differences
1123 clustering around zero, with a slight positive skew, reinforcing the model's overestimation
1124 tendency for this month. Stronger wind speeds and an incorrect representation of the dust
1125 physical and optical properties can explain the model bias. In contrast, in December there are
1126 more balanced results, with WRF-Chem showing a closer alignment with MODIS AOD on
1127 average. The spatial distribution of the model bias displays areas in the central and southern
1128 UAE where the MODIS AOD exceeds the WRF-Chem values, with anomalies of the opposite
1129 sign over the Arabian Gulf and parts of the Al Hajar mountains in Oman. Mostamandi et al.
1130 (2023) showed that, over the Arabian Gulf and in the WRF-Chem model, the dust deposition
1131 rates decrease away from the coastlines, with coastal UAE having lower deposition rates than
1132 inland sites. Excessive dust deposition over the Rub Al Khali Desert is consistent with a clearer
1133 atmosphere closer to the coastlines in the model when compared to the MODIS measurements.
1134 The positive bias over the Arabian Gulf can be attributed to higher amounts of dust transported
1135 upstream by north-westerly winds and/or reduced dust deposition over the water in WRF-
1136 Chem. The frequency distribution in December shows a balanced spread around zero,
1137 suggesting a more accurate seasonal fit than in June. These findings, together with those in Fig.
1138 5 with respect to the AERONET station observations, underscore the influence of seasonal
1139 atmospheric conditions on WRF-Chem's performance and suggest the need for seasonal
1140 adjustments in the aerosol parameterization to improve model accuracy in capturing the UAE's
1141 unique aerosol dynamics.
1142

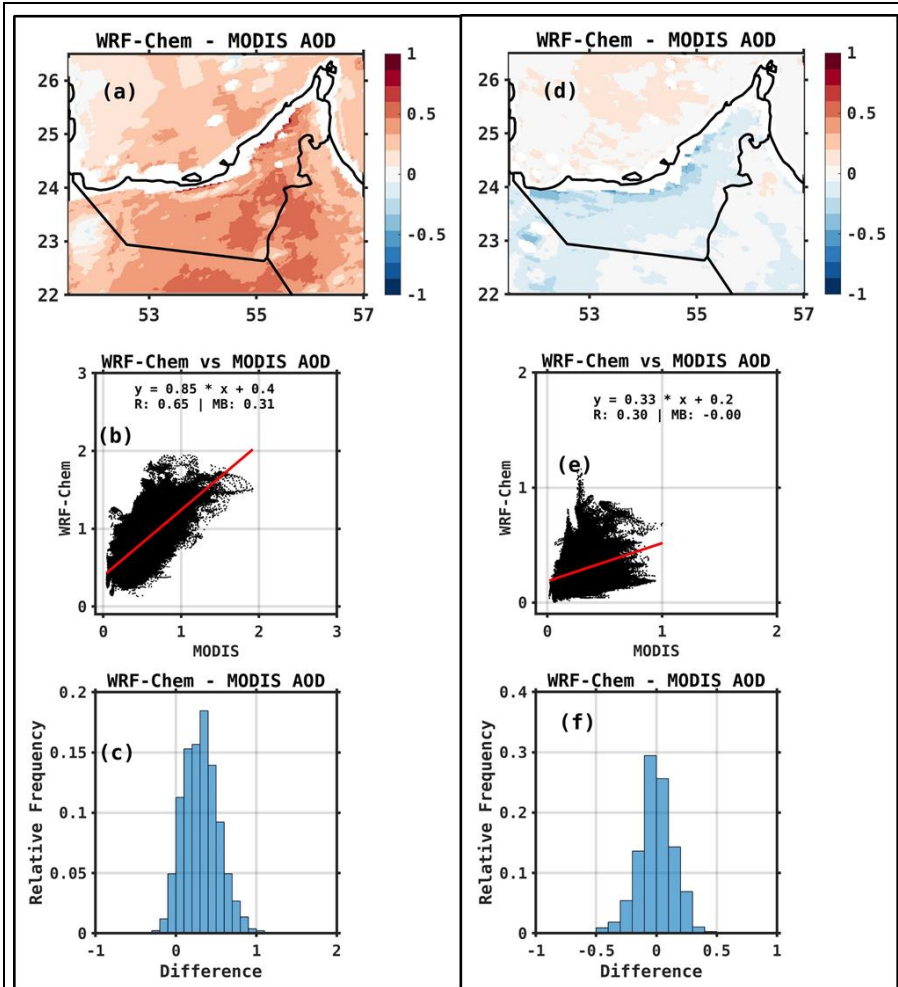


Figure 6: Evaluation of WRF-Chem against MODIS AOD : Same as Fig. 2 but for the MODIS AOD.

1143

1144 4.4. Aerosol influence on Ozone

1145 Tropospheric or surface ozone (O₃) is one of the most significant greenhouse gases after
 1146 carbon dioxide (CO₂) and methane (CH₄) (Ehhalt and Prather, 2001). It plays a critical role in
 1147 the Earth's radiation budget, contributing to an increase in radiative forcing of up to 0.47 W/m²

1148 [and accounting for 3-7% of global warming \(Gauss, 2003; Ehhalt and Prather, 2001\). Elevated](#)
1149 [O₃ levels in the atmospheric boundary layer are toxic and can significantly impact human health](#)
1150 [and vegetation \(Adams et al., 1989\). The interactions between reactive gaseous pollutants and](#)
1151 [aerosols are a major focus in the development of air quality and climate models. Aerosols,](#)
1152 [through scattering and absorption of solar radiation, influence photolysis rates and can either](#)
1153 [increase or decrease the formation of O₃ and its precursors \(He and Carmichael, 1999\). Studies](#)
1154 [have shown that aerosols impact ozone production and loss by altering photolysis frequencies](#)
1155 [\(Dickerson et al., 1997; Jacobson, 1998\). For example, Li et al. \(2011\) used an air quality model](#)
1156 [to evaluate the changes in photolysis frequencies caused by sulfate, nitrate, ammonium, and](#)
1157 [mineral dust aerosols in central and eastern China, finding a 5.4% decrease in daily average](#)
1158 [surface ozone concentrations. Similarly, Lou et al. \(2014\) found that aerosols reduced annual](#)
1159 [mean photolysis frequencies, j\(O¹D\) and j\(NO₂\), by 6–18% in polluted eastern China, resulting](#)
1160 [in reductions of up to 0.5 ppbv in O₃ during spring and summer, using a global chemical](#)
1161 [transport model. Attributing ozone levels to a specific source region is particularly challenging,](#)
1162 [as ozone concentrations are influenced by various processes, including stratosphere-](#)
1163 [troposphere exchange, significant hemispheric background levels, dominant local emissions,](#)
1164 [and complex photochemical reactions involving multiple trace gases \(Fiore et al., 2003\).](#)
1165 [Therefore, it is crucial to understand the impact of aerosol feedback on surface ozone in the](#)
1166 [UAE, a region with high aerosol loading in the Arabian Peninsula.](#)

1167 [From Fig. 4 and the discussion in section 4.2, it is evident that ozone levels are higher during](#)
1168 [the summer season, which coincides with a dominance of aerosols over the UAE. In order to](#)
1169 [better understand the impact of aerosols on ozone concentrations, we conducted a simulation](#)
1170 [in which all aerosol components in the WRF-Chem model are turned off \(No aerosol + radiative](#)
1171 [feedback on\), simulating an aerosol-free atmosphere over the UAE. This simulation is](#)
1172 [conducted alongside a control simulation \(All aerosol + radiative feedback on\) in which all](#)
1173 [aerosol processes are included, both for June 2022. The results of these simulations, comparing](#)
1174 [the scenarios with and without aerosols, are presented in Fig. 7 and highlight the influence of](#)
1175 [aerosols on ozone formation and spatial distribution in the region. This analysis focuses on](#)
1176 [daytime hours \(04-12 UTC\) and non-daytime hours \(13-03 UTC\) to delve deeper into ozone](#)
1177 [dynamics, as ozone production predominantly occurs during the daytime compared to non-](#)
1178 [daytime hours. Figs. 7 \(a\)-\(b\) shows the ozone distribution with and without aerosols during](#)
1179 [the daytime hours \(04-12 UTC; 08-16 LT\). Both panels depict higher ozone concentrations over](#)
1180 [the northern regions, with a clear gradient decreasing towards the south-eastern areas during](#)

1181 [daytime hours. The influence of aerosols on ozone production is evident in areas where the](#)
1182 [ozone levels are slightly elevated, suggesting that aerosols contribute to ozone production/loss](#)
1183 [under daytime conditions based on the nature of the aerosols. Fig. 7 \(c\) highlights the difference](#)
1184 [in ozone concentrations between simulations with and without aerosols for daytime hours. The](#)
1185 [difference shows localized areas of positive and negative changes, indicating regions where](#)
1186 [aerosols either enhance or suppress ozone levels. Notably, over the northern areas, particularly](#)
1187 [in oceanic regions where the ozone concentrations are the highest, the differences are generally](#)
1188 [positive, reflecting a positive feedback of aerosols on ozone production, particularly over the](#)
1189 [Arabian Gulf. On the other hand, over land areas, where the ozone is lower, the lower](#)
1190 [photolysis rates may limit ozone production. Therefore, the impact of aerosols on ozone varies](#)
1191 [based on their origin, such as dust events. These aerosols can have anthropogenic, natural, or](#)
1192 [marine origins \(Filioglou et al., 2020; Nelli et al., 2021\). Aerosols significantly influence](#)
1193 [surface ozone through atmospheric chemical and physical processes. Depending on their](#)
1194 [nature, aerosols can either increase or decrease ozone levels, as observed in various studies](#)
1195 [\(Gao et al., 2023; Shi et al., 2022\). As noted in studies such as Wang et al. \(2019\), Mukherjee](#)
1196 [et al. \(2020\), and Qu et al. \(2021\), the reduction in the incoming shortwave radiation flux will](#)
1197 [hinder the generation of ozone, as well as an increase in the NO/NO₂ ratio, which can happen](#)
1198 [when the pollutants' concentration increases in a shallower boundary layer. On the other hand,](#)
1199 [higher amounts of CO and NO₂ will promote the production of ozone.](#)

1200 [Fig. 7 \(d\) and \(e\) illustrate ozone concentrations with and without aerosols for the remaining](#)
1201 [hours \(non-daytime\). The patterns are largely similar to those observed during the daytime,](#)
1202 [except over urban areas where the ozone concentration is much reduced owing to the lack of](#)
1203 [in situ generation due to the absence of sunlight and underestimation of ozone precursor](#)
1204 [concentration. Fig. 7\(d\) shows slightly higher concentrations than Fig. 7\(e\), suggesting that](#)
1205 [aerosols continue to have an impact on ozone production, albeit less pronounced, during non-](#)
1206 [daytime periods. Fig. 7\(f\) presents the difference in ozone concentrations between simulations](#)
1207 [with and without aerosols for the non-daytime hours. The spatial distribution of positive and](#)
1208 [negative differences follows a similar pattern to that observed during the daytime hours, though](#)
1209 [the magnitudes are generally larger. This suggests that ozone advection from upstream sources](#)
1210 [may play a role. Additionally, marine aerosols can contribute to ozone production through their](#)
1211 [nature.](#)

1212

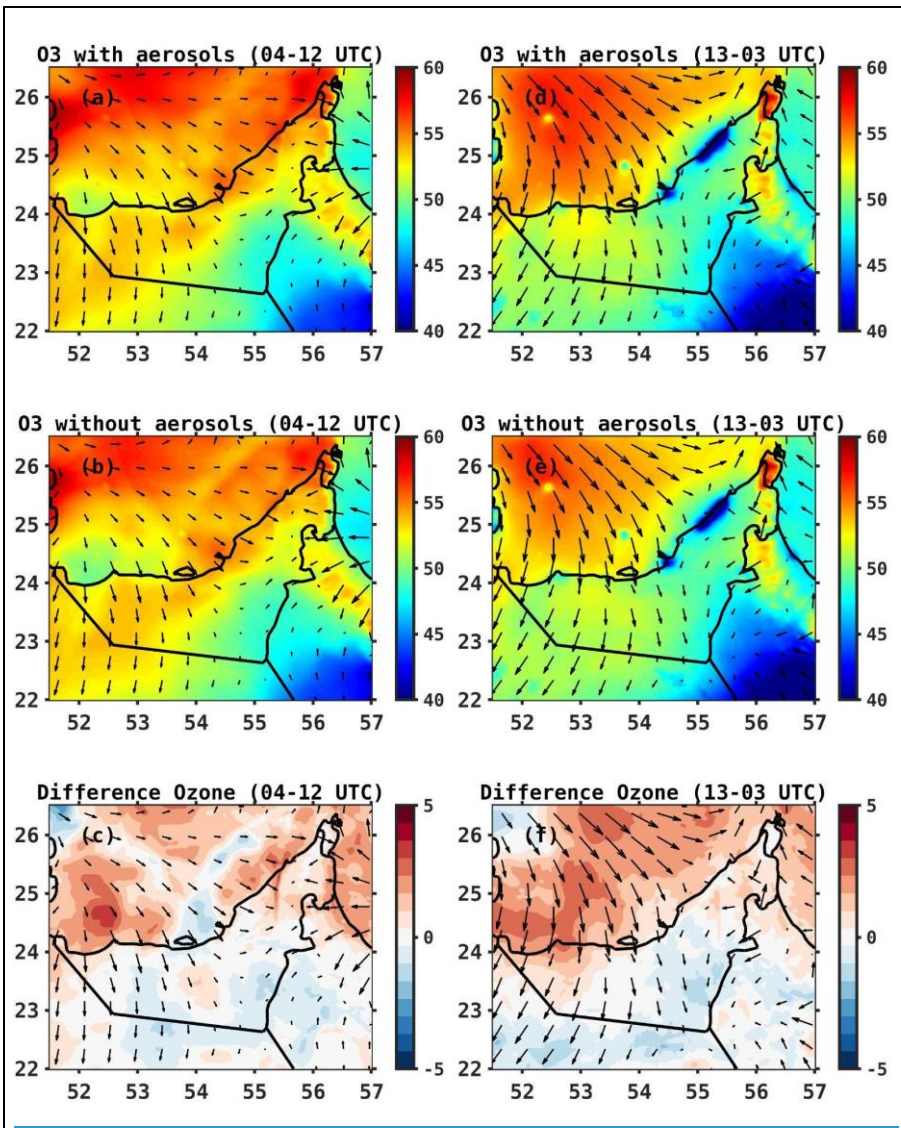


Figure 7: Ozone (O_3) Sensitivity Simulations: Spatial distribution of surface ozone concentrations (ppb) simulated by the WRF-Chem model with (a) and without (b) aerosols over the UAE for specified daytime hours during June 2022. (d)-(e) are as (a)-(b) for the remaining hours. Panels (c) and (f) illustrate the difference (%) in ozone concentrations (with aerosols minus without aerosols) during daytime hours and the remaining hours.

respectively. The 10-m wind vectors (m/s) are overlaid on each plot, indicating the wind patterns influencing the ozone distribution.

5. Conclusions

This study rigorously evaluates the performance of the Weather Research and Forecasting model coupled with chemistry (WRF-Chem). ~~The model ability to simulate~~ in simulating meteorological parameters and ~~gaseousair~~ pollutants over the United Arab Emirates (UAE) ~~is assessed~~ during June and December ~~2018 to reflect~~2022, representing contrasting summer and winter conditions. The ~~model~~model's performance is assessed through ~~comparison~~comparisons with ground-based observations and ERA-5 reanalysis data for meteorological parameters, ~~and as well as~~ AERONET, TROPOMI, and MODIS satellite observations for ~~gaseousair~~ pollutants.

We evaluated WRF-Chem model's accuracy in simulating meteorological parameters, in ~~particular~~particularly 2-meter temperature (T2m), 10-meter wind speed (WS10m), and ~~solar radiation (SR)~~2-meter relative humidity (RH2m) across ~~167~~ locations in the UAE. The model generally ~~underestimates-overestimates~~ T2m in summer by less than 0.52 °C and ~~overestimates~~ ~~underestimates~~ it in winter by ~~less than~~ 1.3 °C, with correlation coefficients ranging from 0.7 to 0.985 among the stations. ~~WRF-chem~~This is comparable performance ~~for WS10m and SR~~ has shown high scores, indicating ~~enhanced accuracy across~~with compared to that reported studies (e.g., Branch et al., 2021; Temimi et al., 2020b), reflecting the ~~locations~~. Regionally, it ~~slightly underpredicts~~T2m added value of explicitly predicting chemistry fields in summer (by 0.37 °C for land and 0.48 °C for marine) mainly due to colder nights, and overestimates in winter (by 0.76 °C for land and 1.30 °C for marine), both with strong correlations above 0.83. ~~Higher SR values in summer and winter, suggest reduced cloud cover and this aerosol loading in WRF-Chem-rich region. An incorrect representation of surface properties, such as the albedo and surface emissivity, and deficiencies in the model physics and dynamics, may explain the referred temperature biases.~~ For WS10m, the model's bias is within ± 1 m/s, and ~~correlation coefficients range between 0.78 and 0.89~~0.5 m/s, indicating good agreement for both land and marine areas. ~~The tendency for the model to overestimate the observed wind speed may arise from deficiencies in the surface drag parameterization scheme and an underrepresentation of its subgrid-scale variability (Nelli et al., 2020). In any case, and as for~~

Formatted: Font: Calibri, 11 pt

Formatted: Space After: 8 pt, Line spacing: Multiple 1.08 li

Formatted: Font color: Auto

Formatted: Font color: Auto

Formatted: Font color: Auto

Formatted: Font color: Auto

Formatted: Font color: Auto

Formatted: Font color: Auto

Formatted: Font color: Auto

Formatted: Font color: Auto

Formatted: Font color: Auto

Formatted: Font color: Auto

Formatted: Font color: Auto

Formatted: Font color: Auto

1243 [air temperature, the magnitude of the biases is much smaller than that reported in other studies,](#)
1244 [for which the wind speed biases exceed 3 m/s \(Branch et al., 2021; Fonseca et al., 2020; Temimi](#)
1245 [et al., 2020b\). The dry bias noted in these studies, however, is also seen in the WRF-Chem](#)
1246 [simulations, possibly arising from a drier soil, an incorrect representation of the mesoscale](#)
1247 [\(sea-/land-breeze\) circulations, and a dry bias in the forcing data. The WRF-Chem model](#)
1248 [evaluation against WISE-UAE measurements reveals a comparable performance to that seen](#)
1249 [with respect to the airport stations w.r.t T2m, WS10m and RH2m. An evaluation against the](#)
1250 [WRF-Chem values reveals the model overestimates the incoming shortwave radiation flux](#)
1251 [\(SW\) by about 30 W/m² for December, which can be attributed to reduced cloud cover, a](#)
1252 [known WRF deficiency \(Wehbe et al., 2019; Fonseca et al. 2020, 2022a\). An inspection of the](#)
1253 [diurnal cycle revealed the cold \(typically by 2-3 °C\) and dry \(by about 20%\) biases occur](#)
1254 [mostly at night, when the wind speed in the model is higher than that observed, suggesting](#)
1255 [increased advection of cooler and drier desert air into the site.](#)

1256 The comparison of ERA5 reanalysis data with WRF-Chem simulations revealed regional
1257 variations in T2m, specifically underestimation in the UAE's [southsouthern region](#) and
1258 overestimation in the north-west. ~~The most significant differences were observed over the~~
1259 ~~Arabian Gulf region, especially during warmer months. These temperature discrepancies are~~
1260 ~~crucial for the land-sea breeze circulation, with higher Gulf temperatures potentially weakening~~
1261 ~~this pattern. This could lead to diminished transport of cleaner marine air inland, thereby~~
1262 ~~hindering pollutant dispersion over land and adversely affecting air quality and pollutant~~
1263 ~~distribution. —western region.~~ Statistical metrics for summer ~~shows~~[show](#) an
1264 ~~overestimation~~[underestimation](#) of ~~0.081~~ °C and a correlation coefficient (r) of 0.97, ~~while~~
1265 ~~winter's follows.~~ In comparison, for winter a similar pattern [is seen](#) with an
1266 ~~overestimation~~[underestimation](#) of ~~0.531~~ °C and [a r value](#) of ~~0.9892~~ over ~~land mass region of~~
1267 ~~UAE~~[the domain](#). The fact that WRF-Chem performs well against in-situ data and ERA5
1268 reanalysis with respect to air temperature is [also](#) an indication [that](#) the reanalysis dataset
1269 performs well in this region, ~~as noted by Fonseca et al. (2022b) and Nelli et al. (2024a).~~ The
1270 mean PBL from ERA5 is largely consistent with that from the WRF-Chem outputs, with both
1271 data sets displaying a clear seasonal variation—increased PBL during summer and decreased
1272 in winter, correlating with temperature changes. ~~June's modelled PBL has a correlation of 0.91,~~
1273 ~~and December's correlation of 0.98 with ERA5.~~

1274 Regarding gaseous pollutants, both WRF-Chem and satellite data show higher TROPOMI-
1275 NO₂ columns greater than ~~1.2x10¹⁵~~5x10¹⁵ molecules/cm² in urban and industrial regions such
1276 as Dubai, Abu Dhabi, and Ras Al Khaimah ~~emirate, and,~~ reflecting emissions from economic
1277 activities like power generation, water desalination, and industries. Lower concentrations ~~of~~
1278 ~~less than (<1.5x10¹⁵ molecules/cm²)~~ are noted in less urbanized areas. The WRF-Chem model
1279 closely reproduces the TROPOMI-NO₂ spatial patterns. ~~However, even though~~ it
1280 ~~overestimates NO₂~~tends to underestimate the observed concentrations in the Abu Dhabi region
1281 and ~~underestimates it in~~underestimate the north-eastern UAE. ~~High, which has been tied to~~
1282 ~~deficiencies in the emission inventory.~~ Moderate correlation coefficients (0.~~95~~59 in summer
1283 and 0.~~94~~58 in winter) confirm the model's effectiveness in capturing NO₂'s day-to-day
1284 variability. ~~The model shows minimal MB and high r values, indicating small discrepancies in~~
1285 ~~NO₂ estimations. Moreover, the~~ WRF-Chem ~~underestimates~~overestimates the observed
1286 TROPOMI-O₃ ~~columns~~column, as indicated by ~~negative~~positive MB values of around 11-16
1287 DU, yet maintains high correlation coefficients (0.~~82~~78 in summer and 0.~~93~~83 in winter),
1288 suggesting accurate ozone concentration simulations. Colder and drier conditions, along with
1289 deficiencies in the representation of the observed chemistry, particularly concerning the NO_x
1290 emissions linked to the O₃ concentration, can explain the WRF-Chem biases. TROPOMI-CO
1291 column simulations, ~~however~~on the other hand, exhibit significant discrepancies in winter and
1292 lower correlation coefficients (~~0.71 in summer and 0.86 in winter~~), highlighting challenges in
1293 accurately modelling CO levels. ~~This~~Besides an incorrect emission inventory, discrepancies
1294 in the representation of the atmospheric flow and its effect on the pollutant's dispersion, can
1295 explain the model performance. In summer, the analysis conducted here stresses the WRF-
1296 Chem model's strengths in simulating CO, NO₂ and O₃ columns with high fidelity ~~to~~
1297 ~~TROPOMI~~with respect to the TROPOMI's observations, but also points out its limitations in
1298 estimating CO columns accurately in winter.

1299 Regarding aerosol optical depth (AOD) observed by AERONET stations and the MODIS
1300 satellite, the WRF-Chem model generally tends to overestimate AOD, particularly during the
1301 summer months. At Mezaira in June, AERONET data showed a steady increase in AOD, which
1302 the WRF-Chem model captured but consistently overpredicted due to factors such as
1303 overestimated wind speeds and inaccuracies in particle size distribution. In December at
1304 DEWA, observed AOD levels were lower, and while the model followed the observed trends,
1305 it occasionally produced large spikes, reflecting challenges in accurately capturing the effects
1306 of mid-latitude weather systems. Correlation coefficients for AOD comparisons reveal

1307 moderate (0.60) to weak model performance depending on the season, influenced by dust
1308 transport mechanisms. Comparisons with MODIS satellite-derived AOD similarly indicated
1309 seasonal overestimations during the summer, with a closer alignment observed in winter.
1310 Spatially, overestimations in southern and central UAE in June were linked to strong winds
1311 and dust properties, while December results were more balanced. Biases over the Arabian Gulf
1312 were attributed to dust transport and deposition dynamics. Overall, the findings indicate that
1313 while the WRF-Chem model captures seasonal AOD variations, adjustments to aerosol
1314 parameterization and dust representation are necessary to improve model accuracy.

1315 This study also explores the impact of aerosols on surface ozone (O₃) in the UAE by altering
1316 photolysis rates through the scattering and absorption of solar radiation. Using WRF-Chem
1317 model simulations for June 2022, we compared scenarios with and without aerosols to assess
1318 their influence. The results show higher ozone concentrations during daytime in northern
1319 regions, with aerosols contributing to localized increases or decreases. Marine aerosols notably
1320 enhance O₃ production over the Arabian Gulf, while lower photolysis rates limit ozone
1321 formation over land areas. During non-daytime hours, aerosol influence continues but is less
1322 significant, with urban areas experiencing reduced ozone levels due to limited photochemical
1323 activity. Additional sensitivity simulations and in-situ observations are needed to validate these
1324 findings further.

1325 The WRF-Chem model exhibits ~~satisfactory~~enhanced capability in simulating key
1326 meteorological parameters and ~~gaseous~~satisfactory performance in air pollutants over the
1327 UAE, showcasing significant improvements in regional-scale dynamics. This is evidenced by
1328 ~~strong correlation coefficients, variable MB, RMSE and MAE values, and~~high skill scores with
1329 ~~respect to observational data, with~~ a clear ~~enhancement~~improvement over previous research
1330 outcomes, particularly during summer. This comprehensive assessment validates the model's
1331 effectiveness and identifies potential areas for improvement in simulating ~~gaseous~~air pollutant
1332 concentrations across the hyper-arid and aerosol-rich UAE. The discrepancies between model
1333 simulations and various observational data sets ~~may likely~~ arise from improper emission
1334 inventories, particularly anthropogenic emissions, ~~model parameterizations, and~~which must be
1335 optimized based on existing country-specific datasets. Other sources of uncertainty are model
1336 parameterization schemes and the quality of the meteorological ~~inputs~~ and chemistry input data.
1337 Integrating model predictions with satellite observations and ground-based measurements is
1338 crucial for advancing air quality monitoring and enhancing the predictive accuracy of

1339 atmospheric pollutant distributions in the UAE. This collective approach aids in addressing
1340 biases and improving the overall understanding of regional air quality dynamics.

1341

1342 **Code and Data Availability**

1343 The authors would like to thank the United Arab Emirates' National Center of Meteorology for
1344 providing meteorological observations at 16 weather stations for the months of June and
1345 December 2018 under an agreement with clauses for non-disclosure of data. Access to these
1346 data is restricted and readers should request them through contacting
1347 research@ncms.ae. The remaining products considered in this study are
1348 freely available online: (i) ERA-5 reanalysis data is extracted from the Copernicus Climate
1349 Change Service Climate Data Store (Hersbach et al. 2023a,b); (ii) Nitrogen Dioxide (NO₂),
1350 Ozone (O₃) and Carbon Monoxide (CO) column concentrations estimated from the
1351 measurements collected by the Tropospheric Monitoring Instrument (TROPOMI) onboard the
1352 Sentinel 5-P satellite are extracted from the National Aeronautics and Space Administration's
1353 (NASA's) website; (iii) National Centers for Environmental Prediction (NCEP) Final (FNL)
1354 Operational Global Analysis meteorological data used to drive the WRF-chem simulations is
1355 downloaded from the National Center for Atmospheric Research (NCAR) Research Data
1356 Archive website (NCEP/NWS/NOAA/USDC, 2000), with the chemistry data used to force
1357 WRF-Chem, the output of the Community Atmosphere Model with Chemistry (CAM-chem)
1358 model, extracted from NCAR's website (Bucholz et al., 2019); (iv) the WRF-Chem model
1359 used, version 4.3.1, is freely available from the developers' website (WRF, 2023), with the pre-
1360 processor tools available at NCAR's website (NCAR, 2023). All figures displayed in this
1361 manuscript were generated with the Matrix Laboratory (MATLAB) software version 2023
1362 (Mathworks, 2023).

1363 **Acknowledgment**

1364 We are thankful to the development team of the WRF-Chem model for making this model
1365 available as an open-source resource for research. We acknowledge the use of WRF-Chem pre-
1366 processor tools including mozbc, anthro_emiss, and bio_emiss provided by the Atmospheric
1367 Chemistry Observations and Modelling Lab (ACOM) of the National Center for Atmospheric
1368 Research (NCAR). Our also thanks go to the Community Atmosphere Model with Chemistry
1369 (CAM-Chem) for the chemical initial and boundary conditions. In addition, we are also

Formatted: English (U.A.E.)

Formatted: Adjust space between Latin and Asian text,
Adjust space between Asian text and numbers

Formatted: English (U.A.E.)

1370 thankful to the National Centers for Environmental Prediction (NCEP) Final (FNL)
1371 Operational Global Analysis data for supplying meteorological initial and lateral boundary
1372 conditions. Additionally, we are grateful to Sentinel-5P TROPOMI for satellite datasets.
1373 Finally, this research greatly benefited from the high-performance computing and research
1374 computing resources provided by Khalifa University. We express our sincere gratitude for their
1375 invaluable support. [We would also like to thank the two anonymous reviewers for their several](#)
1376 [constructive and insightful comments and suggestions that helped to substantially improve the](#)
1377 [quality of this work.](#)

1378 **Conflict of interest**

1379 The authors declare they do not have any conflict of interest.

1380 **Author contribution**

1381 Conceptualisation and methodology: D.F. and Y.Y.; Data curation and visualization: Y.Y.; formal
1382 analysis and interpretation: Y.Y., R.F., N.N., and D.F.; project administration and supervision: D.F.;
1383 writing—original draft: Y.Y.; review and editing: all authors.

1384 **References**

- 1385 Abdallah, C., Afif, C., El Masri, N., Öztürk, F., Keleş, M., & Sartelet, K. (2018). A first annual assessment
1386 of air quality modeling over Lebanon using WRF/Polyphemus. In *Atmospheric Pollution Research*
1387 (Vol. 9, Issue 4, pp. 643–654). Elsevier B.V.
1388 <https://doi.org/10.1016/j.apr.2018.01.003><https://doi.org/10.1016/j.apr.2018.01.003>
- 1389 Abida, R., Addad, Y., Francis, D., Temimi, M., Nelli, N., Fonseca, R., Nesterov, O., & Bosc, E. (2022).
1390 Evaluation of the Performance of the WRF Model in a Hyper-Arid Environment: A Sensitivity
1391 Study. *Atmosphere*, 13(6).
1392 <https://doi.org/10.3390/atmos13060985><https://doi.org/10.3390/atmos13060985>
- 1393 Abuelgasim, A., & Farahat, A. (2020). Effect of dust loadings, meteorological conditions, and local
1394 emissions on aerosol mixing and loading variability over highly urbanized semiarid countries:
1395 United Arab Emirates case study. *Journal of Atmospheric and Solar-Terrestrial Physics*, 199.
1396 <https://doi.org/10.1016/j.jastp.2020.105215>
- 1397 [Adams, R.M., Glycer, J.D., Johnson, S.L., McCarl, B.a., 1989. A reassessment of the eco nomic effects of](#)
1398 [Ozone on U.S. Agriculture. JAPCA 39 \(7\), 960–968. https://doi.org/](#)
1399 [10.1080/08940630.1989.10466583.](#)
- 1400 Archer-Nicholls, S., Lowe, D., Darbyshire, E., Morgan, W. T., Bela, M. M., Pereira, G., Trembath, J.,
1401 Kaiser, J. W., Longo, K. M., Freitas, S. R., Coe, H., & McFiggans, G. (2015). Characterising Brazilian
1402 biomass burning emissions using WRF-Chem with MOSAIC sectional aerosol. *Geoscientific Model*

Formatted: Adjust space between Latin and Asian text,
Adjust space between Asian text and numbers

Field Code Changed

Formatted: Default Paragraph Font, Font color: Blue

1403 *Development*, 8(3), 549–577. [https://doi.org/10.5194/gmd-8-549-](https://doi.org/10.5194/gmd-8-549-2015)
1404 [2015](https://doi.org/10.5194/gmd-8-549-2015)<https://doi.org/10.5194/gmd-8-549-2015>

1405 Alapaty, K., Herwehe, J. A., Otte, T. L., Nolte, C. G., Bullock, O. R., Mallard, M. S., Kain, J. S., & Dudhia,
1406 J. (2012) Introducing subgrid-scale cloud feedbacks to radiation for regional meteorological and
1407 climate modeling. *Geophysical Research Letters*, 39, L24809.
1408 <https://doi.org/10.1029/2012GL054031>

1409 Badia, A., & Jorba, O. (2015). Gas-phase evaluation of the online NMMB/BSC-CTM model over Europe
1410 for 2010 in the framework of the AQMEII-Phase2 project. *Atmospheric Environment*, 115, 657–
1411 669.
1412 <https://doi.org/10.1016/j.atmosenv.2014.05.055>[https://doi.org/10.1016/j.atmosenv.2014.05.0](https://doi.org/10.1016/j.atmosenv.2014.05.055)
1413 [55](https://doi.org/10.1016/j.atmosenv.2014.05.055)

1414 Baldasano, J. M., Pay, M. T., Jorba, O., Gassó, S., & Jiménez-Guerrero, P. (2011). An annual assessment
1415 of air quality with the CALIOPE modeling system over Spain. *Science of the Total Environment*,
1416 409(11), 2163–2178.
1417 <https://doi.org/10.1016/j.scitotenv.2011.01.041>[https://doi.org/10.1016/j.scitotenv.2011.01.04](https://doi.org/10.1016/j.scitotenv.2011.01.041)
1418 [1](https://doi.org/10.1016/j.scitotenv.2011.01.041)

1419 Basha, G., Kishore, P., Ratnam, M. V., Ravindra Babu, S., Velicogna, I., Jiang, J. H., & Ao, C. O. (2019).
1420 Global climatology of planetary boundary layer top obtained from multi-satellite GPS RO
1421 observations. *Climate Dynamics*, 52(3–4), 2385–2398. [https://doi.org/10.1007/s00382-018-](https://doi.org/10.1007/s00382-018-4269-1)
1422 [4269-1](https://doi.org/10.1007/s00382-018-4269-1)<https://doi.org/10.1007/s00382-018-4269-1>

1423 Boersma, K. F., Eskes, H. J., Richter, A., De Smedt, I., Lorente, A., Beirle, S., Van Geffen, J. H. G. M., Zara,
1424 M., Peters, E., Van Roozendaal, M., Wagner, T., Maasakkers, J. D., Van Der A, R. J., Nightingale,
1425 J., De Rudder, A., Irie, H., Pinardi, G., Lambert, J. C., & Compornolle, S. C. (2018). Improving
1426 algorithms and uncertainty estimates for satellite NO₂ retrievals: Results from the quality
1427 assurance for the essential climate variables (QA4ECV) project. *Atmospheric Measurement*
1428 *Techniques*, 11(12), 6651–6678. [https://doi.org/10.5194/amt-11-6651-](https://doi.org/10.5194/amt-11-6651-2018)
1429 [2018](https://doi.org/10.5194/amt-11-6651-2018)<https://doi.org/10.5194/amt-11-6651-2018>

1430 Borsdorff, T., Aan de Brugh, J., Hu, H., Aben, I., Hasekamp, O., & Landgraf, J. (2018). Measuring Carbon
1431 Monoxide With TROPOMI: First Results and a Comparison With ECMWF-IFS Analysis Data.
1432 *Geophysical Research Letters*, 45(6), 2826–2832.
1433 <https://doi.org/10.1002/2018GL077045><https://doi.org/10.1002/2018GL077045>

1434 Borsdorff, T., Hasekamp, O. P., Wassmann, A., & Landgraf, J. (2014). Insights into Tikhonov
1435 regularization: Application to trace gas column retrieval and the efficient calculation of total
1436 column averaging kernels. *Atmospheric Measurement Techniques*, 7(2), 523–535.
1437 <https://doi.org/10.5194/amt-7-523-2014><https://doi.org/10.5194/amt-7-523-2014>

1438 Branch, O., Schwitalla, T., Temimi, M., Fonseca, R., Nelli, N., Weston, M., Milovac, J., & Wulfmeyer, V.
1439 (2021). Seasonal and diurnal performance of daily forecasts with WRF V3.8.1 over the United
1440 Arab Emirates. *Geoscientific Model Development*, 14(3), 1615–1637.
1441 <https://doi.org/10.5194/gmd-14-1615-2021><https://doi.org/10.5194/gmd-14-1615-2021>

1442 Bucholz, R. R., Emmons, L. K., Tilmes, S., & The CESM2 Development Team (2019) CESM2.1/CAM-chem
1443 Instantaneous Output for Boundary Conditions. UCAR/NCAR – Atmospheric Chemistry
1444 Observations and Modeling Laboratory. Subset used (Lat: -5 to 50; Lon: 15 to 55; June and

Formatted: Default Paragraph Font

Formatted: Underline

Formatted: Adjust space between Latin and Asian text,
Adjust space between Asian text and numbers

Formatted: Default Paragraph Font, Font color: Black

1445 December 2018) [Dataset]. Accessed on 10 July 2023, available online at
 1446 <https://doi.org/10.5065/NMP7-EP60><https://doi.org/10.5065/NMP7-EP60>

1447 Chaouch, N., Temimi, M., Weston, M., & Ghedira, H. (2017) Sensitivity of the meteorological model
 1448 WRF-ARW to planetary boundary layer schemes during fog conditions in a coastal arid region.
 1449 *Atmospheric Research*, 187, 106-127. <https://doi.org/10.1016/j.atmosres.2016.12.009>

1450 Chen, Y., Chen, S., Zhao, D., Li, J., Bi, H., Lou, G., & Guan, Y. (2022). The role of boundary layer height
 1451 in India on transboundary pollutions to the Tibetan Plateau. *Science of the Total Environment*,
 1452 837. <https://doi.org/10.1016/j.scitotenv.2022.155816>

1453 Chin, M., Ginoux, P., Kinne, S., Torres, O., ~~Holben, Holben~~, B. N., Duncan, B. N., Martin, R. V., Logan, J. A.,
 1454 Higurashi, A., & Nakajima, T. (2002). Tropospheric ~~Aerosol-Optical-Thickness~~~~aerosol optical~~
 1455 ~~thickness~~ from the GOCART ~~Model~~~~model~~ and ~~Comparisons~~~~comparisons~~ with ~~Satellite~~~~satellite~~
 1456 and Sun ~~Photometer Measurements~~. Accessed on 10 July 2023, available online at ~~photometer~~
 1457 ~~measurements~~. *Journal of Atmospheric Science*, 59, 461-483.
 1458 <http://weather.engin.umich.edu>[https://doi.org/10.1175/1520-0469\(2002\)059<0461:TAOTFT>2.0.CO;2](https://doi.org/10.1175/1520-0469(2002)059<0461:TAOTFT>2.0.CO;2)

1460 Chudnovsky, A., Lyapustin, A., Wang, Y., Tang, C., Schwartz, J., & Koutrakis, P. (2014). High resolution
 1461 aerosol data from MODIS satellite for urban air quality studies. *Central European Journal of*
 1462 *Geosciences*, 6(1), 17–26. <https://doi.org/10.2478/s13533-012-0145-4>
 1463 <https://doi.org/10.2478/s13533-012-0145-4>

1464 Coates, J., Mar, K. A., Ojha, N., & Butler, T. M. (2016). The influence of temperature on ozone
 1465 production under varying NOx conditions - A modelling study. *Atmospheric Chemistry and*
 1466 *Physics*, 16(18), 11601–11615. [https://doi.org/10.5194/acp-16-11601-](https://doi.org/10.5194/acp-16-11601-2016)
 1467 [2016](https://doi.org/10.5194/acp-16-11601-2016)<https://doi.org/10.5194/acp-16-11601-2016>

1468 Crippa, M., Solazzo, E., Huang, G., Guizzardi, D., Koffi, E., Muntean, M., Schieberle, C., Friedrich, R., &
 1469 Janssens-Maenhout, G. (2020). High resolution temporal profiles in the Emissions Database for
 1470 Global Atmospheric Research. *Scientific Data*, 7(1). [https://doi.org/10.1038/s41597-020-0462-](https://doi.org/10.1038/s41597-020-0462-2)
 1471 [2](https://doi.org/10.1038/s41597-020-0462-2)<https://doi.org/10.1038/s41597-020-0462-2>

1472 Dai, A. (2024) [The diurnal cycle from observations and ERA5 in precipitation, clouds, boundary layer](https://doi.org/10.1007/s00382-024-07182-6)
 1473 [height, buoyancy, and surface fluxes. *Climate Dynamics*, 62, 5879-5908.](https://doi.org/10.1007/s00382-024-07182-6)
 1474 <https://doi.org/10.1007/s00382-024-07182-6>

1475 Dee, D. P., Uppala, S. M., Simmons, A. J., Berrisford, P., Poli, P., Kobayashi, S., Andrae, U., Balmaseda,
 1476 M. A., Balsamo, G., Bauer, P., Bechtold, P., Beljaars, A. C. M., van de Berg, L., Bidlot, J., Bormann,
 1477 N., Delsol, C., Dragani, R., Fuentes, M., Geer, A. J., ... Vitart, F. (2011). The ERA-Interim reanalysis:
 1478 Configuration and performance of the data assimilation system. *Quarterly Journal of the Royal*
 1479 *Meteorological Society*, 137(656), 553–597. <https://doi.org/10.1002/qj.828>

1480 [Dickerson, R.R., Kondragunta, S., Stenchikov, G., Civerolo, K.L., Doddridge, B.G., Holben, B.N., \(1997\).](https://doi.org/10.1126/science.1172133)
 1481 [The impact of aerosols on solar ultraviolet radiation and photochemical smog. *Science* 215, 827–](https://doi.org/10.1126/science.1172133)
 1482 [830. <https://doi.org/10.1126/science.1172133>.](https://doi.org/10.1126/science.1172133)

1483 Dekker, Iris N., Sander Houweling, Sudhanshu Pandey, Maarten Krol, Thomas Röckmann, Tobias
 1484 Borsdorff, Jochen Landgraf, and Ilse Aben. 2019. "What Caused the Extreme CO Concentrations
 1485 during the 2017 High-Pollution Episode in India?" *Atmospheric Chemistry and Physics* 19 (6):
 1486 3433–45. <https://doi.org/10.5194/acp-19-3433-2019>.

Formatted: Default Paragraph Font

Formatted: Adjust space between Latin and Asian text, Adjust space between Asian text and numbers

Formatted: Default Paragraph Font, Font color: Blue

Field Code Changed

Formatted: Font: Not Italic

Formatted: Font: Not Italic

Formatted: Font: Not Italic

Formatted: Font: Not Italic

Formatted: Font: Not Italic

Formatted: Adjust space between Latin and Asian text, Adjust space between Asian text and numbers

Formatted: No underline

Field Code Changed

Formatted: Default Paragraph Font, Font color: Blue

1487 [Devadiga, S. \(2024\) MOD04_L2 - MODIS/Terra Aerosol 5-Min L2 Swath 10 km. Accessed on 30 October](https://doi.org/10.5067/MODIS/MOD04_L2.061)
1488 [2024, available online at https://doi.org/10.5067/MODIS/MOD04_L2.061](https://doi.org/10.5067/MODIS/MOD04_L2.061)

1489 [Dubovik, O., Smirnov, A., Holben, B. N., King, M. D., Kaufman, Y. J., Eck, T. F., and Slutsker, I.: Accuracy](https://doi.org/10.1029/2000jd900040)
1490 [assessments of aerosol optical properties retrieved from Aerosol Robotic Network \(AERONET\)](https://doi.org/10.1029/2000jd900040)
1491 [Sun and sky radiance measurements, *J. Geophys. Res.-Atmos.*, *105*, 9791–9806,](https://doi.org/10.1029/2000jd900040)
1492 [https://doi.org/10.1029/2000jd900040, 2000.](https://doi.org/10.1029/2000jd900040)

1493 [Ehhalt, D., Prather, M., 2001. Atmospheric chemistry and greenhouse gases. *Clim. Chang. Sci. Basis*](https://doi.org/10.2753/JES1097-203X330403)
1494 [239–287. https://doi.org/10.2753/JES1097-203X330403.](https://doi.org/10.2753/JES1097-203X330403)

~~1495 German Aerospace Center (DLR), Copernicus Sentinel data processed by ESA (2020) Sentinel 5P~~
~~1496 TROPOMI Total Ozone Column 1 Orbit L2 5.5 km x 3.5 km. Greenbelt, MD, USA, Goddard Earth~~
~~1497 Sciences Data and Information Services Center (GES DISC) [Dataset]. Accessed on 10 October~~
~~1498 2023, available online at https://doi.org/10.5270/S5P_ft13p57~~

1499 [Eltahan, M., Shokr, M., & Sherif, A. O. \(2018\). Simulation of severe dust events over Egypt using tuned](https://doi.org/10.3390/atmos9070246)
1500 [dust schemes in Weather Research Forecast \(WRF-Chem\). *Atmosphere*, *9*\(7\).](https://doi.org/10.3390/atmos9070246)
1501 [https://doi.org/10.3390/atmos9070246https://doi.org/10.3390/atmos9070246](https://doi.org/10.3390/atmos9070246)

1502 [Emmons, L. K., Schwantes, R. H., Orlando, J. J., Tyndall, G., Kinnison, D., Lamarque, J. F., Marsh, D.,](https://doi.org/10.1029/2019MS001882)
1503 [Mills, M. J., Tilmes, S., Bardeen, C., Buchholz, R. R., Conley, A., Gettelman, A., Garcia, R., Simpson,](https://doi.org/10.1029/2019MS001882)
1504 [I., Blake, D. R., Meinardi, S., & Pétron, G. \(2020\). The Chemistry Mechanism in the Community](https://doi.org/10.1029/2019MS001882)
1505 [Earth System Model Version 2 \(CESM2\). *Journal of Advances in Modeling Earth Systems*, *12*\(4\).](https://doi.org/10.1029/2019MS001882)
1506 [https://doi.org/10.1029/2019MS001882https://doi.org/10.1029/2019MS001882](https://doi.org/10.1029/2019MS001882)

1507 [Emmons, L. K., Walters, S., Hess, P. G., Lamarque, J., Pfister, G. G., Fillmore, D., Granier, C., & Emmons,](https://doi.org/10.5194/gmd-3-43-2010)
1508 [L. K., Walters, S., Hess, P. G., Lamarque, J.-F., Pfister, G. G., Fillmore, D., Granier, C., Guenther, A.,](https://doi.org/10.5194/gmd-3-43-2010)
1509 [Kinnison, D., Laepple, T., Orlando, J., Tie, X., Tyndall, G., Wiedinmyer, C., Baughcum, S. L., and](https://doi.org/10.5194/gmd-3-43-2010)
1510 [Kloster, S. \(2010\). Description and evaluation of the Model for Ozone and Related chemical](https://doi.org/10.5194/gmd-3-43-2010)
1511 [Tracers, version 4 \(MOZART-4\). *Geoscientific Model Development*, *3*\(1\), 43–67.](https://doi.org/10.5194/gmd-3-43-2010)
1512 <https://doi.org/10.5194/gmd-3-43-2010>

1513 [Filioglou, M., Giannakaki, E., Backman, J., Kesti, J., Hirsikko, A., Engelmann, R., O'Connor, E.,](https://doi.org/10.5194/acp-20-8909-2020)
1514 [Leskinen, J. T. T., Shang, X., Korhonen, H., Lihavainen, H., Romakkaniemi, S., & Komppula, M.](https://doi.org/10.5194/acp-20-8909-2020)
1515 [\(2020\). Optical and geometrical aerosol particle properties over the United Arab Emirates.](https://doi.org/10.5194/acp-20-8909-2020)
1516 [*Atmospheric Chemistry and Physics*, *20*\(14\), 8909–8922. https://doi.org/10.5194/acp-20-8909-](https://doi.org/10.5194/acp-20-8909-2020)
1517 [2020](https://doi.org/10.5194/acp-20-8909-2020)

1518 [Fiore, A., Jacob, D.J., Liu, H., Yantosca, R.M., Fairlie, T.D., Li, Q., \(2003\). Variability in surface ozone](https://doi.org/10.1029/2003JD003855)
1519 [background over the United States: Implications for air quality policy. *J. Geophys. Res. Atmos.*](https://doi.org/10.1029/2003JD003855)
1520 [108 \(D24\). https://doi.org/10.1029/2003JD003855. 4787](https://doi.org/10.1029/2003JD003855)

1521 [Fonseca, R., & Francis, D. \(2023\). Satellite derived trends and variability of CO₂ concentrations in the](https://doi.org/10.3389/fenvs.2023.1289142)
1522 [Middle East during 2014–2023. *Frontiers in Environmental Science*, *11*.](https://doi.org/10.3389/fenvs.2023.1289142)
1523 <https://doi.org/10.3389/fenvs.2023.1289142>

1524 [Fonseca, R., Francis, D., Nelli, N., Farrah, S., Wehbe, Y., Al Hosari, T., & Al Mazroui, A. \(2022a\)](https://doi.org/10.1029/2022EA002269)
1525 [Assessment of the WRF model as a guidance tool into cloud seeding operations in the United](https://doi.org/10.1029/2022EA002269)
1526 [Arab Emirates. *Earth and Space Science*, *9*, e2022EA002269.](https://doi.org/10.1029/2022EA002269)
1527 <https://doi.org/10.1029/2022EA002269>

Formatted: Default Paragraph Font, Font color: Blue

Field Code Changed

Formatted: English (U.A.E.)

Field Code Changed

Formatted: Default Paragraph Font, Font color: Blue,
English (U.A.E.)

Formatted: English (U.A.E.)

1528 Fonseca, R., Francis, D., Nelli, N., & Thota, M. (2022). Climatology of the heat low and the
1529 intertropical discontinuity in the Arabian Peninsula. *International Journal of Climatology*, 42(2),
1530 1092–1117. <https://doi.org/10.1002/joc.7291><https://doi.org/10.1002/joc.7291>

1531 Fonseca, R., Francis, D., Weston, M., Nelli, N., Farah, S., Wehbe, Y., Alhosari, T., Teixido, O., &
1532 Mohamed, R. (2021). Sensitivity of summertime convection to aerosol loading and properties in
1533 the ~~united arab emirates~~United Arab Emirates. *Atmosphere*, 12(12).
1534 <https://doi.org/10.3390/atmos12121687><https://doi.org/10.3390/atmos12121687>

1535 Fonseca, R., Temimi, M., Thota, M. S., Nelli, N. R., Weston, M. J., Suzuki, K., Uchida, J., Kumar, K. N.,
1536 Branch, O., Wehbe, Y., Al Hosari, T., Al Shamsi, N., & Shalaby, A. (2020). On the analysis of the
1537 performance of WRF and nicam in a hyperarid environment. *Weather and Forecasting*, 35(3),
1538 891–919. <https://doi.org/10.1175/WAF-D-19-0210.1><https://doi.org/10.1175/WAF-D-19-0210.1>

1539 Francis, D., Fonseca, R., Nelli, N., Cuesta, J., Weston, M., Evan, A., & Temimi, M. (2020). The
1540 Atmospheric Drivers of the Major Saharan Dust Storm in June 2020. In *Geophysical Research*
1541 *Letters* (Vol. 47, Issue 24). Blackwell Publishing Ltd.
1542 <https://doi.org/10.1029/2020GL090102><https://doi.org/10.1029/2020GL090102>

1543 Francis, D., Fonseca, R., Nelli, N., Teixido, O., Mohamed, R., & Perry, R. (2022a). Increased Shamal
1544 winds and dust activity over the Arabian Peninsula during the COVID-19 lockdown period in 2020.
1545 *Aeolian Research*, 55, 100786.
1546 <https://doi.org/10.1016/j.aeolia.2022.100786><https://doi.org/10.1016/j.aeolia.2022.100786>

1547 Francis, D., Nelli, N., Fonseca, R., Weston, M., Flamant, C., & Cherif, C. (2022b). The dust load and
1548 radiative impact associated with the June 2020 historical Saharan dust storm. *Atmospheric*
1549 *Environment*, 268.
1550 <https://doi.org/10.1016/j.atmosenv.2021.118808><https://doi.org/10.1016/j.atmosenv.2021.118808>
1551 808

1552 Francis, D., Temimi, M., Fonseca, R., Nelli, N. R., Abida, R., Weston, M., Wehbe, Y. (2021) On the
1553 analysis of a summertime convective event in a hyperarid environment. *Quarterly Journal of the*
1554 *Royal Meteorological Society*, 147, 501-525. <https://doi.org/10.1002/qj.3930>

1555 Francis, D., Weston, M., Fonseca, R., Temimi, M., & Alsuwaidi, A. (2023). Trends and variability in
1556 methane concentrations over the Southeastern Arabian Peninsula. *Frontiers in Environmental*
1557 *Science*, 11. <https://doi.org/10.3389/fenvs.2023.1177877>

1558 [Gao, J., Li, Y., Xie, Z., Wang, L., Hu, B., & Bao, F. \(2023\). Which aerosol type dominate the impact
1559 of aerosols on ozone via changing photolysis rates? *Science of the Total Environment*, 854.
1560 <https://doi.org/10.1016/j.scitotenv.2022.158580>](https://doi.org/10.1016/j.scitotenv.2022.158580)

1561 Gao, Z., & Zhou, X. (2024). A review of the CAMx, CMAQ, WRF-Chem and NAQPMS models:
1562 Application, evaluation and uncertainty factors. *Environmental Pollution*, 343, 123183.
1563 <https://doi.org/10.1016/j.envpol.2023.123183>

1564 Gauss, M., 2003. Radiative forcing in the 21st century due to ozone changes in the tro posphere and
1565 the lower stratosphere. *J. Geophys. Res.* 108 (D9), 4292. [https://doi.
1566 org/10.1029/2002JD002624](https://doi.org/10.1029/2002JD002624)

Formatted: English (U.A.E.)

Formatted: English (U.A.E.)

Formatted: Default Paragraph Font, Font color: Blue

Field Code Changed

Formatted: English (U.A.E.)

Field Code Changed

Formatted: Default Paragraph Font, Font color: Black, English (U.A.E.)

Formatted: Font color: Black, English (U.A.E.)

1567 Geng, F., Zhao, C., Tang, X., Lu, G., & Tie, X. (2007). Analysis of ozone and VOCs measured in Shanghai:
 1568 A case study. *Atmospheric Environment*, 41(5), 989–1001.
 1569 <https://doi.org/10.1016/j.atmosenv.2006.09.023>

1570 <https://doi.org/10.5270/S5P-ft13p57>
 1571 German Aerospace Center (DLR), Copernicus Sentinel data processed by ESA (2020) Sentinel-5P
 1572 TROPOMI Total Ozone Column 1-Orbit L2 5.5 km x 3.5 km. Greenbelt, MD, USA, Goddard Earth
 1573 Sciences Data and Information Services Center (GES DISC) [Dataset]. Accessed on 10 October
 1574 2023, available online at <https://doi.org/10.1016/j.atmosenv.2006.09.023>

1575 Georgiou, G. K., Christoudias, T., Proestos, Y., Kushta, J., Hadjinicolaou, P., & Lelieveld, J. (2018). Air
 1576 quality modelling in the summer over the eastern Mediterranean using WRF-Chem: Chemistry
 1577 and aerosol mechanism intercomparison. *Atmospheric Chemistry and Physics*, 18(3), 1555–1571.
 1578 <https://doi.org/10.5194/acp-18-1555-2018><https://doi.org/10.5194/acp-18-1555-2018>

1579 <https://doi.org/10.1175/MWR-D-22-0082.1>
 1580 Gopalakishnan, D., Taraphdar, S., Pauluis, O. M., Xue, L., Ajayamohan, R. S., Al Shamsi, N., Chen, S.,
 1581 Lee, J. A., Grabowski, W. W., Liu, C., Tessendorf, S. A., Rasmussen, R. M. (2023) Anatomy of a
 1582 Summertime Convective Event over the Arabian Region. *Monthly Weather Review*, 151, 989-
 1004. <https://doi.org/10.1175/MWR-D-22-0082.1>

1583 Grell, G. a., Peckham, S. E., Schmitz, R., McKeen, S. a., Frost, G., Skamarock, W. C., & Eder, B. (2005).
 1584 Fully coupled “online” chemistry within the WRF model. *Atmospheric Environment*, 39(37),
 1585 6957–6975.
 1586 <https://doi.org/10.1016/j.atmosenv.2005.04.027>[https://doi.org/10.1016/j.atmosenv.2005.04.0](https://doi.org/10.1016/j.atmosenv.2005.04.027)
 1587 [27](https://doi.org/10.1016/j.atmosenv.2005.04.027)

1588 Griffin, D., Zhao, X., McLinden, C. A., Boersma, F., Bourassa, A., Dammers, E., Degenstein, D., Eskes, H.,
 1589 Fehr, L., Fioletov, V., Hayden, K., Kharol, S. K., Li, S. M., Makar, P., Martin, R. V., Mihele, C.,
 1590 Mittermeier, R. L., Krotkov, N., Snee, M., ... Wolde, M. (2019). High-Resolution Mapping of
 1591 Nitrogen Dioxide With TROPOMI: First Results and Validation Over the Canadian Oil Sands.
 1592 *Geophysical Research Letters*, 46(2), 1049–1060.
 1593 <https://doi.org/10.1029/2018GL081095><https://doi.org/10.1029/2018GL081095>

1594 Guenther, A. B., Jiang, X., Heald, C. L., Sakulyanontvittaya, T., Duhl, T., Emmons, L. K., & Wang, X.
 1595 (2012). The model of emissions of gases and aerosols from nature version 2.1 (MEGAN2.1): An
 1596 extended and updated framework for modeling biogenic emissions. *Geoscientific Model*
 1597 *Development*, 5(6), 1471–1492. <https://doi.org/10.5194/gmd-5-1471-2012>

1598 <https://doi.org/10.5194/gmd-17-4331-2024>
 1599 Guo, Y., Roychoudhury, C., Mirrezaei, M. A., Kumar, R., Sorooshian, A., & Arellano, A. F. (2024a)
 1600 Investigating ground-level ozone pollution in semi-arid and arid regions of Arizona using WRF-
 1601 Chem v4.4 modeling. *Geoscientific Model Development*, 17, 4331-4353.
<https://doi.org/10.5194/gmd-17-4331-2024>

1602 <https://doi.org/10.3390/f15030508>
 1603 Guo, P., Su, Y., Sun, X., Liu, C., Cui, B., Xu, X., Ouyang, Z., Wang, X. (2024b) Urban-Rural Comparisons
 1604 of Biogenic Volatile Organic Compounds and Ground-Level Ozone in Beijing. *Forests*, 15, 508.
<https://doi.org/10.3390/f15030508>

1605 Hersbach, H., Bell, B., Berrisford, P., Biavati, G., Horanyi, A., Muñoz Sabater, J., Nicolas, J., Peubey, C.,
 1606 Radu, R., Rozum, I., Schepers, D., Simmons, A., Soci, C., Dee, D., & Thepaut, J.-N. (2023a) ERA5
 1607 hourly data on single levels from 1940 to present. Copernicus Climate Change Service Climate
 1608 Data Store [Dataset]. Accessed on 14 November 2023, available online at
 1609 <https://doi.org/10.24381/cds.adbb2d47><https://doi.org/10.24381/cds.adbb2d47>

Formatted: English (U.A.E.)

Formatted: Indent: First line: 0 cm, Adjust space between Latin and Asian text, Adjust space between Asian text and numbers

Formatted: Default Paragraph Font, Font color: Blue

Field Code Changed

Formatted: Font: Calibri

Formatted: Normal, Border: Top: (No border), Bottom: (No border), Left: (No border), Right: (No border), Between : (No border)

Formatted: Font: Calibri

1610 Hersbach, H., Bell, B., Berrisford, P., Biavati, G., Horanyi, A., Muñoz Sabater, J., Nicolas, J., Peubey, C.,
 1611 Radu, R., Rozum, I., Schepers, D., Simmons, A., Soci, C., Dee, D., & Thepaut, J.-N. (2023b) ERA5
 1612 hourly data on pressure levels from 1940 to present. Copernicus Climate Change Service Climate
 1613 Data Store [Dataset]. Accessed on 14 November 2023, available online at
 1614 <https://doi.org/10.24381/cds.bd0915c6><https://doi.org/10.24381/cds.bd0915c6>

1615 Hersbach, H., Bell, B., Berrisford, P., Hirahara, S., Horányi, A., Muñoz-Sabater, J., Nicolas, J., Peubey,
 1616 C., Radu, R., Schepers, D., Simmons, A., Soci, C., Abdalla, S., Abellan, X., Balsamo, G., Bechtold,
 1617 P., Biavati, G., Bidlot, J., Bonavita, M., ... Thépaut, J. N. (2020). The ERA5 global reanalysis.
 1618 *Quarterly Journal of the Royal Meteorological Society*, 146(730), 1999–2049.
 1619 <https://doi.org/10.1002/qj.3803>

1620 [Holben, B. N., Eck, T. F., Slutsker, I., Tanre, D., Buis, J. P., Setzer, A., Vermote, E., Reagan, J. A., Kaufman,
 1621 Y. J., Nakajima, T., Lavenu, F., Jankowiak, I., and Smirnov, A.: AERONET– A federated instrument
 1622 network and data archive for aerosol characterization, *Remote Sens. Environ.*, 66, 1–16,
 1623 \[https://doi.org/10.1016/s0034-4257\\(98\\)00031-5\]\(https://doi.org/10.1016/s0034-4257\(98\)00031-5\), 1998.](https://doi.org/10.1016/s0034-4257(98)00031-5)

1624 Hong, S. Y. (2010). A new stable boundary-layer mixing scheme and its impact on the simulated East
 1625 Asian summer monsoon. *Quarterly Journal of the Royal Meteorological Society*, 136(651), 1481–
 1626 1496. <https://doi.org/10.1002/qj.665><https://doi.org/10.1002/qj.665>

1627 Hoshyaripour, G., Brasseur, G., Andrade, M. F., Gavidia-Calderón, M., Bouarar, I., & Ynoue, R. Y. (2016).
 1628 Prediction of ground-level ozone concentration in São Paulo, Brazil: Deterministic versus statistic
 1629 models. *Atmospheric Environment*, 145, 365–375.
 1630 <https://doi.org/10.1016/j.atmosenv.2016.09.061>

1631 [Hsu, N. C., M.-J. Jeong, C. Bettenhausen, A. M. Sayer, R. Hansell, C. S. Seftor, J. Huang, and S.-C. Tsay.
 1632 2015. "Enhanced Deep Blue Aerosol Retrieval Algorithm : The Second Generation." 118\(April\):
 1633 9296–9315.](https://doi.org/10.1016/j.atmosenv.2015.11.022)

1634 Hu, C., Kang, P., Jaffe, D. A., Li, C., Zhang, X., Wu, K., & Zhou, M. (2021). Understanding the impact of
 1635 meteorology on ozone in 334 cities of China. *Atmospheric Environment*, 248.
 1636 <https://doi.org/10.1016/j.atmosenv.2021.118221><https://doi.org/10.1016/j.atmosenv.2021.118221>
 1637 221

1638 Iacono, Michael J, Jennifer S Delamere, Eli J Mlawer, Mark W Shephard, Shepard A Clough, and William
 1639 D Collins. 2008. "Radiative Forcing by Long-Lived Greenhouse Gases: Calculations with the AER
 1640 Radiative Transfer Models." *Journal of Geophysical Research: Atmospheres* 113 (D13).
 1641 <https://doi.org/10.1029/2008JD009944><https://doi.org/10.1029/2008JD009944>

1642 Ialongo, I., Virta, H., Eskes, H., Hovila, J., & Douros, J. (2020). Comparison of TROPOMI/Sentinel-5
 1643 Precursor NO2 observations with ground-based measurements in Helsinki. *Atmospheric
 1644 Measurement Techniques*, 13(1), 205–218. [https://doi.org/10.5194/amt-13-205-
 1645 2020](https://doi.org/10.5194/amt-13-205-2020)<https://doi.org/10.5194/amt-13-205-2020>

1646 Ivatt, P. D., & Evans, M. J. (2020). Improving the prediction of an atmospheric chemistry transport
 1647 model using gradient-boosted regression trees. *Atmospheric Chemistry and Physics*, 20(13),
 1648 8063–8082. [https://doi.org/10.5194/acp-20-8063-
 1649 2020](https://doi.org/10.5194/acp-20-8063-2020)<https://doi.org/10.5194/acp-20-8063-2020>

Formatted: Font: Calibri

Formatted: Default Paragraph Font, Font color: Blue

Field Code Changed

Formatted: English (U.A.E.)

Formatted: Adjust space between Latin and Asian text,
Adjust space between Asian text and numbers

Field Code Changed

Formatted: Default Paragraph Font, Font color: Blue

Formatted: Adjust space between Latin and Asian text,
Adjust space between Asian text and numbers

1650 [Jacobson, M.Z., \(1998\). Studying the effects of aerosols on vertical photolysis rate coefficient and](#)
 1651 [temperature profiles over an urban airshed Gas photochemistry Gasto-pxticle conversion Wind](#)
 1652 [speed Wind direction Air pressure Nucleation Freezing/ Melting. J. Geophys. Res. 103.](#)

1653 Jena, C., Ghude, S. D., Kumar, R., Debnath, S., Govardhan, G., Soni, V. K., Kulkarni, S. H., Beig, G., &
 1654 Nanjundiah, R. S. (2021). Performance of high resolution (400 m) P M 2 . 5 forecast over Delhi.
 1655 *Scientific Reports*, 400 m, 1–9. [https://doi.org/10.1038/s41598-021-83467-](https://doi.org/10.1038/s41598-021-83467-8)
 1656 [8](https://doi.org/10.1038/s41598-021-83467-8)<https://doi.org/10.1038/s41598-021-83467-8>

1657 Kain, J. S. (2004). The Kain-Fritsch Convective Parameterization: An Update. *Journal of Applied*
 1658 *Meteorology*, 43, 170–181. [https://doi.org/10.1175/1520-](https://doi.org/10.1175/1520-0450(2004)043<0170:TKCPAU>2.0.CO;2)
 1659 [0450\(2004\)043<0170:TKCPAU>2.0.CO;2](https://doi.org/10.1175/1520-0450(2004)043<0170:TKCPAU>2.0.CO;2)[https://doi.org/10.1175/1520-](https://doi.org/10.1175/1520-0450(2004)043<0170:TKCPAU>2.0.CO;2)
 1660 [0450\(2004\)043<0170:TKCPAU>2.0.CO;2](https://doi.org/10.1175/1520-0450(2004)043<0170:TKCPAU>2.0.CO;2)

1661 Karagulian, F., Temimi, M., Ghebreyesus, D., Weston, M., Kondapalli, N. K., Valappil, V. K., Aldababesh,
 1662 A., Lyapustin, A., Chaouch, N., Al Hammadi, F., & Al Abdooli, A. (2019) Analysis of a severe dust
 1663 storm and its impact on air quality conditions using WRF-Chem modeling, satellite imagery, and
 1664 ground observations. *Air Quality, Atmosphere & Health*, 12, 453-470.
 1665 <https://doi.org/10.1007/s11869-019-00674-z><https://doi.org/10.1007/s11869-019-00674-z>

1666 Karumuri, R. K., Dasari, H. P., Gandham, H., Viswanadhapalli, Y., Madineni, V. R., & Hoteit, I. (2022).
 1667 Impact of COVID-19 lockdown on the ambient air-pollutants over the Arabian Peninsula.
 1668 *Frontiers in Environmental Science*, 10.
 1669 <https://doi.org/10.3389/fenvs.2022.963145><https://doi.org/10.3389/fenvs.2022.963145>

1670 Kerkweg, A., & Jöckel, P. (2012). The 1-way on-line coupled atmospheric chemistry model system
 1671 MECO(n) - Part 1: Description of the limited-area atmospheric chemistry model COSMO/MESSy.
 1672 *Geoscientific Model Development*, 5(1), 87–110. [https://doi.org/10.5194/gmd-5-87-](https://doi.org/10.5194/gmd-5-87-2012)
 1673 [2012](https://doi.org/10.5194/gmd-5-87-2012)<https://doi.org/10.5194/gmd-5-87-2012>

1674 Kishta, M., Al Abadla, Z., Wahab, M. M. A., & Aldashti, H. (2023). Assessment of Heat Wave Indexing*
 1675 and Performance of ERA5 in Simulating Temperature and Precipitation Dataset over the UAE.
 1676 *Environment Asia*, 16(2), 48–65. <https://doi.org/10.14456/ea.2023.20>

1677 Koninklijk Nederlands Meteorologisch Instituut (KNMI), Copernicus Sentinel data processed by ESA
 1678 (2018) Sentinel-5P TROPOMI Tropospheric NO₂ 1-Orbit L2 7 km x 3.5 km. Greenbelt, MD, USA,
 1679 Goddard Earth Sciences Data and Information Services Center (GES DISC) [Dataset]. Accessed on
 1680 10 October 2023, available online at [https://doi.org/10.5270/S5P-](https://doi.org/10.5270/S5P-s4lig54)
 1681 [s4lig54](https://doi.org/10.5270/S5P-s4lig54)[https://doi.org/10.5270/S5P-](https://doi.org/10.5270/S5P-s4lig54)
 1682 Koninklijk Nederlands Meteorologisch Instituut/Netherlands Institute for Space Research
 1683 (KNMI/SRON), Copernicus Sentinel data processed by ESA (2021) Sentinel-5P TROPOMI
 1684 Tropospheric Carbon Monoxide CO 1-Orbit L2 5.5 km x 7 km. Greenbelt, MD, USA, Goddard Earth
 1685 Sciences Data and Information Services Center (GES DISC) [Dataset]. Accessed on 10 October
 1686 2023, available online at [https://doi.org/10.5270/S5P-](https://doi.org/10.5270/S5P-bi3nry0)
 1687 [bi3nry0](https://doi.org/10.5270/S5P-bi3nry0)[https://doi.org/10.5270/S5P-](https://doi.org/10.5270/S5P-bi3nry0)

1688 Koo, Y. S., Kim, S. T., Cho, J. S., & Jang, Y. K. (2012). Performance evaluation of the updated air quality
 1689 forecasting system for Seoul predicting PM 10. *Atmospheric Environment*, 58(3), 56–69.
 1690 <https://doi.org/10.1016/j.atmosenv.2012.02.004><https://doi.org/10.1016/j.atmosenv.2012.02.004>
 1691 [04](https://doi.org/10.1016/j.atmosenv.2012.02.004)

Formatted: Adjust space between Latin and Asian text, Adjust space between Asian text and numbers

Field Code Changed

Formatted: Default Paragraph Font, Font color: Blue

- 1692 Krol, M., Houweling, S., Bregman, B., Van Den Broek, M., Segers, A., Van Velthoven, P., Peters, W.,
1693 Dentener, F., & Bergamaschi, P. (2005). The two-way nested global chemistry-transport zoom
1694 model TM5: algorithm and applications. In *Atmos. Chem. Phys* (Vol. 5). [www.atmos-chem-](http://www.atmos-chem-phys.org/acp/5/417/SRef-ID:1680-7324/acp/2005-5-417EuropeanGeosciencesUnion)
1695 [phys.org/acp/5/417/SRef-ID:1680-](http://www.atmos-chem-phys.org/acp/5/417/SRef-ID:1680-7324/acp/2005-5-417EuropeanGeosciencesUnion)
1696 [7324/acp/2005-5-417EuropeanGeosciencesUnion](http://www.atmos-chem-phys.org/acp/5/417/SRef-ID:1680-7324/acp/2005-5-417EuropeanGeosciencesUnion)
1697
- 1698 [Kaufman, Y. J., Tanre, D., Rmer, L. A., Vermote, E. F., Chu, A., & Holben, B. N. \(1997\) Operational](https://doi.org/10.1029/96JD03988)
1699 [remote sensing of tropospheric aerosol over land from EOS moderate resolution imaging](https://doi.org/10.1029/96JD03988)
1700 [spectroradiometer. *Journal of Geophysical Research*, 102, 17051-17067.](https://doi.org/10.1029/96JD03988)
1701 <https://doi.org/10.1029/96JD03988>
- 1702 Kumar, R. (2011). Weather Research and Forecasting Model with Chemistry (WRF-CHEM) over South
1703 Asia. *Pubman.MpdI.Mpg.De*. Accessed on 10 July 2023, available online at
1704 [http://pubman.mpg.de/pubman/item/escidoc:994147:1/component/escidoc:994146/Bz-](http://pubman.mpg.de/pubman/item/escidoc:994147:1/component/escidoc:994146/BzE-57.pdf)
1705 [E-57.pdf](http://pubman.mpg.de/pubman/item/escidoc:994147:1/component/escidoc:994146/BzE-57.pdf)[http://pubman.mpg.de/pubman/item/escidoc:994147:1/component/escidoc:99](http://pubman.mpg.de/pubman/item/escidoc:994147:1/component/escidoc:994146/BzE-57.pdf)
1706 [4146/BzE 57.pdf](http://pubman.mpg.de/pubman/item/escidoc:994147:1/component/escidoc:994146/BzE-57.pdf)
- 1707 Kumar, R., Barth, M. C., Pfister, G. G., Delle Monache, L., Lamarque, J. F., Archer-Nicholls, S., ... Walters,
1708 S. (2018). How Will Air Quality Change in South Asia by 2050? *Journal of Geophysical Research:*
1709 *Atmospheres*, 123(3), 1840–1864.
1710 <https://doi.org/10.1002/2017JD027357><https://doi.org/10.1002/2017JD027357>
- 1711 Kumar, R., Bhardwaj, P., Pfister, G., Drews, C., Honomichl, S., & D'attilo, G. (2021). Description and
1712 evaluation of the fine particulate matter forecasts in the NCAR regional air quality forecasting
1713 system. *Atmosphere*, 12(3).
1714 <https://doi.org/10.3390/atmos12030302><https://doi.org/10.3390/atmos12030302>
- 1715 Kumar, R., Naja, M., Pfister, G. G., Barth, M. C., Wiedinmyer, C., & Brasseur, G. P. (2012). Simulations
1716 over South Asia using the Weather Research and Forecasting model with Chemistry (WRF-Chem):
1717 Chemistry evaluation and initial results. *Geoscientific Model Development*, 5(3), 619–648.
1718 <https://doi.org/10.5194/gmd-5-619-2012><https://doi.org/10.5194/gmd-5-619-2012>
- 1719 Labow, G. J., Ziemke, J. R., McPeters, R. D., Haffner, D. P., & Bhartia, P. K. (2015). A total ozone-
1720 dependent ozone profile climatology based on ozonesondes and Aura MLS data. *Journal of*
1721 *Geophysical Research*, 120(6), 2537–2545.
1722 <https://doi.org/10.1002/2014JD022634><https://doi.org/10.1002/2014JD022634>
- 1723 Lambert, J.-C., A. Keppens, S. Compennolle, K.-U. Eichmann, M. de Graaf, D. Hubert, B. Langerock, A.
1724 Ludewig, M.K. Sha, T. Verhoelst, T. Wagner, C. Ahn, A. Argyrouli, D. Balis, K.L. Chan, M. Coldewey-
1725 Egbers, I. De Smedt, H. Eskes, A.M. Fjæraa, ... M. Weber. (2023). *Quarterly Validation Report of*
1726 *the Copernicus Sentinel-5 Precursor Operational Data Products #21: April 2018-November 2023*.
- 1727 Landgraf, J., Aan De Brugh, J., Scheepmaker, R., Borsdorff, T., Hu, H., Houweling, S., Butz, A., Aben, I.,
1728 & Hasekamp, O. (2016). Carbon monoxide total column retrievals from TROPOMI shortwave
1729 infrared measurements. *Atmospheric Measurement Techniques*, 9(10), 4955–4975.
1730 <https://doi.org/10.5194/amt-9-4955-2016>
- 1731 [Levy, R C et al. 2013. "The Collection 6 MODIS Aerosol Products over Land and Ocean." *Atmospheric*](https://doi.org/10.5194/amt-9-4955-2016)
1732 [Measurement Techniques](https://doi.org/10.5194/amt-9-4955-2016) (6): 2989–3034.

Formatted: English (U.A.E)

Field Code Changed

Formatted: Default Paragraph Font, Font color: Blue

1733 [Li, J., Wang, Z. F., Wang, X., Yamaji, K., Takigawa, M., Kanaya, Y., Pochanart, P., Liu, Y., Irie, H., Hu, B.,](#)
1734 [Tanimoto, H., and Akimoto, H \(2011\), Impacts of aerosols on summertime tropospheric](#)
1735 [photolysis frequencies and photochemistry over Central Eastern China, *Atmos. Environ.*, *45*,](#)
1736 [1817–1829, <https://doi.org/10.1016/j.atmosenv.2011.01.016>.](#)

1737 Li, T. Y., Deng, X. J., Li, Y., Song, Y. S., Li, L. Y., Tan, H. B., & Wang, C. L. (2018). Transport paths and
1738 vertical exchange characteristics of haze pollution in Southern China. *Science of the Total*
1739 *Environment*, *625*, 1074–1087.
1740 <https://doi.org/10.1016/j.scitotenv.2017.12.235><https://doi.org/10.1016/j.scitotenv.2017.12.235>
1741 [5](#)

1742 Li, Y., Gibson, J. M. D., Jat, P., Puggioni, G., Hasan, M., West, J. J., Vizuete, W., Sexton, K., & Serre, M.
1743 (2010). Burden of disease attributed to anthropogenic air pollution in the United Arab Emirates:
1744 Estimates based on observed air quality data. *Science of the Total Environment*, *408*(23), 5784–
1745 5793. <https://doi.org/10.1016/j.scitotenv.2010.08.017>

1746 [Li, Z., Zhao, X., Kahn, R., Mishchenko, M., Remer, L., Lee, K., Wang, M., Laszlo, I., Nakajima, T., &](#)
1747 [Maring, H. \(2015\). Uncertainties in satellite remote sensing of aerosols and impact on monitoring](#)
1748 [its long-term trend: a review and perspective. *Annales Geophysicae*, *27*, 2755–2770. \[www.ann-\]\(http://www.ann-geophys.net/27/2755/2009/\)](#)
1749 [geophys.net/27/2755/2009/](#)

1750 Liu, F., Tao, Z., Beirle, S., Joiner, J., Yoshida, Y., Smith, S. J., Knowland, K. E., & Wagner, T. (2022). A new
1751 method for inferring city emissions and lifetimes of nitrogen oxides from high-resolution
1752 nitrogen dioxide observations: A model study. *Atmospheric Chemistry and Physics*, *22*(2), 1333–
1753 1349. <https://doi.org/10.5194/acp-22-1333-2022>

1754 [Lou, S. J., Liao, H., and Zhu, B \(2014\), Impacts of aerosols on surface-layer ozone concentrations in](#)
1755 [China through heterogeneous reactions and changes in photolysis rates. *Atmos. Environ.*, *85*,](#)
1756 [123–138, <https://doi.org/10.1016/j.atmosenv.2013.12.004>.](#)

1757 Lu, X., Zhang, L., & Shen, L. (2019). Meteorology and Climate Influences on Tropospheric Ozone: a
1758 Review of Natural Sources, Chemistry, and Transport Patterns. In *Current Pollution Reports* (Vol.
1759 5, Issue 4, pp. 238–260). Springer. [https://doi.org/10.1007/s40726-019-00118-](https://doi.org/10.1007/s40726-019-00118-3)
1760 [3](#)<https://doi.org/10.1007/s40726-019-00118-3>

1761 Madronich, S. (1987). Photodissociation in the atmosphere: 1. Actinic flux and the effects of ground
1762 reflections and clouds. *Journal of Geophysical Research: Atmospheres*, *92*(D8), 9740–9752.
1763 <https://doi.org/10.1029/JD092iD08p09740><https://doi.org/10.1029/JD092iD08p09740>
1764 [029/JD092iD08p09740](#)

1765 Manders, A. M. M., Builtjes, P. J. H., Curier, L., Gon, H. A. C. D. Vander, Hendriks, C., Jonkers, S.,
1766 Kranenburg, R., Kuenen, J. J. P., Segers, A. J., Timmermans, R. M. A., Visschedijk, A. J. H., Kruit, R.
1767 J. W., Pul, W. A. J. V., Sauter, F. J., Van Der Swaluw, E., Swart, D. P. J., Douros, J., Eskes, H., Van
1768 Meijgaard, E., ... Schaap, M. (2017). Curriculum vitae of the LOTOS-EUROS (v2.0) chemistry
1769 transport model. *Geoscientific Model Development*, *10*(11), 4145–4173.
1770 <https://doi.org/10.5194/gmd-10-4145-2017><https://doi.org/10.5194/gmd-10-4145-2017>

1771 Mathworks (2023) MATLAB. Maths. Graphic. Programming [Software]. Accessed on 10 July 2023,
1772 available online at
1773 <https://uk.mathworks.com/products/matlab.html>[https://uk.mathworks.com/products/matlab.](https://uk.mathworks.com/products/matlab.html)
1774 [html](#)

Formatted: Default Paragraph Font, Font color: Blue

Field Code Changed

Formatted: Adjust space between Latin and Asian text,
Adjust space between Asian text and numbers

Field Code Changed

Formatted: Default Paragraph Font, Font color: Blue

Formatted: Adjust space between Latin and Asian text,
Adjust space between Asian text and numbers

1775 Menut, L., Bessagnet, B., Briant, R., Cholakian, A., Couvidat, F., Mailler, S., Pennel, R., Siour, G.,
 1776 Tuccella, P., Turquety, S., & Valari, M. (2021). The CHIMERE v2020r1 online chemistry-transport
 1777 model. *Geoscientific Model Development*, 14(11), 6781–6811. [https://doi.org/10.5194/gmd-14-](https://doi.org/10.5194/gmd-14-6781-2021)
 1778 [6781-2021](https://doi.org/10.5194/gmd-14-6781-2021)<https://doi.org/10.5194/gmd-14-6781-2021>

1779 Morrison, H., Thompson, G., & Tatarskii, V. (2009). Impact of cloud microphysics on the development
 1780 of trailing stratiform precipitation in a simulated squall line: Comparison of one- and two-
 1781 moment schemes. *Monthly Weather Review*, 137(3), 991–1007.
 1782 <https://doi.org/10.1175/2008MWR2556.1><https://doi.org/10.1175/2008MWR2556.1>

1783 Mostamandi, S., Ukhov, A., Engelbrecht, J., Shevchenko, I., Osipov, S., & Stenchikov, G. (2023). Fine
 1784 and coarse dust effects on radiative forcing, mass deposition, and solar devices over the Middle
 1785 East. *Journal of Geophysical Research: Atmospheres*, 128, e2023JD039479.
 1786 <https://doi.org/10.1029/2023JD039479>

1787 Mukherjee, T., Vinoj, V., Midya, S. K., Adhikary, B. (2020) Aerosol radiative impact on surface ozone
 1788 during a heavy dust and biomass burning event over South Asia. *Atmospheric Environment*, 223,
 1789 117201. <https://doi.org/10.1016/j.atmosenv.2019.117201>

1790 National Center for Atmospheric Research (2023) Download WRF-CHEM Processors [Dataset].
 1791 Accessed on 10 July 2023, available online at [https://www.acom.ucar.edu/wrf-](https://www.acom.ucar.edu/wrf-chem/download.shtml)
 1792 [chem/download.shtml](https://www.acom.ucar.edu/wrf-chem/download.shtml)<https://www.acom.ucar.edu/wrf-chem/download.shtml>

1793 National Centers for Environmental Prediction/National Weather Service/National Oceanic and
 1794 Atmospheric Administration/United States Department of Commerce (NCEP/NWS/NOAA/USDC)
 1795 (2000) NCEP FNL Operational Model Global Tropospheric Analyses, continuing from July 1999.
 1796 Research Data Archive at the National Center for Atmospheric Research, Computational and
 1797 Information Systems Laboratory [Dataset]. Accessed on 10 July 2023, available online at
 1798 <https://doi.org/10.5065/D6M043C6><https://doi.org/10.5065/D6M043C6>

1799 Nelli, N., Fissehay, S., Francis, D., Fonseca, R., Temimi, M., Weston, M., Abida, R., & Nesterov, O.
 1800 (2021) Characteristics of atmospheric aerosols over the UEA inferred from CALIPSO and sun
 1801 photometer aerosol optical depth. *Earth and Space Science*, 8, e2020EA001360.
 1802 <https://doi.org/10.1029/2020EA001360>

1803 Nelli, N., Francis, D., Alkatheeri, A., & Fonseca, R. (2024a). Evaluation of Reanalysis and Satellite
 1804 Products against Ground-Based Observations in a Desert Environment. *Remote Sensing*, 16,
 1805 3593. <https://doi.org/10.3390/rs16193593>

1806 Nelli, N., Francis, D., Fonseca, R., Masson, O., Sow, M., & Bosc, E. (2024b). First measurements of
 1807 electric field variability during fog events in the United Arab Emirates. *Journal of Arid*
 1808 *Environments*, 220. <https://doi.org/10.1016/j.jaridenv.2023.105096>

1809 Nelli, N., Francis, D., Fonseca, R., Bosc, E., Addad, Y., Temimi, M., Abida, R., Weston, M., Cherif,
 1810 C. (2022). Characterization of the atmospheric circulation near the Empty Quarter Desert during
 1811 major weather events. *Frontiers in Environmental Science*, 10, 972380.
 1812 <https://doi.org/10.3389/fenvs.2022.972380>

1813 Nelli, N., Francis, D., Sow, M., Fonseca, R., Alkatheeri, A., Bosc, E., & Bergametti, G. (2024c). The
 1814 Wind-Blown Sand Experiment in the Empty Quarter Desert: Roughness Length and Saltation
 1815 Characteristics. *Earth and Space Science*, 11(6). <https://doi.org/10.1029/2024EA003512>

Formatted: English (U.A.E.)

Field Code Changed

Formatted: Default Paragraph Font, Font color: Blue

1816 Nelli, N. R., Temimi, M., Fonseca, R. M., Weston, M. J., Thota, M. S., Valappil, V. K., Branch, O.,
1817 Wulfmeyer, V., Wehbe, Y., Al Hosary, T., Shalaby, A., Al Shamsi, N., & Al Naqbi, H. (2020) Impact
1818 of roughness length on WRF simulated land-atmospheres interactions over a hyper-arid region.
1819 *Earth and Space Science*, 7, e2020EA001165. <https://doi.org/10.1029/2020EA001165>
1820 <https://doi.org/10.1029/2020EA001165>

1821 [Nelli, N., Fissehaye, S., Francis, D., Fonseca, R., Temimi, M., Weston, M., Abida, R., & Nesterov,
1822 O. \(2021\). Characteristics of Atmospheric Aerosols Over the UAE Inferred From CALIPSO and Sun
1823 Photometer Aerosol Optical Depth. *Earth and Space Science*, 8\(6\).
1824 <https://doi.org/10.1029/2020EA001360>](https://doi.org/10.1029/2020EA001360)

1825

1826 Nesterov, O., Temimi, M., Fonseca, R., Nelli, N. R., Addad, Y., Bosc, E., & Abida, R. (2021). Validation
1827 and statistical analysis of the Group for High Resolution Sea Surface Temperature data in the
1828 Arabian Gulf. *Oceanologia*, 63(4), 497–515.
1829 <https://doi.org/10.1016/j.oceano.2021.07.001><https://doi.org/10.1016/j.oceano.2021.07.001>

1830 Nhu, T., Do, N., Ngo, X. T., Pham, V. H., Vuong, N. L., Le, H. A., & Pham, C. T. (2021). *Application of
1831 WRF-Chem to simulate air quality over Northern Vietnam. 2016*, 12067–12081.
1832 <https://doi.org/10.1007/s11356-020-08913-y>

1833 [Olivier, J., J. Peters, C. Granier, G. Pétron, J.F. Müller, and S. Wallens, Present and future surface
1834 emissions of atmospheric compounds, POET Report #2, EU project EVK2-1999-00011, 2003.](https://doi.org/10.1016/j.atmosenv.2003.07.001)

1835 Parajuli, S. P., Stenchikov, G. L., Ukhov, A., & Kim, H. (2019). Dust Emission Modeling Using a New High-
1836 Resolution Dust Source Function in WRF-Chem With Implications for Air Quality. *Journal of
1837 Geophysical Research: Atmospheres*, 124(17–18), 10109–10133.
1838 <https://doi.org/10.1029/2019JD030248>

1839 Parajuli, [Sagar S. P., Georgiy L. Stenchikov, Alexander G. L., Ukhov, Hugh L., Morrison, Hui H.,
1840 Shevchenko, and Suleiman A., & Mostamandi, S. \(2023-\). Simulation of a Dust-And-Rain Event
1841 Across the Red Sea Using WRF-Chem. *Journal of Geophysical Research: Atmospheres* 128 \(14\).
1842 <https://doi.org/10.1029/2022JD038384>](https://doi.org/10.1029/2022JD038384)

1843 Parajuli, [Sagar S. P., Georgiy L. Stenchikov, Alexander G. L., Ukhov, Suleiman A., Mostamandi, Paul A. S.,
1844 Kucera, Duncan P. A., Axisa, William I. D., Gustafson, W. I., and Yannian Zhu, Y. \(2022-\). Effect of
1845 Dust on Rainfall over the Red Sea Coast Based on WRF-Chem Model Simulations. *Atmospheric
1846 Chemistry and Physics* 22 \(13\): 8659–82. <https://doi.org/10.5194/acp-22-8659-2022>](https://doi.org/10.5194/acp-22-8659-2022)

1847 [Pauli, E., Cermak, J., Bendix, J., Stier, P. \(2024\) Synoptic scale controls and aerosol effects on fog and
1848 low stratus life cycle processes in Po valley, Italy. *Geophysical Research Letters*, 51,
1849 e2024GL111490. <https://doi.org/10.1029/2024GL111490>](https://doi.org/10.1029/2024GL111490)

1850 [Phanikumar, D. V., Basha, G., Ratnam, M. V., Kondapalli, N. K., Ouarda, T. B. M. K., Pangaluru, K. \(2020\)
1851 Assessment of particulate matter concentration and gaseous pollutants in urban and rural
1852 regions over the Emirate of Abu Dhabi, UAE. *Journal of Atmospheric and Solar-Terrestrial Physics*,
1853 199, 105217. <https://doi.org/10.1016/j.jastp.2020.105217>](https://doi.org/10.1016/j.jastp.2020.105217)

1854 [Powers, J. G., Klemp, J. B., Skamarock, W. C., Davis, C. A., Dudhia, J., Gill, D. O., Coen, J. L., Gochis,
1855 D. J., Ahmadov, R., Peckham, S. E., Grell, G. A., Michalakes, J., Trahan, S., Benjamin, S. G.,
1856 Alexander, C. R., Dimego, G. J., Wang, W., Schwartz, C. S., Romine, G. S., ... Duda, M. G. \(2017\).](https://doi.org/10.1016/j.atmosenv.2017.04.011)

Formatted: Indent: Left: 0 cm, First line: 0 cm

Formatted: Adjust space between Latin and Asian text,
Adjust space between Asian text and numbers

Formatted: Default Paragraph Font, Font color: Blue

Field Code Changed

Field Code Changed

Formatted: Default Paragraph Font, Font color: Blue

Formatted: Default Paragraph Font, Font color: Blue

Field Code Changed

Field Code Changed

Formatted: Default Paragraph Font, Font color: Blue

1857 [The weather research and forecasting model: Overview, system efforts, and future directions.](#)
1858 [Bulletin of the American Meteorological Society, 98\(8\), 1717–1737.](#)
1859 <https://doi.org/10.1175/BAMS-D-15-00308.1>

1860 Ramadan, E. (2015) Sustainable Urbanization in the Arabian Gulf Region: Problems and Challenges.
1861 *Arts and Social Sciences Journal*, 6:2. [https://doi.org/10.4172/2151-](https://doi.org/10.4172/2151-6200-10000109)
1862 [6200-10000109](https://doi.org/10.4172/2151-6200-10000109)<https://doi.org/10.4172/2151-6200:10000109>

1863 [Qu, Y., Voulgarakis, A., Wang, T., Kasoar, M., Wells, C., Yuan, C., Varma, S., Mansfield, L. \(2021\) A study](#)
1864 [of the effect of aerosols on surface ozone through meteorology feedbacks over China.](#)
1865 [Atmospheric Chemistry and Physics, 21, 5705–5718. https://doi.org/10.5194/acp-21-5705-2021](#)

1866 Reddy, K. K., Naja, M., Ojha, N., Mahesh, P., & Lal, S. (2012). Influences of the boundary layer evolution
1867 on surface ozone variations at a tropical rural site in India. *Journal of Earth System Science*,
1868 121(4), 911–922. <https://doi.org/10.1007/s12040-012-0200-z>

1869 [Remer LA, Kaufman YJ, Tanré D, Mattoo S, Chu DA, Martins JV, Li R-R, Ichoku C, Levy RC, Kleidman RG,](#)
1870 [Eck TF, Vermote E, Holben BN. 2005. "The MODIS Aerosol Algorithm, Products, and Validation."](#)
1871 [Journal of the Atmospheric Sciences 62: 947–973.](#)

1872 [Remer, Lorraine A et al. 2008. "Global Aerosol Climatology from the MODIS Satellite Sensors." 113: 1–](#)
1873 [18](#)

1874 Ritter, M., Müller, M. D., Tsai, M. Y., & Parlow, E. (2013). Air pollution modeling over very complex
1875 terrain: An evaluation of WRF-Chem over Switzerland for two 1-year periods. *Atmospheric*
1876 *Research*, 132–133, 209–222. <https://doi.org/10.1016/j.atmosres.2013.05.021>

1877 [Sayer, A M, LA Munchak, et al. 2014b. "MODIS Collection 6 Aerosol Products: Comparison between](#)
1878 [Aqua's e-Deep Blue, Dark Target, and 'Merged' Data Sets, and Usage Recommendations."](#)
1879 [Journal of Geophysical Research Atmospheres 119\(13\): 13965–89.](#)

1880 [Sayer, A M et al. 2015. "Effect of MODIS Terra Radiometric Calibration Improvements on Collection 6](#)
1881 [Deep Blue Aerosol Products : Validation and Terra / Aqua Consistency." Journal of Geophysical](#)
1882 [Research: Atmospheres 120\(12\): 157–74.](#)

1883 [Sayer, A M, N C Hsu, C Bettenhausen, and M Jeong. 2014a. "Validation and Uncertainty Estimates for](#)
1884 [MODIS Collection 6 ' Deep Blue ' Aerosol Data." Journal of Geophysical Research Atmospheres](#)
1885 [118\(July 2013\): 7864–73.](#)

1886 Schwitalla, T., Branch, O., & Wulfmeyer, V. (2020). Sensitivity study of the planetary boundary layer
1887 and microphysical schemes to the initialization of convection over the Arabian Peninsula.
1888 *Quarterly Journal of the Royal Meteorological Society*, 146(727), 846–869.
1889 <https://doi.org/10.1002/qj.3711><https://doi.org/10.1002/qj.3711>

1890 Shahbaz, M., Sbia, R., Hamdi, H., & Ozturk, I. (2014) Economic growth, electricity consumption,
1891 urbanization and environmental degradation relationship in United Arab Emirates. *Ecological*
1892 *Indicators*, 45, 622–631.
1893 <https://doi.org/10.1016/j.ecolind.2014.05.022><https://doi.org/10.1016/j.ecolind.2014.05.022>

1894 Shami, A. Al, Aawar, E. Al, Baayoun, A., Saliba, N. A., Kushta, J., Christoudias, T., & Lakkis, I. (2022).
1895 Updated national emission inventory and comparison with the Emissions Database for Global
1896 Atmospheric Research (EDGAR): case of Lebanon. *Environmental Science and Pollution Research*,
1897 29(20), 30193–30205. <https://doi.org/10.1007/s11356-021-17562-8>

Formatted: Adjust space between Latin and Asian text, Adjust space between Asian text and numbers

Field Code Changed

Formatted: Default Paragraph Font, Font color: Blue

Field Code Changed

Formatted: Default Paragraph Font, Font color: Blue

Formatted: Adjust space between Latin and Asian text, Adjust space between Asian text and numbers

Formatted: Default Paragraph Font, Font color: Blue

Field Code Changed

1898 [Shi, S., Zhu, B., Tang, G., Liu, C., An, J., Liu, D., Xu, J., Xu, H., Liao, H., & Zhang, Y. \(2022\).
1899 \[Observational Evidence of Aerosol Radiation Modifying Photochemical Ozone Profiles in the
1900 Lower Troposphere. *Geophysical Research Letters*, 49\\(15\\).
1901 <https://doi.org/10.1029/2022GL099274>\]\(#\)](#)

1902 Sicard, P., Crippa, P., De Marco, A., Castruccio, S., Giani, P., Cuesta, J., Paoletti, E., Feng, Z., & Anav, A.
1903 (2021). High spatial resolution WRF-Chem model over Asia: Physics and chemistry evaluation.
1904 *Atmospheric Environment*, 244(June 2020), 118004.
1905 [https://doi.org/10.1016/j.atmosenv.2020.118](https://doi.org/10.1016/j.atmosenv.2020.118004)
1906 [004](https://doi.org/10.1016/j.atmosenv.2020.118004)

1907 Sillman, S. (1999). The relation between ozone, NO_x and hydrocarbons in urban and polluted rural
1908 environments. In *Atmospheric Environment*, 33, 1821-1845. [https://doi.org/10.1016/S1352-](https://doi.org/10.1016/S1352-2310(98)00345-8)
1909 [2310\(98\)00345-8](https://doi.org/10.1016/S1352-2310(98)00345-8)[https://doi.org/10.1016/S1352-2310\(98\)00345-8](https://doi.org/10.1016/S1352-2310(98)00345-8)

1910 Skamarock WC, et al. (2008). A description of the advanced research WRF version 3, NCAR Tech. Note,
1911 NCAR/TN-468+STR. *Natl. Cent. for Atmos. Res. Boulder, Colorado, June*, 408.
1912 <https://doi.org/10.5065/D68S4MVH><https://doi.org/10.5065/D68S4MVH>

1913 Srinivas, R., Panicker, A. S., Parkhi, N. S., Peshin, S. K., & Beig, G. (2016). Sensitivity of online coupled
1914 model to extreme pollution event over a mega city Delhi. *Atmospheric Pollution Research*, 7(1),
1915 25–30. <https://doi.org/10.1016/j.apr.2015.07.001>

1916 [Taraphdar, S., Pauluis, O. M., Xue, L., Liu, C., Rasmussen, R., Ajayamohan, R. S., Tessendorf, S., Jing, X.,
1917 Chen, S., Grabowski, W. W. \(2021\) WRF gray zone simulations of precipitation over the Middle-
1918 East and the UAE: Impacts of physical parameterizations and resolution. *Journal of Geophysical
1919 Research: Atmospheres*, 126, e2021JD034648. <https://doi.org/10.1029/2021JD034648>](#)

1920 [Teixido, O., Tobias, A., Massague, J., Mohamed, R., Ekaabi, R., Hamed, H. I., Perry, R., Querol, X. & Al
1921 Hosani, S. \(2021\) The influence of COVID-19 preventive measures on the air quality in Abu Dhabi
1922 \(United Arab Emirates\). *Air Quality, Atmosphere & Health*, 14, 1071-1079.
1923 <https://doi.org/10.1007/s11869-021-01000-2>](#)

1924 Temimi, M., Fonseca, R., Nelli, N., ~~Valappil, V. K., Weston, M. J., Thota, M., Valappil, V., Branch, O.,
1925 Wizemann, H., Kumar Kondapalli, N. S., Wehbe, Y., Hosary, T. AL, Shalaby, A., Shamsi, N. AL, &
1926 Naqbi, H. AL, Yousef, L.~~ (2020a). Assessing the Impact of Changes in Land Surface Conditions on
1927 WRF Predictions in Arid Regions. *Journal of Hydrometeorology*. [https://doi.org/10.1175/JHM-D-](https://doi.org/10.1175/JHM-D-20-0083.1)
1928 [20-0083.1](https://doi.org/10.1175/JHM-D-20-0083.1)[On the analysis of ground-based microwave radiometer data during fog conditriions.](https://doi.org/10.1175/JHM-D-20-0083.1)
1929 *Atmospheric Research*, 231, 104652. <https://doi.org/10.1016/j.atmosres.2019.104652>

1930 Temimi, M., Fonseca, R., Nelli, N., Weston, M., Thota, M., Valappil, V., Branch, O., Wizemann, H.,
1931 Kumar Kondapalli, N., Wehbe, Y., Hosary, T. AL, Shalaby, A., Shamsi, N. AL, & Naqbi, H. AL.
1932 (2020b). Assessing the Impact of Changes in Land Surface Conditions on WRF Predictions in Arid
1933 Regions. *Journal of Hydrometeorology*, 2829–2853. [https://doi.org/10.1175/JHM-D-20-](https://doi.org/10.1175/JHM-D-20-0083.1)
1934 [0083.1](https://doi.org/10.1175/JHM-D-20-0083.1)<https://doi.org/10.1175/JHM-D-20-0083.1>

1935 Tewari, M., Chen, F., Wang, W., Dudhia, J., Lemone, M. A., Mitchell, K., Ek, M., Gayno, G., Wegiel, J., &
1936 Cuenca, R. H. (2004). *Implementation and verification of the united NOAH land surface model in
1937 the WRF model.* [https://www2.mmm.ucar.edu/wrf/users/physics/phys-](https://www2.mmm.ucar.edu/wrf/users/physics/physics_refs/LAND_SURFACE/noah.pdf)
1938 [refs/LAND_SURFACE/noah.pdf](https://www2.mmm.ucar.edu/wrf/users/physics/physics_refs/LAND_SURFACE/noah.pdf)[https://www2.mmm.ucar.edu/wrf/users/physics/phys-](https://www2.mmm.ucar.edu/wrf/users/physics/physics_refs/LAND_SURFACE/noah.pdf)
1939 [refs/LAND_SURFACE/noah.pdf](https://www2.mmm.ucar.edu/wrf/users/physics/physics_refs/LAND_SURFACE/noah.pdf)

Formatted: Adjust space between Latin and Asian text, Adjust space between Asian text and numbers

Field Code Changed

Formatted: Default Paragraph Font, Font color: Blue

1940 Tie, X. (2003). Effect of clouds on photolysis and oxidants in the troposphere. *Journal of Geophysical*
1941 *Research*, 108(D20).
1942 <https://doi.org/10.1029/2003jd003659><https://doi.org/10.1029/2003jd003659>

1943 Tie, X., Brasseur, G., Emmons, L., Horowitz, L., & Kinnison, D. (2001). Effects of aerosols on
1944 tropospheric oxidants: A global model study. *Journal of Geophysical Research*, 106(D19), 22931.
1945 <https://doi.org/10.1029/2001JD900206><https://doi.org/10.1029/2001JD900206>

1946 Ukhov, A., Ahmadov, R., Grell, G., & Stenchikov, G. (2021). Improving dust simulations in WRF-Chem
1947 v4.1.3 coupled with the GOCART aerosol module. *Geoscientific Model Development*, 14(1), 473–
1948 493. <https://doi.org/10.5194/gmd-14-473-2021><https://doi.org/10.5194/gmd-14-473-2021>

1949 Van Geffen, J. H. G. M., Eskes, H. J., Boersma, K. F., & Veefkind, J. P. (2022). *TROPOMI ATBD of the*
1950 *total and tropospheric NO₂ data products document number : S5P-KNMI-L2-0005-RP*. Accessed
1951 on 10 July 2023, available online at
1952 [https://sentinel.esa.int/documents/247904/2476257/sentinel-5p-tropomi-atbd-no2-data-](https://sentinel.esa.int/documents/247904/2476257/sentinel-5p-tropomi-atbd-no2-data-products)
1953 [products](https://sentinel.esa.int/documents/247904/2476257/sentinel-5p-tropomi-atbd-no2-data-products)[https://sentinel.esa.int/documents/247904/2476257/sentinel-5p-tropomi-atbd-no2-](https://sentinel.esa.int/documents/247904/2476257/sentinel-5p-tropomi-atbd-no2-data-products)
1954 [data-products](https://sentinel.esa.int/documents/247904/2476257/sentinel-5p-tropomi-atbd-no2-data-products)

1955 Veefkind, J. P., Aben, I., McMullan, K., Förster, H., de Vries, J., Otter, G., Claas, J., Eskes, H. J., de Haan,
1956 J. F., Kleipool, Q., van Weele, M., Hasekamp, O., Hoogeveen, R., Landgraf, J., Snel, R., Tol, P.,
1957 Ingmann, P., Voors, R., Kruizinga, B., ... Levelt, P. F. (2012). TROPOMI on the ESA Sentinel-5
1958 Precursor: A GMES mission for global observations of the atmospheric composition for climate,
1959 air quality and ozone layer applications. *Remote Sensing of Environment*, 120, 70–83.
1960 <https://doi.org/10.1016/j.rse.2011.09.027><https://doi.org/10.1016/j.rse.2011.09.027>

1961 Veefkind, J., Keppens, A., & de Haan, J. (2021). *TROPOMI ATBD Ozone Profile*. Accessed on 10 July 2023.
1962 Available online at [https://sentinel.esa.int/documents/247904/2476257/Sentinel-5P-TROPOMI-](https://sentinel.esa.int/documents/247904/2476257/Sentinel-5P-TROPOMI-ATBD-Ozone-Profile.pdf)
1963 [ATBD-Ozone-Profile.pdf](https://sentinel.esa.int/documents/247904/2476257/Sentinel-5P-TROPOMI-ATBD-Ozone-Profile.pdf)[https://sentinel.esa.int/documents/247904/2476257/Sentinel-5P-](https://sentinel.esa.int/documents/247904/2476257/Sentinel-5P-TROPOMI-ATBD-Ozone-Profile.pdf)
1964 [TROPOMI-ATBD-Ozone-Profile.pdf](https://sentinel.esa.int/documents/247904/2476257/Sentinel-5P-TROPOMI-ATBD-Ozone-Profile.pdf)

1965 Waked, A., Afif, C., & Seigneur, C. (2012). An atmospheric emission inventory of anthropogenic and
1966 biogenic sources for Lebanon. *Atmospheric Environment*, 50, 88–96.
1967 <https://doi.org/10.1016/j.atmosenv.2011.12.058>[https://doi.org/10.1016/j.atmosenv.2011.12.0](https://doi.org/10.1016/j.atmosenv.2011.12.058)
1968 [58](https://doi.org/10.1016/j.atmosenv.2011.12.058)

1969 Wang, Y., Bai, Y., Zhi, X., Wu, K., Zhao, T., Zhou, Y., Xiong, J., Zhu, S., Zhou, W., Hu, W., Zhang, L., &
1970 Meng, K. (2022). Two Typical Patterns of Regional PM_{2.5} Transport for Heavy Air Pollution Over
1971 Central China: Rapid Transit Transport and Stationary Accumulation Transport. *Frontiers in*
1972 *Environmental Science*, 10. <https://doi.org/10.3389/fenvs.2022.890514>

1973 [Wang, W., Li, X., Shao, M., Hu, M., Zeng, L., Wu, Y., Tan, T. \(2019\) The impact of aerosols on photolysis](https://doi.org/10.5194/acp-19-9413-2019)
1974 [frequencies and ozone production in Beijing during the 4-year period 2012-2015. *Atmospheric*](https://doi.org/10.5194/acp-19-9413-2019)
1975 [Chemistry and Physics](https://doi.org/10.5194/acp-19-9413-2019), 19, 9413-9429. <https://doi.org/10.5194/acp-19-9413-2019>

1976 WRF (2023) Weather Research and Forecasting model [Model]. Accessed on 10 July 2023, available
1977 online at <https://github.com/wrf-model/WRF/releases>[https://github.com/wrf-](https://github.com/wrf-model/WRF/releases)
1978 [model/WRF/releases](https://github.com/wrf-model/WRF/releases)

1979 Wehbe, Y., Ghebreyesus, D., Temimi, M., Milewski, A., & Al Mandous, A. (2017). Assessment of the
1980 consistency among global precipitation products over the United Arab Emirates. *Journal of*
1981 *Hydrology: Regional Studies*, 12, 122–135. <https://doi.org/10.1016/j.ejrh.2017.05.002>

Formatted: Default Paragraph Font, Font color: Black

Formatted: Adjust space between Latin and Asian text, Adjust space between Asian text and numbers

Formatted: Default Paragraph Font, Font color: Blue

Field Code Changed

Formatted: Adjust space between Latin and Asian text, Adjust space between Asian text and numbers

Field Code Changed

Formatted: Default Paragraph Font, Font color: Blue

- 1982 [Wehbe, Y., Griffiths, S., Al Mazrouei, A., Al Yazeedi, O., & Al Mandous, A. \(2023\) Rethinking water](#)
 1983 [security in a warming climate: rainfall enhancement as an innovative augmentation technique.](#)
 1984 [npj Climate and Atmospheric Sciences, 171.](#) <https://doi.org/10.1038/s41612-023-00503-2>
- 1985 [Wehbe, Y., Temimi, M., Weston, M., Chaouch, N., Branch, O., Schwitalla, T., Wulfmeyer, V., Zhan, X.,](#)
 1986 [Liu, J., Al Mandous, A. \(2019\) Analysis of an extreme weather event in a hyper-arid region using](#)
 1987 [WRF-Hydro coupling, station, and satellite data. Natural Hazards and Earth System Sciences, 19,](#)
 1988 [1129-1149.](#) <https://doi.org/10.5194/nhess-19-1129-2019>
- 1989 Wesely, M. L. (1989). Parameterization of surface resistance to gaseous dry deposition in regional
 1990 numerical model. *Atmospheric Environment*, 23(6), 1293–1304. [https://doi.org/10.1016/0004-](https://doi.org/10.1016/0004-6981(89)90153-4)
 1991 [6981\(89\)90153-4](https://doi.org/10.1016/0004-6981(89)90153-4)[https://doi.org/10.1016/0004-6981\(89\)90153-4](https://doi.org/10.1016/0004-6981(89)90153-4)
- 1992 [Weston, M., Chaouch, N., Valappil, V., Temimi, M., Ek, M., Zheng, W. \(2018\) Assessment of the](#)
 1993 [sensitivity to the thermal roughness length in Noah and Noah-MP land surface model using WRF](#)
 1994 [in an arid region. Pure and Applied Geophysics, 176, 2121-2137.](#) [https://doi.org/10.1007/s00024-](https://doi.org/10.1007/s00024-018-1901-2)
 1995 [018-1901-2](https://doi.org/10.1007/s00024-018-1901-2)
- 1996 Wizenberg, T., Strong, K., Walker, K., Lutsch, E., Borsdorff, T., & Landgraf, J. (2021). Intercomparison
 1997 of CO measurements from TROPOMI, ACE-FTS, and a high-Arctic ground-based Fourier transform
 1998 spectrometer. *Atmospheric Measurement Techniques*, 14(12), 7707–7728.
 1999 <https://doi.org/10.5194/amt-14-7707-2021><https://doi.org/10.5194/amt-14-7707-2021>
- 2000 Yarragunta, Y., Srivastava, S., Mitra, D., & Chandola, H. C. (2021). Source apportionment of carbon
 2001 monoxide over India: a quantitative analysis using MOZART-4. *Environmental Science and*
 2002 *Pollution Research*, 28(7), 8722–8742. [https://doi.org/10.1007/s11356-020-11099-](https://doi.org/10.1007/s11356-020-11099-y)
 2003 [y](https://doi.org/10.1007/s11356-020-11099-y)<https://doi.org/10.1007/s11356-020-11099-y>
- 2004 Yarragunta, Y., Srivastava, S., Mitra, D., & Chandola, H. C. H. C. (2020). Influence of forest fire episodes
 2005 on the distribution of gaseous air pollutants over Uttarakhand, India. *GIScience and Remote*
 2006 *Sensing*, 57(2), 190–206.
 2007 <https://doi.org/10.1080/15481603.2020.1712100>[https://doi.org/10.1080/15481603.2020.171](https://doi.org/10.1080/15481603.2020.1712100)
 2008 [2100](https://doi.org/10.1080/15481603.2020.1712100)
- 2009 Yarragunta, Y., Srivastava, S., Mitra, D., Le Flochmoën, E., Barret, B., Kumar, P., & Chandola, H. C. C.
 2010 (2019). Source attribution of carbon monoxide and ozone over the Indian subcontinent using
 2011 MOZART-4 chemistry transport model. *Atmospheric Research*, 227(April), 165–177.
 2012 <https://doi.org/10.1016/j.atmosres.2019.04.019>[https://doi.org/10.1016/j.atmosres.2019.04.0](https://doi.org/10.1016/j.atmosres.2019.04.019)
 2013 [19](https://doi.org/10.1016/j.atmosres.2019.04.019)
- 2014 Yin, H., Lu, X., Sun, Y., Li, K., Gao, M., Zheng, B., & Liu, C. (2021). Unprecedented decline in summertime
 2015 surface ozone over eastern China in 2020 comparably attributable to anthropogenic emission
 2016 reductions and meteorology. *Environmental Research Letters*, 16(12).
 2017 <https://doi.org/10.1088/1748-9326/ac3e22><https://doi.org/10.1088/1748-9326/ac3e22>
- 2018 [Yousef, A. L., Temimi, M., Molini, A., Weston, M., Wehbe, Y., Al Mandous, A. \(2020\) Cloud Cover over](#)
 2019 [the Arabian Peninsula from Global Remote Sensing and Reanalysis Products. Atmospheric](#)
 2020 [Research, 238, 104866.](#) <https://doi.org/10.1016/j.atmosres.2020.104866>
- 2021 [Yu, Y., Notaro, M., Kalashnikova, O. V., Garay, M. J. \(2016\) Climatology of summer Shamal wind in the](#)
 2022 [Middle East. Journal of Geophysical Research: Atmospheres, 121, 289-305.](#)
 2023 <https://doi.org/10.1002/2015JD024063>

2024 Zhang, Y., Bocquet, M., Mallet, V., Seigneur, C., & Baklanov, A. (2012). Real-time air quality forecasting,
 2025 part I: History, techniques, and current status. *Atmospheric Environment*, *60*, 632–655.
 2026 <https://doi.org/10.1016/j.atmosenv.2012.06.031><https://doi.org/10.1016/j.atmosenv.2012.06.031>
 2027 [31](https://doi.org/10.1016/j.atmosenv.2012.06.031)

2028 [Zhang, X., Chen, H., Xu, X., Hu, X.-M., Gao, L., & Jia, G. \(2024\) Legacy of aerosol radiative effect
 2029 predominates daytime dust loading evolution. *Atmospheric Research*, *312*, 107735.
 2030 <https://doi.org/10.1016/j.atmosres.2024.107735>](https://doi.org/10.1016/j.atmosres.2024.107735)

2031 Zhang, Y., Pan, Y., Wang, K., Fast, J. D., & Grell, G. A. (2010). WRF/Chem-MADRID: Incorporation of an
 2032 aerosol module into WRF/Chem and its initial application to the TexAQ52000 episode. *Journal of
 2033 Geophysical Research Atmospheres*, *115*(18).
 2034 <https://doi.org/10.1029/2009JD013443><https://doi.org/10.1029/2009JD013443>

2035 Zhang, Xu, X., & Su, Y. (2020). Impacts of regional transport and meteorology on ground-level ozone
 2036 in windsor, canada. *Atmosphere*, *11*(10). <https://doi.org/10.3390/atmos11101111>

2037

2038

2039

2040

2041

2042

2043

2044

2045

2046

2047

2048

2049

2050

2051

Formatted: Adjust space between Latin and Asian text,
 Adjust space between Asian text and numbers

Field Code Changed

Formatted: Default Paragraph Font, Font color: Blue